

Towards Photonic Crystal-Based Spectroscopic Gas Sensors

Dissertation

zur Erlangung des akademischen Grades

doctor rerum naturalium (Dr. rer. nat.)

vorgelegt der

Mathematisch-Naturwissenschaftlich-Technischen Fakultät
(mathematisch-naturwissenschaftlicher Bereich)
der Martin-Luther-Universität Halle-Wittenberg

von

Herrn Dipl. Phys. Torsten M. Geppert
(geboren am 10.03.1975 in Offenburg)

angefertigt am

Max-Planck-Institut für Mikrostrukturphysik
Weinberg 2, 06120 Halle (Saale), Germany
und

Universität Paderborn, Dept. Physik,
Warburgerstr. 100, 33098 Paderborn, Germany

Gutachter:

Prof. Dr. R.B. Wehrspohn, Univ. Paderborn, Germany

Prof. Dr. Ph. Fauchet, Univ. Rochester, NY, USA

PD Dr. G. Seifert, Univ. Halle, Germany

Eingereicht: September 2005

Verteidigung: 10.04.2006

urn:nbn:de:gbv:3-000010074

[<http://nbn-resolving.de/urn/resolver.pl?urn=nbn%3Ade%3Agbv%3A3-000010074>]

Contents

1	Introduction and motivation	1
1.1	Electronic and photonic semiconductors	1
1.2	'Classical' PhC research	3
1.3	PhC-based sensors	3
1.3.1	Working principle of PhC-based gas sensors	5
1.3.2	PhC-based gas sensors: connection to the outside world	6
1.3.3	Fabrication of PhCs for gas sensors	6
1.4	Organization of the thesis	7
2	Goals of this work	8
2.1	Theory	8
2.2	Experiment	9
3	State-of-the-art gas sensors	10
3.1	Conventional gas sensors	10
3.1.1	Optical gas sensors	12
3.2	Alternative concepts	14
3.2.1	Ionization gas sensors	14
3.2.2	Frequency selective IR emitter/detector	15
3.2.3	PhC fiber-based spectroscopic gas sensor	16
4	Methods used in this thesis	17
4.1	Theoretical methods	17
4.1.1	Analytical treatment of photonic crystals	17
4.1.1.1	Maxwell's equations in periodic dielectric media	17
4.1.2	Numerical treatment of photonic crystals	20
4.1.2.1	Plane wave expansion (PWE)	21
4.1.2.2	Finite-difference time-domain (FDTD)	21
4.1.2.3	Finite element method (FEM)	23
4.2	Experimental methods	23
4.2.1	Macroporous Si fabrication process	23
4.2.1.1	Electrochemical dissolution of Si: the HF/n-Si contact	24
4.2.1.2	Formation of ordered macropores in n-type Si	25
4.2.2	Characterization	27
4.2.2.1	Optical Characterization by FTIR spectroscopy	27
4.2.2.2	Optical Characterization using a QCL	28
4.2.2.3	Surface characterization by AFM	29

5	Design of photonic crystal gas sensors	31
5.1	Software used in this work: overview and rating	31
5.2	Basic requirements for a PhC gas sensor	33
5.2.1	Working principle	33
5.3	Design of the photonic band structure	34
5.3.1	Spectral range	34
5.3.2	Resonance and interaction condition	35
5.3.3	Coupling condition	36
5.3.4	PhC interaction volume design: tuning and robustness	37
5.3.4.1	Tuning of PhC gas sensors	37
5.3.4.2	Robustness of PhC gas sensors	38
5.3.5	PhC interaction volume design: results	38
5.4	Transmission through a PhC gas sensor	39
5.4.1	Semi-classical approach: adiabatic taper	39
5.4.1.1	Adiabatic PhC taper: conclusions	43
5.4.2	Novel concept: Anti-Reflection-Layer (ARL)	44
5.4.2.1	ARL concept: robustness	46
5.4.2.2	ARL concept: working principle	48
5.4.2.3	ARL concept: conclusions	52
5.4.3	PhC gas sensor: absorption enhancement	52
5.4.4	PhC gas sensor: design results	53
6	Fabrication of PhC gas sensor structures	54
6.1	Why macroporous Si ?	54
6.2	Macroporous Si for PhCs: state-of-the-art in 2002	56
6.3	PECE of deep pore arrays	56
6.4	Realization of PhC tapers in the macroporous Si material system	59
6.4.1	Adiabatic PhC Taper	59
6.4.2	Anti-Reflection-Layer: PECE of deep trenches	60
6.5	Fabrication of macroporous Si membranes	63
7	Characterization of photonic crystal gas sensor structures	66
7.1	Characterization of the PECE ARL surface	66
7.2	Optical characterization of PhC gas sensor structures	69
7.2.1	Intrinsic macroporous Si absorption	69
7.2.2	PhC structures without taper	71
7.2.3	Adiabatic PhC Taper	72
7.2.4	Optical properties of ARL PhC structures	72
7.2.4.1	PhC with ARL: IR reflectance	72
7.2.4.2	PhC with ARL: QCL transmission	74
7.2.4.3	PhC with ARL: IR transmission	75
8	PhC gas sensor: device integration	80
8.1	Choice of the IR light source	80
8.2	Coupling of radiation to and from the PhC	80
8.3	Device dicing: realization of optically high grade interfaces	81
8.3.1	Cleaving	82
8.3.2	Sawing	82

8.3.3	Laser cutting	82
8.3.4	RIE etching	83
8.3.5	PECE of the ARL	83
9	Summary	85
10	Conclusion and outlook	87
	Appendix	I
A	Miscellaneous	I
A.1	Lattices	I
A.1.1	The hexagonal lattice	I
A.1.2	The distorted hexagonal lattice	I
A.2	Bragg diffraction at PhC interfaces	II
B	Publications and presentations	III
B.1	Publications	III
B.1.1	Publications primarily related to this thesis	III
B.1.2	Further publications	IV
B.2	Selected Talks	IV
B.2.1	Invited	IV
B.2.2	Contributed	V
B.3	Posters	V
B.4	Patents	V
C		VI
C.1	Eidesstattliche Erklärung	VI
C.2	Declaration in lieu of oath	VI
D	Curriculum Vitae	VII
E	Acknowledgements	VIII
F	Abbreviations and symbols	X
	Literature	XV

List of Figures

1	Macroporous Si	viii
1.1	Electronic and photonic semiconductors	1
1.2	Photonic crystals: periodic arrangements of dielectric materials	2
1.3	Conventional vs. PhC-based spectroscopic gas sensor	4
1.4	Application fields for gas sensors	5
3.1	Typical resonance frequencies corresponding to stretching and bending modes in gas molecules	13
3.2	Ionization gas sensors based on multiwalled carbon nanotubes	14
3.3	Narrow band IR emitter	15
3.4	PhC fiber-based spectroscopic gas sensor	16
4.1	Real- and reciprocal space for a 2D hex. latt. PhC	19
4.2	HF/n-Si interface: unbiased Schottky-like contact and IV curves	24
4.3	Lithographical prestructuring of a Si wafer	26
4.4	Photo-electrochemical etching of Si	27
4.5	FTIR spectroscopy principle	28
4.6	Quantum cascade laser (QCL) setup	29
4.7	AFM principle	30
5.1	Coupling condition: PW \rightarrow PhC mode	36
5.2	Tuning by rotation	37
5.3	Fresnel reflection at dielectric interfaces	40
5.4	Adiabatic taper for a bulk PhC	41
5.5	Adiabatic taper device scheme	42
5.6	Plane wave components of the TE _{B02K} Bloch mode	43
5.7	Anti-Reflection-Layer (ARL) scheme	44
5.8	Transmission through a PhC vs. ARL thickness	45
5.9	Robustness of ARL: rotation	46
5.10	Robustness of ARL: PECE proximity effect	47
5.11	Structure used for the calculation of the dispersion of surface modes in the ARL concept	48
5.12	Working principle of the ARL concept	49
5.13	Dispersion of surface modes in the ARL concept	50
5.14	Fields of surface and PhC modes in the ARL concept	51
5.15	H_z in a gas sensing PhC with ARL	52
5.16	PhC gas sensor: absorption enhancement	53

6.1	Photonic crystals made of silicon	54
6.2	Simple defect structures in 2D macroporous Si PhCs	55
6.3	PECE of deep macropore arrays	57
6.4	Deep PECE macropores	59
6.5	Adiabatic PhC taper realization: SEM of PECE macropores	60
6.6	ARL realization: mask design and lithography	61
6.7	PECE trenches	62
6.8	PECE trench: branching and dying due to thick ARL	62
6.9	PECE trenches: 2 μ m and 4.2 μ m pitch	63
6.10	Post-PECE macroporous Si membrane fabrication methods	64
6.11	In-situ macroporous Si membrane fabrication method	65
7.1	PECE ARL: surface quality	67
7.2	Equipotential surfaces for PhC/ARL and distorted hex. latt. PhC geometries	68
7.3	Si phonon absorption	69
7.4	Si absorption	70
7.5	Transmission through conventionally terminated PhC using a QCL	72
7.6	Distorted hexagonal lattice: optical characterization	73
7.7	PhC with ARL: optical characterization	74
7.8	PhC with ARL: optical characterization using a QCL	75
7.9	PhC with ARL: transmission vs. reflectance	76
7.10	PhC with ARL: transmission vs. reflectance	77
7.11	Scattering loss due to surface roughness	78
7.12	Surface roughness and nanopolishing of pore walls	79
8.1	Device integration: coupling of thermal emitter and PhC	81
8.2	Macroporous Si PhC: dicing	81
8.3	Successful device dicing: trenches etched during PECE	84
10.1	Alternative PhC-based gas sensor schemes	87

List of Tables

3.1	Overview of conventional spectroscopic gas sensors	11
5.1	Overview of different numerical methods for PhC calculations	32
5.2	Prominent absorption lines for common gases in the NIR/MIR	34
5.3	Fine tuning the PhBS by changing the r/a ratio	34
5.4	PhC modes for gas sensing in a 2D hex. macroporous Si PhC	39
7.1	Scattering loss per pore row	78
A.1	Bragg diffraction at a PhC interface	II

Zusammenfassung

Ziel dieser Arbeit ist die Untersuchung der Realisierbarkeit von kompakten spektroskopischen Gassensoren auf Basis photonischer Kristalle. Das zu Grunde liegende Funktionsprinzip basiert auf der Ausnutzung langsamer Gruppengeschwindigkeiten im photonischen Kristall, woraus eine verstärkte Wechselwirkung zwischen Strahlung und Gas in den Poren des photonischen Kristalls resultiert. Mit Hilfe numerischer Methoden wurde ein entsprechendes Wechselwirkungsvolumen aus 2-dimensionalen photonischen Kristallen basierend auf makroporösem Silizium entworfen. Um trotz der Verwendung von photonischen Kristall(Bloch)moden mit extrem niedrigen Gruppengeschwindigkeiten hohe Transmission durch das Wechselwirkungsvolumen zu erzielen, wurden zwei Konzepte zur effektiven Ein- und Auskopplung von elektromagnetischer Strahlung untersucht. Mit dem in dieser Arbeit entwickelten *Anti-Reflection-Layer* (ARL) Konzept, welches auf Kopplung mittels Oberflächenmoden basiert, ist es möglich Transmission von mehr als 90% bei einer Verstärkung der Wechselwirkung zwischen Gas und Licht von mehr als einem Faktor 30 zu erzielen. Entsprechende photonische Kristallstrukturen aus makroporösem Silizium wurden hergestellt. Der zur Herstellung verwendete photo-elektrochemische Ätzprozess wurde weiterentwickelt um Makroporen mit Tiefen von mehr als 450 μm herzustellen. Zur experimentellen Realisierung des ARL Konzeptes gelang es erstmals, tiefe Gräben neben geordneten Makroporenfeldern zu ätzen. Diese Methode liefert neben der ARL-Realisierung zusätzlich noch glatte Koppelkanten für die einfallende Strahlung und erlaubt des weiteren manuelle Vereinzeln von photonischen Kristall Sensorstrukturen mit sub- μm Präzision! Erste optische Messungen zur Charakterisierung der photonischen Kristallstrukturen mit ARL sowie Transmissionmessungen durch photonische Kristallstrukturen mit mehr als 200 Porenreihen in Transmissionrichtung wurden demonstriert.

Abstract

Goal of this work is the investigation of the feasibility of compact photonic crystal-based spectroscopic gas sensors. The underlying working principle is based on the utilization of low group velocities in the photonic crystal from which an enhanced interaction of radiation and gas within the photonic crystal results. Using numerical methods, an appropriate interaction volume made of 2-dimensional macroporous silicon photonic crystals was developed. To ensure high transmission through the photonic crystal despite the utilization of low group velocity modes, two concepts to achieve efficient coupling of light were investigated. The concept entitled *Anti-Reflection-layer* (ARL), which was developed in this work and utilizes coupling via surface modes, allows transmission through the photonic crystal interaction volume of more than 90% while a more than 30-fold interaction enhancement is achieved. Experimental realization of macroporous silicon photonic crystal structures with various coupling schemes was demonstrated. The photo-electrochemical etching process was improved to achieve macroporous structures of more than 450 μm depth. Experimental realization of the ARL concept was achieved by etching trenches next to ordered macropore arrays for the first time. In addition, this method yields almost flat coupling interfaces for incoming and outgoing radiation and allows manual device dicing with sub- μm precision! First optical characterization of photonic crystal structures with and without ARL as well as transmission measurements through photonic crystal structures of more than 200 pore rows along the transmission direction were performed.

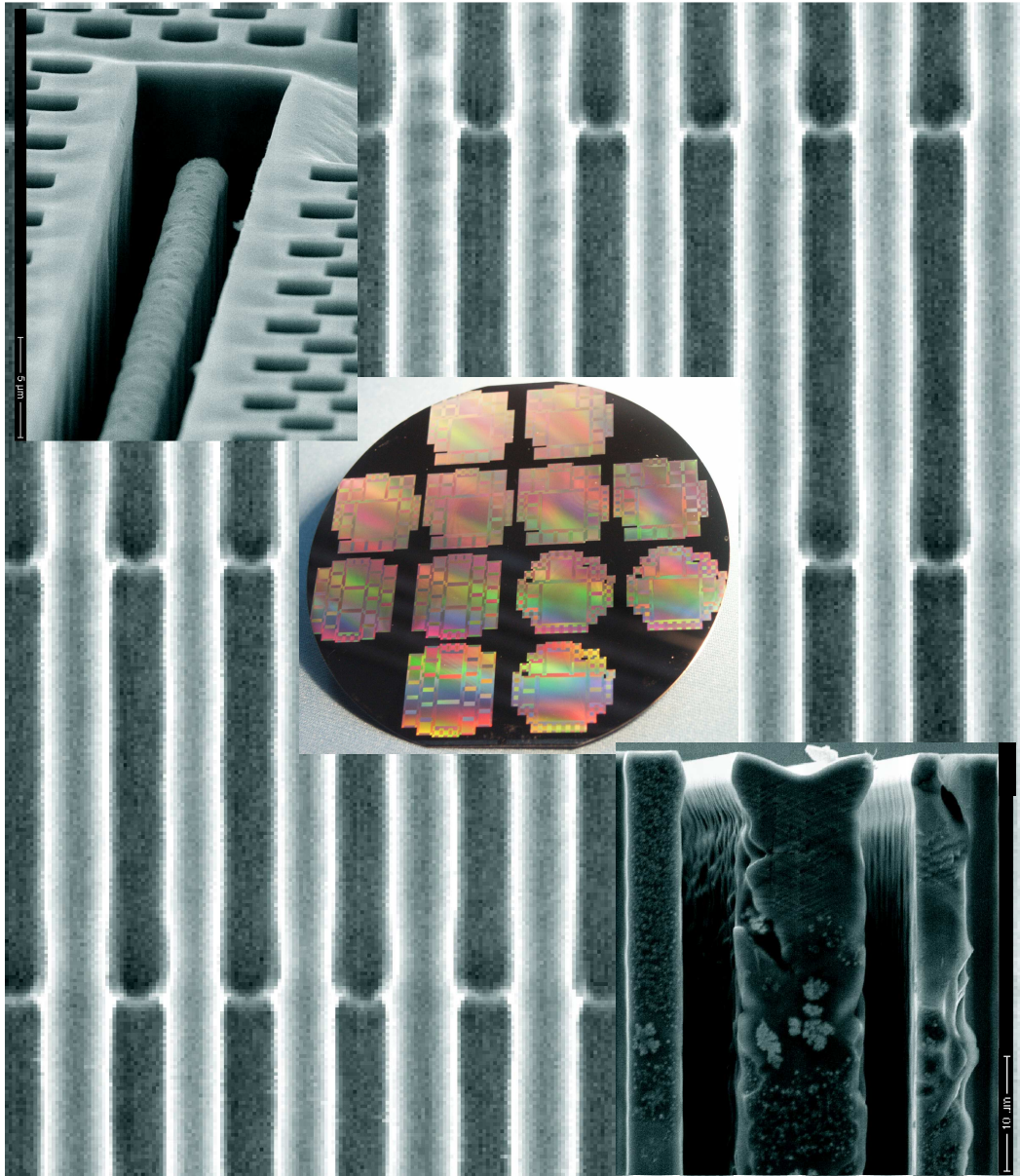


Figure 1: Background: depth markers produced by electrical breakdown pores during photo-electrochemical etching. Corner insets in the foreground: photo-electrochemically etched trenches in macroporous Si. Center inset: lithographically patterned 4 inch n-Si wafer ready for photo-electrochemical etching.

"He who has reached the point,
where he no longer errs,
has ceased to perform."

Max Planck

"Wer es einmal so weit gebracht hat,
dass er nicht mehr irrt,
der hat auch zu arbeiten aufgehört."

Max Planck

Chapter 1

Introduction and motivation

1.1 Electronic and photonic semiconductors

Since the realization of the first transistor [1] in 1947 electronic semiconductors have been extensively studied for about six decades and many of their properties are now well understood [2][3]. Figs.1.1a and b illustrate the dramatic progress in the field of electronic semiconductors during this period, comparing the first experimentally realized (point contact) transistor based on electronic semiconductors and a state-of-the-art microprocessor made up of millions of (field effect) transistors on an area of a few mm^2 . One of the most interesting and probably the most important property of electronic semiconductors is the existence of a band structure for electrons and holes. This electronic band structure governs the behavior of electrons and holes in an electronic semiconductor by determining their allowed energy and momentum states.

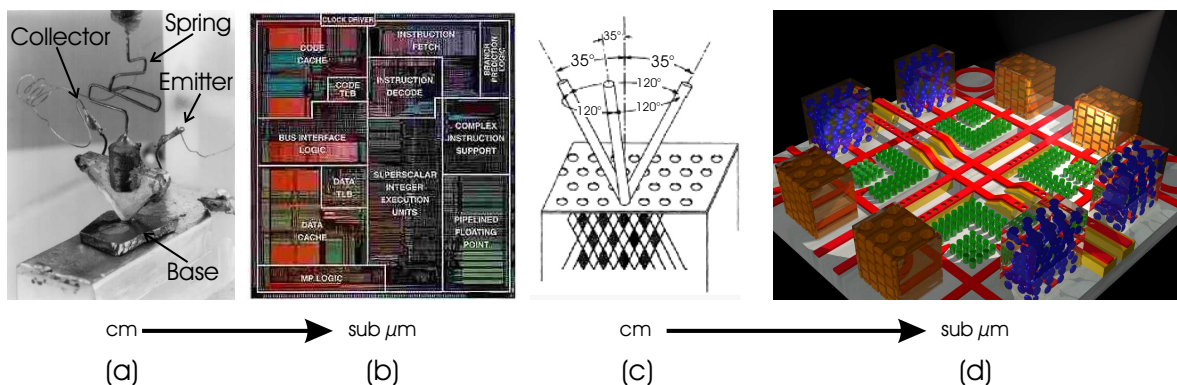


Figure 1.1: Dramatic development with enormous impact: **a)** first transistor based on electronic semiconductors by Bardeen, Brittain and Shockley in 1947 [1] and **b)** modern state-of-the-art microprocessor (Intel Pentium 4[®]). **c)** First experimentally realized photonic crystal with 3D band gap by Yablonovitch (1991) [4] **d)** Photonic Micropolis as envisioned by Joannopoulos et al. [5]. (Typical feature size given below the pictures.)

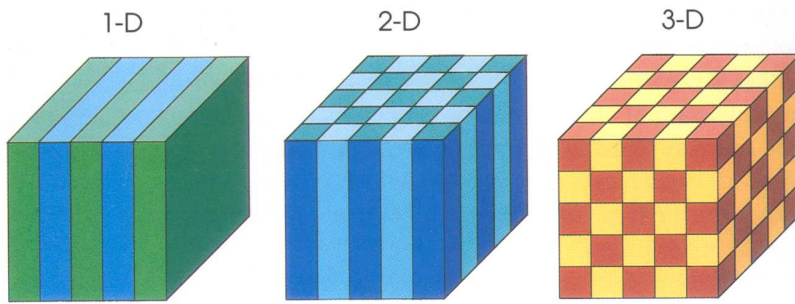


Figure 1.2:
Photonic crystals: periodic arrangements of dielectric materials with different refractive indices. [5]

The possibility to engineer the electronic band structure by, e.g., growing epitaxial alloys of different semiconductors like $\text{Ga}_{1-x}\text{In}_x\text{As}$ or layered quantum well structures like $\text{Al}_x\text{Ga}_{1-x}\text{As}/\text{GaAs}$ or simply by incorporating defect atoms such as phosphorus (P) and boron (B) in Si (*doping*), opened a wide field for both fundamental physics as well as applications in optics and electronics. In the field of fundamental physics, the discovery of the fractional quantum hall effect by Laughlin, Tsui and Störmer was only enabled by the availability of highest quality GaAs/AlGaAs semiconductors. Among the countless applications, Si-based microprocessors and III-V semiconductor-based optical components such as semiconductor lasers and detectors are to be mentioned. Nowadays, electronic semiconductors are indispensable in our everyday life, controlling - in the form of integrated circuits - or functionalizing - in the form of optically active components - almost every electric and (opto)electronic device we use.

But only shortly before the end of the 20th century the optical counterpart of electronic semiconductors, the so-called photonic crystals (*PhCs*), were devoted a huge amount of attention by fundamental as well as applied researchers. The idea of PhCs was introduced to the scientific community independently by John [6] and Yablonovitch [7] in 1987 while studying different theoretical questions, namely the localization of light in disordered media and low threshold lasers, respectively. PhCs are structures consisting of *periodic* arrangements of dielectric materials with different refractive indices as shown in fig.1.2. As a consequence a *photonic band structure* (*PhBS*) arises. Analogous to the electronic band structure, the PhBS governs the propagation of light in the PhC by relating frequency ω and wavevector \vec{k} of photons. Within the PhC photons of certain energy are allowed to travel along certain directions while for certain other directions and within certain frequency ranges - in the so-called photonic band gap (*PhBG*) - light propagation is forbidden. The PhBS can be tailored by choosing the dielectric materials and the way in which they are arranged. The analogue to doping in the electronic case can be achieved by disturbing the periodicity, e.g., by removing, adding or displacing dielectric material.

Keeping in mind the tremendous impact electronic semiconductors had in the 20th century and the fact that PhCs are their optical analogue - promising comparable potential for the manipulation of light - explains the enormous efforts recently put in understanding, fabricating and investigating PhCs. Figs.1.1c and d illustrate the anticipated development of PhCs by comparing the first experimentally realized PhC [4] with its currently envisioned further development, the *Photonic Micropolis*, being the equivalent to the electronic microprocessor.

1.2 'Classical' PhC research

The properties of PhCs studied so far are manifold due to their enormous potential for the manipulation of light.

In the sector of fundamental research a lot of effort was put into finding structures with a complete PhBG, i.e., a PhBG for *all* spatial directions [4][8][9][10]. Furthermore the investigation of effects such as enhanced or suppressed emission of light in a PhC resulting from the modified photonic density of states (*PhDOS*) were focused on [7][11]. Another interesting field is the investigation of the unusual dispersive and refractive properties arising from the PhBS, such as, e.g., the superprism [12].

In the application sector the studies concentrated on using PhCs as potential components in optical circuits. PhC resonators were used as add/drop filters for signal injection/extraction [13][14][15][16], etc. PhC waveguides and beam splitters were anticipated to allow fabrication of very compact optical circuitry - even with incorporated functionality such as dispersion compensation or selectivity to different polarizations [17][18][19][20]. Lasers based on PhCs offer the advantage of low threshold current [21]. PhC-based switching devices are necessary for the realization of an optical transistor - the necessary prerequisite for an optical microprocessor.

While the above mentioned functionalities have been demonstrated in principle, the PhC components designed and fabricated so far still lack the requested requirements to be used on an industrial application scale. The reasons for this are manifold. Besides the baisse in the high-tech market that limits the will of industry to invest more time and money into PhC research, PhC-based components for the optical industry face hard competition from already established techniques. The latter have grown mature, i.e., they can be fabricated with high quality for a reasonable price with currently well developed processes and they are capable to sufficiently fulfill almost all demands of today's optics industry. In turn, the fabrication of PhC-based optical components for the technologically interesting wavelength range of 1.3 μm and 1.5 μm is still working at the limits of currently available production systems. This results in intolerably high deviations from the designed structure, thereby either ruining the functionality of the PhC device or disturbing other components in optical networks. As a consequence, nowadays PhCs have to seek their salvation in niche markets. One example to be mentioned here are the (hollow core) photonic crystal fibers by Russel et al. [22] - the only commercially successful application of PhCs so far. PhC fibers guide the light not by total internal reflection occurring at the interface of a high index core and a low index cladding layer but by PhBG mechanism. This enables PhC fibers to guide light of high intensities or at wavelengths not accessible with conventional fibers. Furthermore the dispersion of these fibers can be tailored and PhC fibers can be endlessly single mode [23][24].

1.3 PhC-based sensors

Last but not least, due to the still missing PhC-based *killer application* in the field of photonics, the use of PhCs for sensing applications has gained more and more attention during the last years. The shift of the resonance frequency of a microcavity's defect state due to the change in refractive index contrast in a PhC structure after infiltration of liquids, gases or bio-molecules can be used as detection signal as investigated by the groups of Prof. Fauchet (Univ. Rochester,

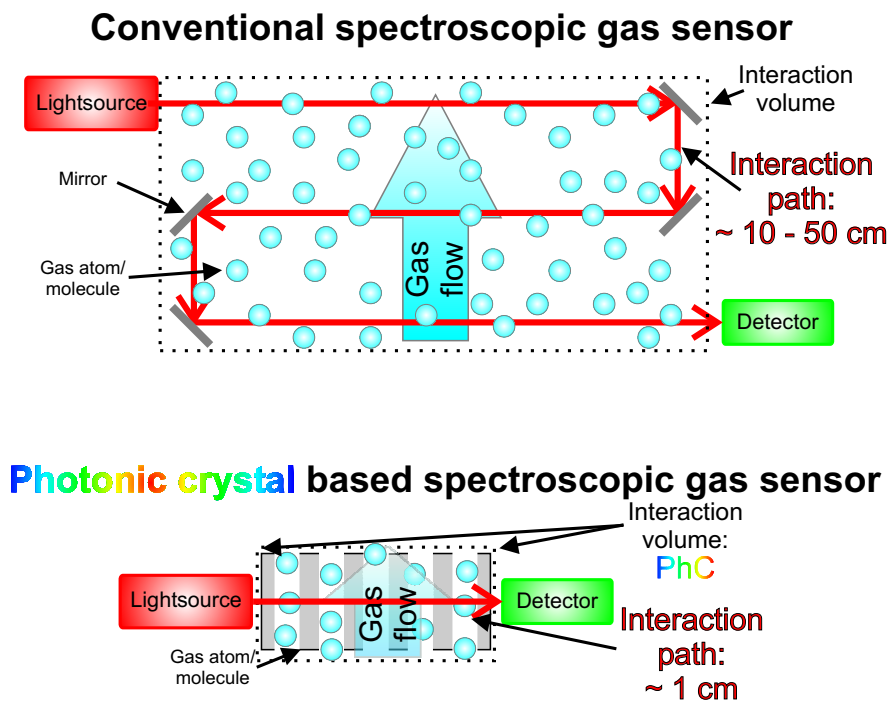


Figure 1.3: Conventional vs. PhC-based spectroscopic gas sensor. The intensity of light transmitted through a gas filled interaction volume serves as signal for the determination of the gas concentration. In the PhC-based scheme the conventional interaction volume usually consisting of a glass tube is replaced by a PhC membrane.

USA) [25] and Prof. Scherer (Caltech, USA) [26]. In addition to such spectroscopic approaches, in the group of Prof. Pavesi (Univ. Trento, Italy) quantities such as the electrical conductivity or the photoluminescence intensity as a function of ambient gas concentration were investigated within the scope of a multi-parametric, porous silicon microcavity structure [27].

Likewise, in this work the applicability of PhCs outside the conventional optics field is investigated, namely the application of PhCs for the realization of compact gas sensor devices, as depicted in fig.1.3. The PhC based gas sensor concept represents a modification of a conventional spectroscopic gas sensor in which the intensity of light transmitted through an interaction volume for light and gas serves as signal from which the concentration of the gas can be derived. The difference consists in the type of interaction volume. While in conventional spectroscopic gas sensors the interaction volume is realized by, e.g., a glass tube, it is replaced by a PhC membrane in the PhC-based detection scheme.

For the realization of a PhC-based gas sensor some of the previously mentioned problems hindering the success of PhCs in optical circuits are no longer present. First, fabrication of PhC structures, e.g., by using the macroporous silicon material system, is easier because the wavelength range of interest covers the NIR/MIR spectral region. Along with it, the PhC feature size to be realized lies in the μm -range. This helps to keep relative fabrication deviations small. Second, the fact that the intended PhC-based gas sensor is an optical gas sensor makes it rather competitive with other types of gas sensors, such as metal-oxide gas sensors etc. Their functionality mainly depends on surface reactions and is therefore prone to contamination and depletion. In addition, these sensors lack broad range selectivity, as will be discussed in chapter 3.1. The unique characteristic



Figure 1.4:
Application fields for gas sensors: environmental monitoring, automotive applications, medical and safety systems.

of the PhC-based gas sensor with conventional optical gas sensors originates from its expected compactness. As will be described in detail later, a reduction in size of the interaction volume on the order of one magnitude is expected for a PhC-based gas sensor as compared to a conventional spectroscopic gas sensor. And in contrast to the IT/optics industry that has shown considerable yearly growth rates ($\gtrsim 10\%$ per year) during the last decades but a drastic collapse in the last years, the market for sensors grows slowly but steadily with a few percent per year^{1,2}. In addition, there are many fields in which gas sensors are needed, a few of them are shown in fig.1.4. Environmental monitoring is becoming more and more important along with industrial monitoring of processes involving gaseous substances or exhaust fumes. Furthermore, medical applications such as anesthesia and breathing systems as well as safety equipment such as fire detectors are becoming increasingly relevant. In the automotive sector not only exhaust fumes but potentially also the drivers blood alcohol level could be monitored to increase traffic safety³.

1.3.1 Working principle of PhC-based gas sensors

Due to their photonic band structure PhCs offer different strategies to be used in sensing devices. One possibility is to use the spectral shift of a defect state or a band edge due to the change of refractive index contrast of the PhC when certain species, e.g., gas molecules, are present within a PhC. But for gases this approach is not optimally suited because their refractive indices are very similar to the refractive index of air and therefore the change in dielectric contrast and along with it the spectral shift of the frequency under study is rather small. As a consequence, although detection of the presence of certain species is possible, quantitative analysis is rather challenging. Another only recently discussed approach utilizes PhC fibers into which the gaseous species to be detected is infiltrated. As in the conventional spectroscopic detection scheme the absorption of light travelling along the gas filled fiber is measured [28]. Due to the strong confinement of light within the PhC fiber and the tiny size of the PhC fiber, within this detection scheme compact spectroscopic gas sensors requiring only small interaction volumes can be realized (fiber length \approx few cm, sensitivity \approx a few ppb).

¹Infrared devices lead gas-sensors market: the Frost&Sullivan report values last year's European gas sensors and analyzers market at USD 283.9 million. Infrared gas sensors accounted for USD 112.4 million, or 40% of total revenues. The demand for infrared sensors is expected to remain high as applications for the technology increase over the next few years, with revenues reaching USD 133.3 million in 2007. This represents a compound annual growth rate of 2.4% for the forecasted period. (from "Opto & Laser Europe", November 2001)

²US Market: annual increase of 8.7% until 2007, Frost&Sullivans, (from Optical Sensors, Oct. 2003)

³Volvo announced this feature as part of his "speed key" concept in August 2005.

The new - and patented [29] - approach taken in this work is based on the enhancement of the interaction between light and gas molecules within an appropriately designed PhC. The slope of a band in the PhBS corresponds to the group velocity v_g of light. As a consequence, for certain frequencies and along certain directions within a PhC the group velocity of light is as low as a few tenths of percent of the velocity of light in vacuum c_0 [30][31][19]. If the PhC is designed in a way that such a low v_g frequency coincides with a resonance frequency of the gas, typically a rotational-vibrational excitation, an enhanced interaction compared to gas molecules within a conventional interaction volume should be obtained. Such an enhancement of the interaction can be measured by comparing the absorption of light along a certain interaction length.

1.3.2 PhC-based gas sensors: connection to the outside world

For a PhC being used in an absorption measurement-based gas sensor light from a source, e.g., a thermal infrared (*IR*) emitter, has to be coupled into the PhC as well as coupled out from the PhC to reach the detector. This results in two major challenges.

First, in a semi-classical picture, for a photonic band with low v_g the corresponding refractive index n_{eff} is rather large according to $n_{\text{eff}} = c_0/v_g$. This leads to very high reflection at the air/PhC interfaces as described by Fresnel's equations.

Second, the incoming light, which has the form of a plane wave, has to couple to a low v_g Bloch mode in the PhC.

To allow efficient coupling of light to and from the PhC two taper concepts have been developed and investigated. It turned out that a semi-classical approach based on adiabatically adjusting the dielectric contrast between air and the PhC mode by appropriately distorting the PhC lattice does not lead to the desired enhanced coupling.

As a solution, a second concept was developed. This new concept entitled Anti-Reflection-Layer (*ARL*) is based on modifying the shape of the air/PhC interface by changing it from a corrugated surface - which usually results from cleaving a PhC structure along a row of pores - to a flat interface which is realized by leaving a layer of unstructured material of the dielectric matrix in front of the first pore row of the PhC. By choosing the correct thickness of this layer it is possible to drastically increase the transmission through a PhC structure suited for gas sensing up to about 95% in contrast to about 40% transmission through a conventionally terminated PhC gas sensor structure, as found in numerical simulations. It is shown that the underlying working principle is based on an interplay of diffraction at the grating formed by the outermost pore row of the PhC, surface states forming in the ARL and coupling of these surface states to the desired PhC Bloch mode. It should be mentioned here that this ARL is *not* an Anti-Reflection-Coating (*ARC*) in the form of a $\lambda/4$ -layer known from wave optics!

1.3.3 Fabrication of PhCs for gas sensors

The PhC structures are fabricated using the macroporous silicon material system. The possibility to choose the PhC geometry by lithography allows to incorporate the above mentioned taper concepts necessary to achieve high transmission through the structure. In addition, the possibility to produce almost perfect, large scale ($\geq \text{cm}^2$) pore arrays with very high aspect ratios ($AR \geq 150$)

allows the realization of sufficiently large interaction volume for the light and the gas. The already established macroporous Si fabrication with typical pore depths of about $100\ \mu\text{m}$ has successfully been improved to allow realization of macropore arrays - even with included ARL structures - with depths of up to $450\ \mu\text{m}$.

1.4 Organization of the thesis

After this very general introduction to PhCs and the motivation for investigating PhC-based gas sensors, the remaining part of this thesis is structured as follows: in chapter 2 the main theoretical and experimental goals pursued in this work are summarized. Following in chapter 3 is a brief overview of currently used detectors for gas sensing - with emphasis on spectroscopic gas sensors - discussing their different working principles as well as related advantages and shortcomings. Furthermore, only recently suggested and implemented alternative approaches are introduced. In chapter 4 the theoretical and experimental methods relevant for this work are explained and discussed. The subsequent chapter 5 is devoted to the theoretical design of suitable photonic crystal structures to be used in gas sensors with emphasis on band structure and transmission requirements, preceded by a short section assessing the usefulness of the numerical methods described in 4. Chapter 6 treats the fabrication of photonic crystal structures for gas sensing based on macroporous silicon including two taper concepts developed in this work. The properties of these structures are investigated and compared to theory in chapter 7. Device integration of a spectroscopic PhC-based gas sensor is discussed in chapter 8. Chapter 9 summarizes the main issues treated in this thesis, followed by an outlook given in chapter 10. A list of abbreviations and symbols used throughout this thesis can be found in F at the very end.

Chapter 2

Goals of this work

The main goal of this thesis is to explore the potential of PhCs to be used in spectroscopic gas sensors and to design, fabricate and characterize appropriate PhC structures.

The idea is to replace the interaction volume of light and gas in a conventional spectroscopic gas sensor by an appropriately designed PhC. Due to the expected enhanced interaction of light and gas within the PhC interaction volume resulting from the reduced group velocity for certain frequencies it should be possible to shrink the size of such a PhC-based spectroscopic gas sensor by more than an order of magnitude as compared to conventional spectroscopic gas sensors. The theoretical as well as experimental issues which have to be addressed are stated in the following part of this chapter.

2.1 Theory

The theoretical concerns are discussed in two stages. First, the design of the PhC-based interaction volume itself will be addressed. Second, the connection of the PhC interaction volume to the outside world will be investigated. The questions to be clarified are:

1. Which requirements does the photonic band structure of the PhC have to meet?

Taking into account

- that the wavelength region of interest is the mid-infrared (*MIR*) spectral region from about $3 \mu\text{m}$ to $20 \mu\text{m}$ and
- the dielectric contrast of $11.6 : 1$ is given by the macroporous silicon material system used and
- ordered macropore arrays with lattice constants a ranging from $0.5 \mu\text{m} \leq a \leq 20 \mu\text{m}$ with pore radii r ranging from about $0.25a \leq 2r \leq 0.45a$ can be photo-electrochemically etched

set the boundary conditions for the design freedom for a PhC-based spectroscopic gas sensor, the following matters will be addressed:

- (a) Which lattice geometry is appropriate?

- (b) Which bands spectrally overlapping with the gas absorption frequency promise to have low group velocity v_g ?
 - (c) Along which directions (in reciprocal as well as in real space) do these low v_g appear and can they be easily accessed in terms of interface fabrication?
 - (d) Is a sufficient amount of the electric field of these low v_g modes mainly concentrated within the pores of the macroporous Si and therefore allows interaction of the PhC mode and the gas?
 - (e) Which of these low v_g bands allow - concerning their symmetry - coupling from an incoming and to an outgoing plane wave?
2. How can *efficient* coupling of incoming and outgoing plane waves, respectively, to the low v_g PhC Bloch mode under consideration be achieved?
Two alternative taper concepts will be discussed:
- (a) semi-classical adiabatic taper
 - (b) novel Anti-Reflection-Layer (ARL) approach.¹

2.2 Experiment

On the experimental side, the goal is to fabricate suitable structures for a PhC-based spectroscopic gas sensor and to eventually succeed in a proof-of-principle experiment showing the enhanced interaction of gas and light.

The different stages towards these goals are:

1. Fabrication of suitable PhC structures in the macroporous silicon material system. In particular
 - (a) photo-electrochemical etching of deep ($d \gtrsim 450 \mu\text{m}$), parallel macropores
 - (b) realization of the different taper concepts in the macroporous silicon material system.
2. Optical characterization of the fabricated PhC structures including
 - (a) verification of the coupling enhancement achieved by the use of the ARL concept and comparison to theory
 - (b) transmission measurements through the PhC structures
 - (c) possibly verification of the enhanced interaction of light and gas within the PhC.

¹This ARL concept is not to be confused with conventional Anti-Reflection-Coatings (ARCs) widely used in optics to minimize the reflection at dielectric interfaces.

Chapter 3

State-of-the-art gas sensors

In this chapter a brief overview of currently used gas sensing concepts is given. The different detection principles are described and the advantages and shortcomings of each approach are pointed out. The first part concentrates on widely used conventional gas sensing schemes while the second part focuses on some recently developed approaches, suggested as future alternatives.

3.1 Conventional gas sensors

Table 3.1 gives an overview of widely used conventional gas sensor schemes. The first four methods rely on measuring the change of an electrical quantity of the sensor's active material. This change is caused by adsorption or absorption of chemical species at the surface of the active material.

Metal-oxide gas sensors: One widely used class of gas sensors is based on metal-oxides (*MO*) as functional layers. For elevated temperatures the conductivity of these layers strongly depends on the adsorption of certain gases on their surface. By doping these layers with, e.g., Pd or Pt ($\approx 0.5\%$ wt), n-type conductivity is achieved. Adsorption of easily oxidizable gases like oxygen leads to a transfer of those electrons onto the oxygen atoms, resulting in a decrease of excess electrons in the $\text{SnO}_2\text{:Pt}$ layer. This in turn leads to a decrease in conductivity which is finally used as the detection signal. Similarly, p-doped MO-layers are primarily used for the detection of easily reducible gases.

A major shortcoming of this scheme is its inherently low selectivity with respect to specific gases because *any* oxidizing gas will lead to a decrease in conductivity. Furthermore *any* reducing gas will in turn increase the number of electrons in the $\text{SiO}_2\text{:Pt}$ layer and along with it the conductivity will be increased, resulting in erroneous detection. In addition, this type of sensor is also very sensitive to humidity.

Solid electrolyte gas sensors: Another widely used gas sensing scheme relies on *solid* electrolytes. It utilizes the property of certain ionic crystals, such as, e.g., ZrO_2 , to allow current transport via ions at elevated temperatures. These sensors come in two principle designs: potentiometric and amperometric.

Underlying the working principle of the first - namely the potentiometric - design is the Nernst-equation $U = \frac{R_g T}{4FC} \ln \frac{p_1}{p_2}$, relating the measured voltage between two electrodes with the partial

Detection method	Physical quantity (change)	Example
Impedance spectrometry	Conductivity $\Delta\sigma_e$ Impedance ΔZ_e Resistance ΔR_e	Metal-oxide sensors & conducting polymer layers with interdigital electrodes
Amperometric	Current ΔI_e	Clark-sensor (liquid oxygen)
Potentiometric	Voltage ΔU_e	Lambda-probe (exhaust fumes)
Capacitive	Dielectric constant ΔC	
Calorimetric	Adsorption heat ΔT_{Ads} Reaction heat ΔT_{React}	Polymer membranes Pellistor
Gravimetric	Mass Δm	Quartz Crystal Microbalance (QCM) Surface Acoustic Wave (SAW)
Optical	Absorption, reflection transmission, fluorescence	Optode

Table 3.1: Overview of widely used conventional spectroscopic gas sensing methods.

pressures p_1 and p_2 of the gas species in different spatial regions, F_C being Faraday's constant, R_g the universal gas constant and T the working temperature. The most prominent application of this scheme is currently the oxygen sensor based on zirconium-oxide doped with Yttrium $ZrO_2:Y$, the so called *lambda-probe* in automotive applications.

Recently Siemens [32] announced the development of mm-sized potentiometric gas sensors for ozone, CO_2 , NO_x , etc., based on metal-oxides and polymers being fully compatible with standard CMOS processes.

In the second design - the amperometric scheme - gas detection is based on current measurement. The gas, e.g., oxygen, is reduced to O^{2-} at the cathode, e.g., made of Pt. The O^{2-} ions diffuse through a ZrO_2 layer and reach the anode where they are oxidized to elementary oxygen O_2 . The current flow from the anode to the cathode is a measure of the oxygen concentration.

Capacitive gas sensors: Capacitive gas sensors measure variations of the capacitance ΔC due to either a change of the dielectric constant or a change in thickness of the active layer induced by the gaseous species to be detected. Especially in the case of thickness variations this type of sensor, like the conductometric approach, has a tendency to yield erroneous results because a the thickness change can be the result of, e.g., thermal or mechanical stress not related to the presence of gas.

Calorimetric gas sensors: Calorimetric gas sensors detect the change of temperature ΔT of the active surface layer, made of, e.g., poly-siloxane derivatives due to adsorption or a chemical reaction (*pellistors*) of the gas molecules at the surface layer.

Another shortcoming is the relatively large thermal mass and the resulting slow response time. While these two issues can in principle be eliminated by use of modern micro-technology processes to fabricate, e.g., very thin ($< 1 \mu m$) Si_3N_4 membranes with response times in the range of milliseconds, also for this detection scheme the major drawback lies in its low selectivity.

Gravimetric gas sensors: Gravimetric gas sensors come in two major designs, namely as a quartz crystal microbalance (QCM, also known as bulk acoustic wave (BAW) sensor) and as surface acoustic wave (SAW) detectors.

The QCM detection scheme is based on the Sauerbrey equation $\Delta f \propto \frac{f_0^2}{A} \Delta m$ which states that the change in resonance frequency Δf of a thin quartz crystal covered with a gas sensitive layer is proportional to the additional mass Δm of the adsorbed gas atoms, f_0 being the resonance frequency of the uncovered quartz and A the area sensitive to the gas. State-of-the-art QCMs allow a detection limit in the parts-per-trillion (*ppt*) range.

SAW sensors consist of two electrode pairs, which are deposited with a certain distance from each other on a substrate. The region between the electrodes is coated with gas sensitive substances that allow adsorption of gas atoms. One electrode pair is used for the creation of a surface wave that travels along the gas sensitive region towards the other electrode pair, which is used to detect the amplitude and frequency of the incoming SAW. Gas atoms adsorbed in the region between the sender and detector electrodes change the phase and/or amplitude of the SAW resulting in a detectable signal. The lower detection limit for these SAW sensors lies in the range of a few ppb. The gravimetric QCM and SAW detectors have the advantage of being rather sensitive, relatively cheap and have a fast response time. The remaining problem for these systems is their limited selectivity which depends on the availability of coating layers which only allow specific gases to adsorb. Such specific coatings do exist, but unfortunately only for very few gases.

3.1.1 Optical gas sensors

Each of the above schemes has its advantage, be it easy and cheap fabrication by standard micro-electronic or micro-mechanical processes, tiny size, or high operating temperature. But the major drawback of the above sensor schemes is their lack of broad range selectivity due to a lack of sensitive materials for every gas and/or due to crosstalk. In the following part of this section the structurally more complex but in their generality and selectivity outstanding properties of optical gas sensing schemes are discussed. There are a number of different detection mechanisms, used in optical gas sensors as can be seen in the last row of table 3.1.

Optical gas sensors offer a variety of advantages compared to the concepts described above. One important reason lies in the fact that the species used for detection - namely the photons - is of a fundamentally different nature compared to the species to be detected - namely the gas atoms/molecules. Compared to the other concepts described above the species used for detection does not influence the detection mechanism itself. Photons have no residual mass and carry no charge, so do neither influence charge- nor mass-based detection schemes. Furthermore, because IR spectroscopy-based sensors do not rely on catalytic or electrochemical reactions, they are not prone to depletion or contamination of the surface.

But the by far most important reason is the selectivity optically based detection schemes facilitate due to the very characteristic *fingerprint* most gases show in their IR absorption spectra, especially in the near- and mid-infrared spectral region from $\approx 1.5 \mu\text{m} - 30 \mu\text{m}$. Interaction of electromagnetic (*em*) radiation with certain molecules leads to excitation of characteristic rotational-vibrational (*ro-vib*) states of the molecule. The frequency of these *ro-vib* states depends on the participating functional groups, i.e., on the atoms and the bonding of these atoms to their surrounding, see figure 3.1. The lineshape of such a *ro-vib* state is the superposition of the broader vibrational excitation on which very narrow lines originating from rotational states are superimposed. The

Stretching modes		Bending modes	
Group	$\tilde{\nu}$ (cm ⁻¹)	Group	$\tilde{\nu}$ (cm ⁻¹)
	3300		1650
	3020		900
	2960		1700
	2050		3600
			700
			1100
			1450
			300

Figure 3.1: Typical resonance frequencies $\tilde{\nu}$ corresponding to stretching and bending modes in gas molecules [33].

spectral distance $\tilde{\nu}_2(\text{Gas 1}) - \tilde{\nu}_1(\text{Gas 2})$ is inversely proportional to the momentum of inertia for rotation of the molecule around the corresponding axis, i.e., the heavier the involved groups, the closer are the corresponding ro-vib lines. The spectral distance of subsequent rotational states is given by twice the rotation constant B : $\Delta\tilde{\nu} = 2B$. In principle also electronic excitations of the gases could be used for detection in the visible spectral range (VIS). But in mixtures of gases the selectivity to a specific gas would not be guaranteed due to the possible overlap of lines of different gases due to their relatively large line width of $\approx 10^4 \text{ cm}^{-1}$. In contrast, the ro-vib states in the NIR/MIR spectral regions have very narrow linewidths on the order of a few tenths of cm^{-1} (e.g., $\Delta\tilde{\nu}(\text{CO}) \approx 0.1 \text{ cm}^{-1}$) while the distances between the lines are on the order of a few cm^{-1} (e.g., $\tilde{\nu}_2(\text{CO}) - \tilde{\nu}_1(\text{CO}) \approx 4 \text{ cm}^{-1}$). So the probability of overlap of characteristic lines of different gases is rather low, allowing for a high selectivity.

Furthermore, the sensitivity of optical gas detection schemes can be as high as a few ppb, provided that a sufficient interaction of the gas and the em radiation is achieved.

Pure rotational states of molecules, corresponding to excitations in the MW spectral range, offer in principle the same advantages of narrow linewidths while having large spectral distance. But the fact that the working pressure should be below 1 mbar for achieving this resolution by avoiding line broadening due to the ambient pressure makes the practical application of this spectral region for ambient pressure gas sensors unattractive. Furthermore, in molecules that are heteroatomic but possess structural symmetry such as, e.g., benzene (C_6H_6) or carbon dioxide (CO_2), pure rotational states cannot be excited and can therefore not be used for detection.

The optical gas detection scheme used in this work is based on absorption and can be described by the Lambert-Beer law:

$$I(l_{\text{int}}, c) = I_0 e^{-\alpha(\tilde{\nu})cl_{\text{int}}} \quad (3.1)$$

with l_{int} being the interaction length, I_0 the transmitted intensity without gas in the interaction volume, c the concentration of the gas and $\alpha(\tilde{\nu})$ the absorption coefficient of the gas. Measurement of the intensities I_0 and $I(l_{\text{int}})$ and knowledge of the interaction length l_{int} and the absorption coefficient $\alpha(\tilde{\nu})$ enables the determination of the concentration c of the gas. For the calculation of the absorption according to equation (3.1) one has to take into account that the total absorption depends on the overlap of the absorption line and the frequency dependent absorption coefficient $\alpha(\tilde{\nu})$ given by the oscillator strength $S = \int_{\tilde{\nu}_1}^{\tilde{\nu}_2} \alpha(\tilde{\nu}) d\tilde{\nu}$.

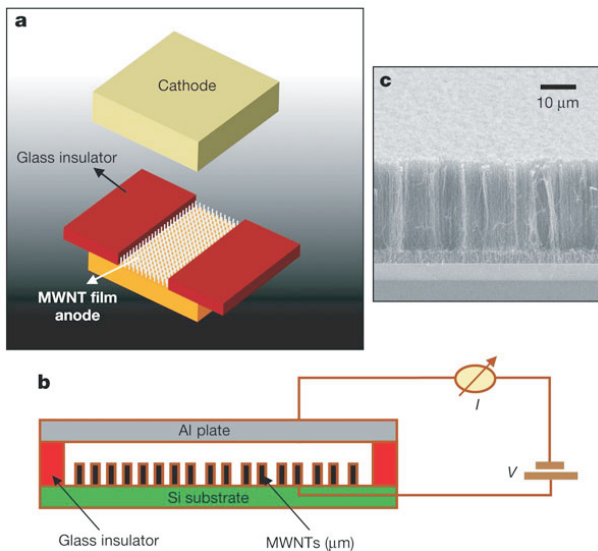


Figure 3.2: Ionization gas sensors based on multiwalled carbon nanotubes [34]. The high electric field at the tips of the carbon nanotubes results in lower externally applied voltages necessary for breakdown as well as increased discharge currents due to the high number of nanotubes, as compared to a conventional ionization gas sensor.

3.2 Alternative concepts

In this section some only recently suggested approaches for gas sensors are briefly introduced. Their working principles are rather different, namely ionization current measurement using carbon nanotubes and IR absorption using a selective narrow-band thermal emitter and a special hollow core fiber, respectively. These approaches are not new concepts in terms of their underlying physical principles, i.e., these principles are also used in conventional state-of-the-art gas sensors. The novelty lies in the fact, that only recently developed fabrication methods and theoretical insight allow an advantageous realization of these structures.

3.2.1 Ionization gas sensors

Ionization gas sensors rely on the fact, that for a certain temperature and pressure any gas will be ionized at a certain voltage. This precisely measurable breakdown voltage provides the *ionization fingerprint* for a specific gas, enabling the identification of the gaseous species. Furthermore, from the discharge current the concentration of the gas can be determined.

Major shortcomings of conventional ionization gas sensors are their usually rather bulky size, high power consumption and high operating voltages.

Utilization of the high electric fields produced at the sharp tips (curvature ≈ 15 nm) of nano-scaled objects, e.g., multiwalled carbon nanotubes, already at relatively low voltages can overcome these problems and might enable compact, battery-powered and safe, i.e., low voltage devices [34].

The principle design of such a carbon nanotube-based ionization gas sensor is shown in fig.3.2. The detector consists of two electrodes separated about $150 \mu\text{m}$ from each other. One electrode, the cathode, is a simple planar Al plate, the second electrode, the anode, consists of vertically aligned multiwalled carbon nanotubes. The separation is guaranteed by a glass insulator. With this design Modi et al. [34] were able to show a reduction of the applied external voltage necessary for breakdown by about 65% and a 6-fold increase in discharge current for air, reference being a comparable design with two planar Al electrodes. Furthermore they demonstrated selective as well as quantitative detection of He, Ar, air, N_2 and O_2 .

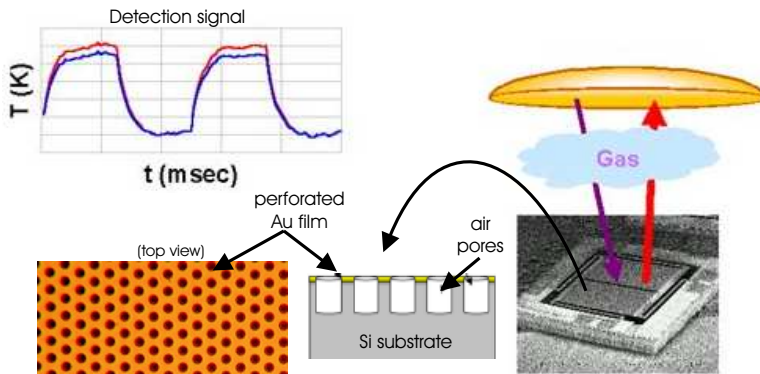


Figure 3.3: Gas sensor design suggested by Ion Optics Inc. based on a narrow band IR emitter. Interaction of a PhC structure, surface plasmons on the Au layer and the perforations in the Au layer acting as grating coupler result in narrow band IR emission. [35][36][37]

This approach fulfills the desired requirement of being a general detection scheme because *any* gas will be ionized at a certain voltage. The selectivity of this approach is quite good for the chemically rather different gases studied in [34]. Whether this approach also offers good selectivity for chemically more similar gases, e.g. alkane-based structures with only minor differences in their side groups, has to be investigated. Also the fabrication of this nanotube-based device might not be straightforward and therefore not suited for mass production of cheap, reliable sensors. Another recently suggested approach related to ionization-based sensors is the utilization of nanocrystalline metal-oxides or noble metals. MoO_3 and Pt are attractive ion emitting materials while AlN and ZnO are potential electron emitting materials.

3.2.2 Frequency selective IR emitter/detector

By combining the properties of a dielectric PhC made of air pores in Si with a periodically perforated metal layer on top of the PhC it is possible to create a narrow-band IR emitter/detector as depicted in fig.3.3¹. The dielectric PhC structure has a high density of states (DOS) for specific frequencies. Thus by heating the device the PhC serves as a reservoir for photons with a specific wavelength. These photons cannot escape through the top metal layer but instead excite surface plasmons at the metal interfaces which can couple to the air region above the metal utilizing the grating momentum provided by the periodically perforated metal layer. By this method a narrow-band IR emitter with enhanced emission/absorption for specific wavelengths, depending on the lattice constants and dielectric materials chosen, can be realized. The intensity of the spectrum emitted by this device is similar to a spectrum emitted by a black body with emissivity of less than 0.1 in all spectral ranges except for a narrow band around the desired frequency. In this spectral region the emissivity almost equals the emissivity of a black body.

The detection scheme itself is as follows: the emitting surface, i.e., the perforated metal layer, will be placed opposite to a mirror. After heating the PhC structure for some time (to typically $\approx 300^\circ\text{C}$) thermal equilibrium will be reached. If now a gas is brought into the space between the emitting surface and the mirror some of the radiation will be absorbed resulting in a decrease of the temperature of the heated PhC/metallic-layer system. This change in temperature serves as

¹<http://www.ion-optics.com/sensorchip.asp>

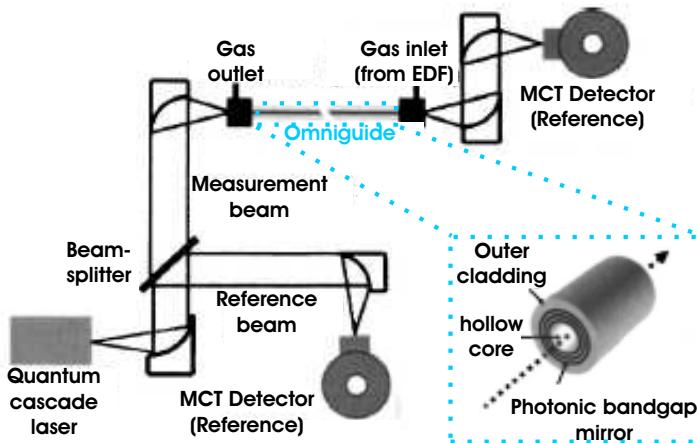


Figure 3.4: Spectroscopic gas sensor using a hollow-core PhC fiber as interaction volume. Its working principle is similar to a White cell where the interaction length between light and gas is prolonged using mirrors. In the PhC fiber the mirroring is achieved by the PhBG of the Omniguide fiber. [28]

the detection signal.

Up to now only the modification of the emission spectrum of the PhC/perforated metallic layer system compared to a black body has been shown. Only recently application of this scheme in a working sensor has been reported. Because the measurement is based on detection of temperature changes the response time of such a detector is limited by its thermal mass and therefore rather slow.

3.2.3 PhC fiber-based spectroscopic gas sensor

A very recent approach concerning realization of novel spectroscopic gas sensors is also based on PhC structures [38] as shown in fig.3.4. Charlton et al. [28] use hollow-core PhC fibers [39] made of cylindrical layers with different dielectric indices resulting in a PhBG. Gas is fed into the hollow core of the fiber and light resonant with an absorption frequency of the gas is fed in along the axis of the fiber. The PhC fiber is designed to have an omni-directional PhBG for the absorption frequency. This leads to multiple reflections of the light along its path through the PhC fiber resulting in a prolonged interaction path, similar to the situation in a *White cell* in which the increased interaction length is achieved by multiple beam folding using mirror optics.

This approach for gas analysis is similar to the method investigated in this work concerning the use of a PhC structure as interaction volume. But it only uses the concept of prolonging the interaction path length by multiple reflections. The concept of utilization of low group velocities is not applied.

But similar to the PhC concept studied in this thesis the PhC fiber approach promises realization of tiny interaction volumes (1.5 ml demonstrated) and along with it a fast response time (8 s demonstrated) of the system. Furthermore it is also a general concept, as the PhBG of the PhC fiber can easily be adjusted to match desired frequencies between 2-20 μm .

A major drawback of the design used by Charlton et al. for detection of ethyl chloride in the lower ppb range is the use of an expensive quantum cascade laser (QCL).

Chapter 4

Methods used in this thesis

4.1 Theoretical methods

In the first part of this chapter the analytical background underlying PhCs will be elucidated and the most important equations are derived. More profound treatments are, e.g., given in [5] and [40]. The second part deals with the numerical treatment of electrodynamics in PhC structures. Different numerical methods were used in this work to investigate various aspects of electrodynamics in PhCs, such as PhBS, field distributions, transmission through PhCs and absorption within the gas filled PhC pores.

4.1.1 Analytical treatment of photonic crystals

First, a relation between Maxwell's equations and PhCs is given, together with a few remarks on symmetry and scaling properties that will prove to be important for PhC-based spectroscopic gas sensors.

4.1.1.1 Maxwell's equations in periodic dielectric media

The Master equation and the transversality requirement The propagation of light in dielectric media is governed by the macroscopic Maxwell equations [41] [42] (in SI units)

$$\nabla \cdot \vec{D} = \rho_{\text{free}} \quad (4.1)$$

$$\nabla \cdot \vec{B} = 0 \quad (4.2)$$

$$\nabla \times \vec{E} = -\frac{\partial \vec{B}}{\partial t} \quad (4.3)$$

$$\nabla \times \vec{H} = \frac{\partial \vec{D}}{\partial t} + \vec{j} \quad (4.4)$$

where \vec{E} and \vec{H} represent the electric and the magnetic field, \vec{D} and \vec{B} the displacement and magnetic induction, ρ_{free} and \vec{j} the free charge density and current density, respectively. For the further treatment linear, homogenous dielectrics, such as Si in the regime used in this work, with frequency independent dielectric constant ϵ_{Si} and magnetic permeability μ_{Si} , are assumed:

$$\vec{D} = \epsilon_0 \epsilon_{\text{Si}} \vec{E} \quad (4.5)$$

$$\vec{B} = \mu_0 \mu_{\text{Si}} \vec{H}, \quad (4.6)$$

μ_0 and ϵ_0 being the free space values for the magnetic permeability and the permittivity, respectively.

For Si the magnetic permeability μ is close to 1. In addition, no free charges and currents are present, i.e., $\rho_{\text{free}} = \vec{j} \equiv 0$. Using these simplifications, the linear relations (4.5), (4.6) and Maxwell's curl equations (4.3), (4.4) together with the ansatz of harmonic waves

$$\vec{H}(\vec{r}, t) = \vec{H}(\vec{r})e^{-i\omega t} \quad (4.7)$$

$$\vec{E}(\vec{r}, t) = \vec{E}(\vec{r})e^{-i\omega t} \quad (4.8)$$

for the magnetic and electric fields, respectively, the time dependence can be separated out and after some algebra the so-called *master equation* for the magnetic field can be derived:

$$\nabla \times \left(\frac{1}{\epsilon_{\text{Si}}(\vec{r})} \nabla \times \vec{H}(\vec{r}) \right) = \left(\frac{\omega}{c} \right)^2 \vec{H}(\vec{r}). \quad (4.9)$$

By solving equation (4.9) for the frequencies ω the PhBS $\omega(\vec{k})$ can be calculated.

In addition, equation (4.9) determines the distribution of the magnetic field $\vec{H}(\vec{r})$ inside the photonic crystal which in turn is fully defined by $\epsilon_{\text{Si}}(\vec{r})$. The electric fields can be derived from the magnetic fields using the curl equation (4.3). Furthermore, the so-called *transversality requirement* has to be fulfilled. It follows from equation (4.2) and states that for a field distribution of the form $\vec{H}(\vec{r}) = \vec{H}_0 e^{i\vec{k} \cdot \vec{r}}$ the relation

$$\vec{H}_0 \cdot \vec{k} = 0 \quad (4.10)$$

must hold, i.e., the waves are transverse.

The scaling law From the linearity of Maxwell's equations, which were the starting point for the derivation of the master equation (4.9), follows that if the dielectric structure $\epsilon(\vec{r})$ making up the PhC is rescaled by a factor s , i.e.,

$$\epsilon'(\vec{r}) = \epsilon(\vec{r}/s) \quad \text{with} \quad \vec{r}' = s\vec{r}, \nabla' \rightarrow \nabla/s \quad (4.11)$$

the frequencies of the PhBS and the field distributions are also rescaled according to

$$\vec{H}'(\vec{r}) = \vec{H}(\vec{r}/s) \quad (4.12)$$

$$\omega' = \omega/s. \quad (4.13)$$

This property makes the use of PhCs in spectroscopic gas sensors rather interesting, because by simply changing the lattice constant of the PhC the PhBS can be shifted to specific resonance frequencies of various gases.

Symmetry and coupling A 2D PhC, i.e., a PhC being periodic in the x - y -plane and extending infinitely along the z -direction as schematically depicted in fig.4.1a, has mirror symmetry with respect to the x - y -plane. The solutions to equation (4.9) can be separated into TE modes having field components $\vec{E}_z = \vec{H}_x = \vec{H}_y = 0$ and TM modes with field components $\vec{E}_x = \vec{E}_y = \vec{H}_z = 0$. This property can be utilized when designing a PhC to be used in a gas sensor. For example, the

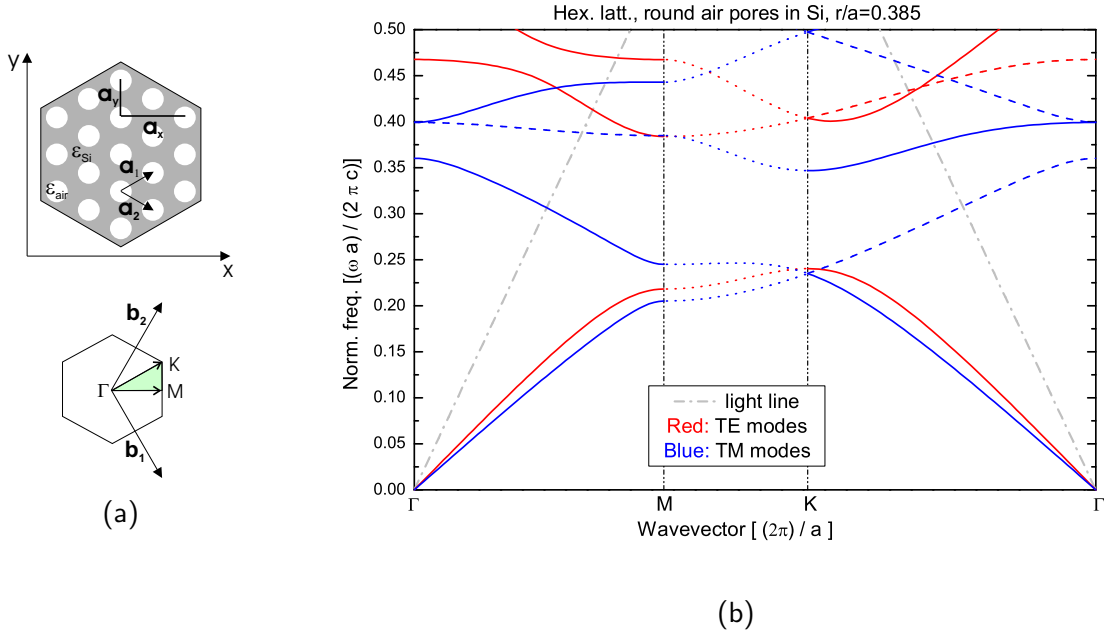


Figure 4.1: **a)** Real and reciprocal space of a 2D PhC with hexagonal lattice symmetry. \vec{a}_1 , \vec{a}_2 and \vec{b}_1 , \vec{b}_2 represent the basis vectors in real and reciprocal space, respectively (for details see A.1.1). The highlighted green region represents the irreducible Brillouin zone (BZ) of the hexagonal lattice. **b)** Photonic band structure of a PhC consisting of round air pores in Si ($\epsilon_{Si} = 11.6$), arranged in a hexagonal lattice (calculation using MPB 4.1.2.1). Due to mirror symmetry of the structure with respect to the x - y -plane the modes in the PhBS split up into TE (red) and TM (blue). Due to their field symmetry, solid (dashed) lines allow (do not allow) coupling to plane waves. The dotted lines between and the M and the K points symbolize that no classification as coupling or non-coupling bands is made because each point corresponds to a different direction in real space (seen from the Γ point).

TE polarized part of incoming, unpolarized light with a specific frequency could be used for the gas detection, while the TM polarization having the same frequency could be used as a reference signal, or vice versa.

To allow coupling of incoming plane waves to PhC modes, a symmetry requirement has to be fulfilled. The symmetry of the PhC mode under consideration has to match the symmetry of the incoming plane wave. Solid red and blue lines in fig.4.1b represent TE and TM modes, respectively, whose symmetry of the important field component H_z and E_z , respectively, matches the symmetry of the impinging plane waves along the ΓM and ΓK directions. This will be treated in more detail in chapter 5. The dotted lines in fig.4.1b represent the normalized frequencies at the endpoint of different \vec{k} -paths starting at the Γ point and ending on the connector of M and K . The corresponding field patterns transform accordingly. Since the symmetry representations at the M and K points are different, namely $C_{2\nu}$ and $C_{3\nu}$, respectively, some bands keep their coupling property along ΓK as well as along ΓM (e.g., 1st TE and TM bands), while other bands couple only along either ΓM or ΓK (e.g., 2nd TM band, 3rd TM band).

The master equation as an eigenvalue problem The master equation (4.9) can be rewritten in the form of an eigenvalue problem using the hermitian operator Θ :

$$\Theta \vec{H}(\vec{r}) = \left(\frac{\omega}{c}\right)^2 \vec{H}(\vec{r}) \quad (4.14)$$

$$\Theta \vec{H}(\vec{r}) = \nabla \times \left(\frac{1}{\epsilon(\vec{r})} \nabla \times \vec{H}(\vec{r}) \right) \quad (4.15)$$

From the Hermiticity of Θ it follows that its eigenvalues are real and that eigenmodes for different eigenvalues are orthogonal.

Bloch modes as solution to the master equation From the periodicity of the PhC follows based on Bloch's theorem, that the solutions to the master equation (4.9) have the form of so-called *Bloch modes*

$$\vec{H}_{n,\vec{k}}(\vec{r}) = e^{i\vec{k}\cdot\vec{r}} u_{n,\vec{k}}^H(\vec{r}) \quad (4.16)$$

with n being the band index, \vec{k} the wavevector and $u_{n,\vec{k}}^H(\vec{r})$ a function having the periodicity of the underlying PhC lattice, i.e., $u_{n,\vec{k}}^H(\vec{r} + \vec{R}) = u_{n,\vec{k}}^H(\vec{r})$ with $\vec{R} = m_1\vec{a}_1 + m_2\vec{a}_2 + m_3\vec{a}_3$ being a vector of the real space lattice, i.e., a linear combination of the real lattice basis vectors \vec{a}_1, \vec{a}_2 and \vec{a}_3 with integers m_1, m_2 and m_3 .

To find the solution for the $\vec{H}_{n,\vec{k}}(\vec{r})$, the $u_{n,\vec{k}}^H(\vec{r})$ have to be determined. This can be done by inserting equation (4.16) into the master equation (4.9) yielding

$$\left(i\vec{k} + \nabla\right) \times \frac{1}{\epsilon_{Si}(\vec{r})} \left[\left(i\vec{k} + \nabla\right) \times u_{n,\vec{k}}^H(\vec{r}) \right] = \frac{\omega^2}{c^2} u_{n,\vec{k}}^H(\vec{r}). \quad (4.17)$$

Utilizing that the functions $\epsilon_{Si}(\vec{r})$ and $u_{n,\vec{k}}^H(\vec{r})$ are periodic, $\epsilon_{Si}(\vec{r})$ and $u_{n,\vec{k}}^H(\vec{r})$ can be expanded into Fourier series according to

$$\epsilon_{Si}(\vec{r}) = \sum_{\vec{G}} \zeta_{\vec{G}} e^{i\vec{G}\cdot\vec{r}} \quad (4.18)$$

$$u_{n,\vec{k}}^H(\vec{r}) = \sum_{\vec{G}} u_{\vec{G}}^H e^{i\vec{G}\cdot\vec{r}} \quad (4.19)$$

with $\zeta_{\vec{G}}$ and $u_{\vec{G}}^H$ being Fourier coefficients and $\vec{G} = m_1\vec{b}_1 + m_2\vec{b}_2 + m_3\vec{b}_3$ a vector of the reciprocal lattice (m_1, m_2, m_3 integers). This leads to a system of equations in \vec{k} space from which by comparison of the corresponding coefficients the solutions $\omega_{n,\vec{k}}$ and $\vec{H}_{n,\vec{k}}(\vec{r})$ for each \vec{k} can be derived. But due to the generally complex structure of ϵ_{Si} in PhCs analytical solutions to the master equation can be found only for special cases as ,e.g., 1D layer systems, so numerical methods have to be used.

4.1.2 Numerical treatment of photonic crystals

While in the preceding section an analytical treatment of electromagnetics in PhCs was given, this section describes different numerical schemes used in this work to find either the eigenvalues and eigenstates in a PhC or to calculate transmission through and absorption enhancement within a PhC.

4.1.2.1 Plane wave expansion (PWE)

For computing the band structures and electromagnetic modes of the PhCs the MIT Photonic Bands (*MPB*) package - a free program developed at the Massachusetts Institute of Technology (MIT) by Steven G. Johnson - was used in this work [43]. *MPB* calculates eigenstates and eigenmodes of periodic structures in reciprocal space based on equation (4.17) using a plane wave expansion method (*PWE*). The PhC structure is specified by defining a unit cell in real space which is then periodically repeated. For the expansion of the fields, i.e., for the expansion of the functions $u_{n,\vec{k}}^H(\vec{r})$, the plane wave basis in equation (4.19) is used.

However, the periodic distribution of the dielectric $\epsilon_{\text{Si}}(\vec{r})$ is not expanded as described in equation (4.18) since for high dielectric contrasts ($\Delta\epsilon = 11.6$ in the macroporous Si material system) a very large number of terms in the expansion is necessary to sufficiently represent the dielectric distribution. On one hand this requires high computational power and memory and on the other hand - even with a high number of expansion terms - overshoots at the high contrast air/Si interfaces cannot be completely avoided.

A different approach drastically reducing the necessary computational power while still sufficiently representing the distribution of the dielectric materials is taken instead. When calculating equation (4.17) the following scheme is applied:

$$\left(i\vec{k} + \nabla\right) \times \dots \text{IFFT} \dots \widetilde{\epsilon_{\text{Si}}^{-1}} \dots \text{FFT} \dots \left[\left(i\vec{k} + \nabla\right) \times \dots\right] = \dots \quad (4.20)$$

First the curl in \vec{k} space is computed and then transferred into real space by a Fast-Fourier-Transform (*FFT*). Now the inverse $\widetilde{\epsilon_{\text{Si}}^{-1}}$ of the dielectric function ϵ_{Si} is multiplied in real space and then the whole equation is transferred back into \vec{k} space by applying an inverse Fast-Fourier-Transform (*IFFT*) and again the curl is taken. The solutions to this set of equations obtained after using the above techniques are the normalized eigenfrequencies $(\omega_{n,\vec{k}}a)/(2\pi c_0) \equiv a/\lambda$ and the distributions of the electric and magnetic fields in the infinite PhC. These are the stationary states because in the above derivation the time harmonic part has been separated out and therefore the temporal evolution of the fields is not accessible.

4.1.2.2 Finite-difference time-domain (FDTD)

In contrast to the *PWE* method which works in Fourier space, in the Finite-difference time-domain (*FDTD*) method the temporal evolution of electromagnetic fields in real space is calculated. For this purpose the differential Maxwell equations (4.1)-(4.4) are transformed into difference equations on a spatial and temporal grid. The temporal evolution from $t \rightarrow t + \Delta t$ of the magnetic field can be derived from the right hand side of equation (4.3) by rewriting

$$-\mu_0 \frac{\partial \vec{H}}{\partial t} = \lim_{\Delta t \rightarrow 0} \left(-\mu_0 \frac{\vec{H}(\vec{r}, t + \Delta t) - \vec{H}(\vec{r}, t)}{\Delta t} \right). \quad (4.21)$$

The left hand side of the equation (4.3) relates this to the electric field $\vec{E}(\vec{r}, t)$. By solving for $\vec{H}(\vec{r}, t + \Delta t)$ it is possible to calculate the magnetic field after a time step Δt at the spatial point \vec{r} from the electric and magnetic fields $\vec{E}(\vec{r}, t)$ and $\vec{H}(\vec{r}, t)$, respectively, at time t using

$$\lim_{\Delta t \rightarrow 0} \left(\vec{H}(\vec{r}, t + \Delta t) = -\nabla \times \vec{E}(\vec{r}, t) \frac{\Delta t}{\mu_0} + \vec{H}(\vec{r}, t) \right). \quad (4.22)$$

As a rule of thumb the spatial grid size should be on the order of about $a/10$ - $a/20$ to ensure sufficient representation of the dielectric distribution while keeping the necessary amount of computational time bearable, a being the lattice constant of the PhC. The choice of the grid depends on the geometry studied. For 3D problems a popular and proven choice is the so-called Yee-cube [44] having a discretization optimally adapted to Maxwell's equations. This algorithm is called *leap frog* because it jumps in time from \vec{H} at time t to \vec{E} at time $t + 0.5\Delta t$ to \vec{H} at $t + \Delta t$, ... while using spatially centered differences for the field values [45].

For the 2D calculations performed in this work usually a square grid with a grid size of $a/16$ was used. For a regular hexagonal lattice employed as the interaction region of the PhC gas sensor a rectangular grid with side lengths of $\sqrt{3}a$ along ΓM and a along ΓK directions is also a reasonable choice matching the symmetry of the underlying PhC lattice. For calculations with distorted hexagonal lattices or the ARL concept studied in this work rectangular unit cells in the different regions can also be used, but their size for optimal representation of the underlying structure is different. Therefore a square grid was chosen for the FDTD calculations.

To ensure stability of the FDTD algorithm the so called *Courant stability criterion* has to be fulfilled. It states that for a grid spacing of Q_1, Q_2, Q_3 the time step Δt has to be chosen to fulfill

$$(\Delta t)^2 < \frac{1}{Q_1^2} + \frac{1}{Q_2^2} + \frac{1}{Q_3^2} \quad (4.23)$$

where atomic units¹ are used for the length and time scales. Figuratively this means that only waves with temporal periods of Δt having vacuum wave vectors $|\vec{k}| = 1/(c_0 t)$ larger than the vectors $k_{\max} = 2\pi/(1/Q_1^2 + 1/Q_2^2 + 1/Q_3^2)$, that can just be represented on the grid, are considered. In the FDTD code employed for most of the 2D calculations in this work (CrystalWave²) a square grid of size $Q_1 = Q_2 = a_0/16$ ($a_0 = 4.2 \mu\text{m}$) was used and the time step Δt was internally set to

$$\Delta t = 0.99 \sqrt{\frac{1}{3}} \frac{Q_1}{c_0}. \quad (4.24)$$

Comparison of equations (4.23) and (4.24) shows that the general Courant stability criterion is fulfilled. The time step in equation (4.24) is on the order of 0.5 fs for the parameters used. Thus by calculating 2^{17} time steps³ the evolution of the fields is studied for about 65 ps. In free space light travels in this time a distance of about 2 cm. In *ordinary* dielectrics with refractive index $n_{\text{mat}} \lesssim 4$ the covered distance is on the order of a few mm. These distances correspond to several hundred unit cells of the PhC studied in this work ($a \simeq \mu\text{m}$) therefore seeming to be sufficient to study light propagation in a PhC consisting of several ten by ten unit cells. But it has to be taken into account that here we are dealing with flat bands in the PhC band structure corresponding to group velocities of a few tenths to hundredths of c_0 . Therefore it has to be carefully observed whether a steady state condition at the end of the calculation is really achieved. The limiting factor in the FDTD calculations performed with CrystalWave was the limited amount of useable memory (< 2GB) on a standard 32bit Windows[®]-based desktop PC (Pentium 4 processor) limiting the

¹ $Q_{1,2,3}$ in multiples of the Bohr radius $a_B = 5.3 \times 10^{-11}$ m; Δt in multiples of the Bohr time $t_B = 2.4 \times 10^{-17}$ s

²Commercially available software from PhotonDesign (www.photond.com)

³The number of time steps is practically limited by the amount of available computer memory.

number of possible time steps to 2^{16} - 2^{17} while still using an appropriate grid size⁴.

4.1.2.3 Finite element method (FEM)

Like the PW-based approach used by MPB, the Finite Element (*FE*) method operates in the frequency domain, i.e., only the stationary state is computed. The FE method is based on discretization of the Helmholtz equation on a, for 2D calculations typically triangular, grid. During the derivation of the Helmholtz equation the time harmonic part of the electromagnetic wave under study was separated and therefore no temporal evolution of the fields can be treated by the FE method. But it is still possible to vary the phase of the complex fields. As a rule of thumb the grid size ΔQ should be on the order of $\lambda_{\text{mat}}/5$ - $\lambda_{\text{mat}}/10$, λ_{mat} being the wavelength in the material, i.e., the vacuum wavelength divided by the refractive index of the material.

In FEM the solution is approximated as a superposition of functions \vec{v}_j . Each function is localized on a small tile of the FEM computational domain. The periodicity of the PhC structure is taken into account by using periodic boundary conditions. The transversality requirement is implemented by the choice of appropriate ansatz functions as well as explicit selection of divergence free solutions in the FEM algorithm. Expanding the $u_{n,\vec{k}}^H(\vec{r})$ in the Bloch ansatz (4.16) into the localized functions \vec{v}_j and substitution into the master equation (4.9) followed by a minimization of the residuum in each element leads to a system of $j = 1 \dots N$ equations of the form

$$\int d\vec{r} \vec{v}_j \left\{ (\nabla + i\vec{k}) \times \left[\frac{1}{\epsilon_{\text{mat}}(\vec{r})} (\nabla + i\vec{k}) \times u_{n,\vec{k}}^H \right] - \omega^2 u_{n,\vec{k}}^H \right\} = 0. \quad (4.25)$$

This can be transformed into a matrix representation and numerically be solved by standard algorithms. Due to the locality of the FEM approach the matrices are only sparsely populated which makes the FEM approach relatively fast.

In this work two FEM codes were used. *HelmPole* was developed at the Konrad-Zuse-Zentrum für Informationstechnik (*ZIB*⁵) in Berlin, Germany. *FEMLAB* is a commercially available multi-physics simulation software. Both softwares are Linux[®]-based which makes it possible to take full advantage of the computational power (4 Opteron processors, 64bit) and RAM (16GB) of a workstation available at the University of Paderborn.

4.2 Experimental methods

4.2.1 Macroporous Si fabrication process

The constraints in vertical structuring of Si using conventional techniques like parallel plate reactive ion etching (*RIE*), inductively coupled plasma etching (*RIE-ICP*) or wet etching (e.g., using potassium hydroxide (*KOH*)), results from their limited selectivity. In those cases the etching not only takes place along the z-direction but also, even though slowly, in other directions. The etching method used in this work to produce ordered arrays of macropores in Si is based on a different principle, namely photo-electrochemical etching (*PECE*). This process is described below

⁴Meanwhile PhotonDesign took one of our suggestions and develops a Linux[®]/Unix[®]-based version of CrystalWave to allow more computer memory to be used

⁵www.zib.de

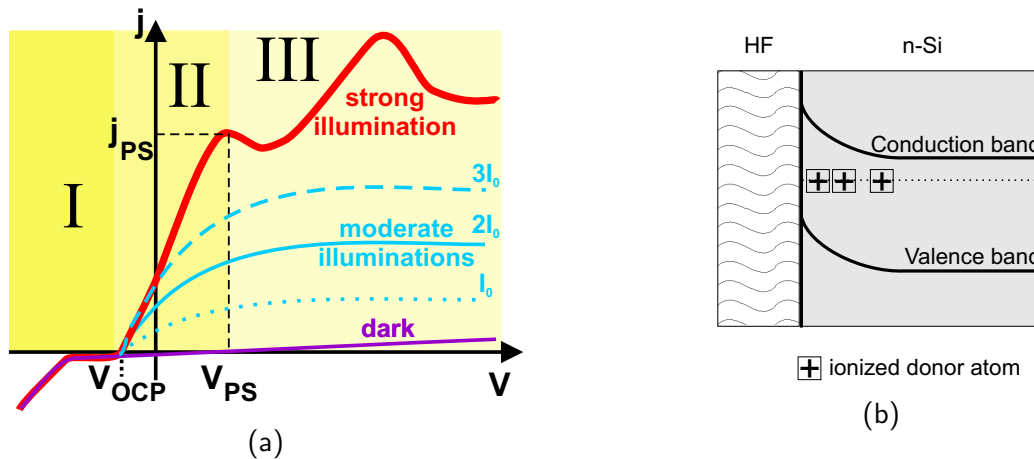


Figure 4.2: **a)** Schematic plot of current density across the HF/Si interface for n-Si under no (purple), medium (blue) and strong (red) illumination. **b)** Unbiased HF/n-Si Schottky-like contact.

following the model for macropore formation by Lehmann [46][47]. More comprehensive reviews of different pore regimes and pore formation mechanisms and alternative models in p-type and n-type Si can be found in [48], [49], [50] and [51].

4.2.1.1 Electrochemical dissolution of Si: the HF/n-Si contact

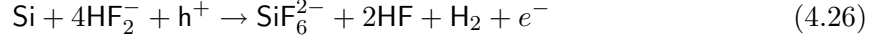
While Si is easily etched in aqueous alkaline solutions it is quite stable in most aqueous acids. However, hydrofluoric acid (HF) is an exception to this general observation. Fig.4.2a shows the current density j across the HF/n-Si interface vs. the applied voltage V for different illumination conditions. In the regime of cathodic currents (I in fig.4.2a) the Schottky-like HF/n-Si contact is forward biased. The current is determined by the majority charge carriers, i.e., the electrons - independent of the illumination state - and leads to the reduction of the H^+ ions in the acidic solution followed by formation of hydrogen (H_2).

The regime of anodic currents (II and III in fig.4.2a) is the more interesting one. Fig.4.2b shows the arrangement of the valence and conduction bands, respectively, within n-Si in contact with HF. When the semiconductor Si is brought into contact with the electrolyte HF the situation resembles a Schottky contact in which the rather conductive electrolyte represents the metal. The different chemical potentials of the aqueous HF and the Si will adapt. This leads to the formation of a Helmholtz double layer in the electrolyte and a surface charge resulting from the ionized donor atoms in the Si from which a depletion of majority charge carriers (electrons in n-Si) at the HF/Si interface follows. Due to the mobile ions in the electrolyte the width of the Helmholtz double layer is only a few nm while due to the stationary nature of the donors in Si the depletion region in n-Si is on the order of a few μm wide.

If no illumination is applied to the n-Si, a small (anodic) dark current resulting from thermally generated holes is observed (purple line fig.4.2a).

If the Si is strongly illuminated the HF/n-Si contact behaves like an HF/p-Si contact (red line in fig.4.2a). An increase in applied voltage V leads to an increase in current across the HF/Si interface. For anodic currents below the critical current density j_{PS} and $V < V_{PS}$ (II in fig.4.2a)

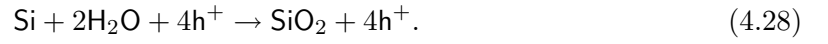
divalent⁶ dissolution of Si occurs along with the formation of hydrogen. Here the etching current is limited by charge carrier supply from the Si electrode and porous Si is formed. A suggested reaction is



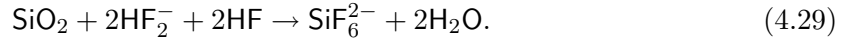
with e^- and h^+ denoting an electron and a hole in the Si [49]. In aqueous HF electrolytes the critical current density j_{PS} was experimentally found to only depend on electrolyte concentration c_{HF} (in weight %) and electrolyte temperature T_{HF} and can be described by

$$j_{\text{PS}} = C c_{\text{HF}}^{3/2} e^{-E_a/(k_{\text{B}}T_{\text{HF}})} \quad (4.27)$$

with C being a constant of 3300 A/cm^2 , $E_a = 0.345 \text{ eV}$ and k_{B} being Boltzmann's constant [46]. For anodic currents and $V > V_{\text{PS}}$ (III in fig.4.2a) tetravalent dissolution of Si is observed. In a first step, under consumption of 4 holes, an anodic oxide is formed on the Si electrode:



In a second step this oxide is then chemically etched by the fluorine species HF, $(\text{HF})_2$ or HF_2^- in the electrolyte [49]



Here the current is limited by the chemical reaction rate during the removal of the SiO_2 . As a consequence the Si electrode is electropolished, i.e., all Si surface atoms are removed uniformly. For medium illumination intensities the IV-curve of the HF/n-Si is similar to the blue curves in fig.4.2a. Here the current density j across the interface is below j_{PS} . j is limited by charge supply from the Si electrode and therefore porous Si is formed.

The electronic holes necessary for the dissolution of Si at the HF/Si interface are created by illuminating the sample with light energy $E_{\nu} = h\nu \geq E_{\text{g,Si}} = 1.1 \text{ eV}$. Due to the high absorption of Si for the IR light used ($\lambda \approx 880 \text{ nm}$, $\alpha \approx 10^2 \text{ cm}^{-1}$ [49]) electron hole pairs are produced within the first few μm from the air/Si interface.

4.2.1.2 Formation of ordered macropores in n-type Si

For the formation of porous Si it is necessary that the current density across the HF/Si interface is smaller than j_{PS} . According to the diameter d_{Pore} of the pores three regimes are distinguished: microporous Si with $0 \text{ nm} \leq d_{\text{Pore}} \leq 2 \text{ nm}$, mesoporous Si with $2 \text{ nm} < d_{\text{Pore}} \leq 50 \text{ nm}$ and macroporous Si with $50 \text{ nm} < d_{\text{Pore}}$. For p-Si $j < j_{\text{PS}}$ can only be fulfilled for potentials $V_{\text{OCP}} < V < V_{\text{PS}}$. For the n-Si used in this work $j < j_{\text{PS}}$ can be achieved for potentials $V_{\text{OCP}} < V$ by appropriate adjustment of the illumination. Stable macropore growth is possible for $j < j_{\text{PS}}$ and $V_{\text{PS}} < V$. The ratio j/j_{PS} only controls the average porosity p of the sample. The x - y -positions as well as the diameters of individual pores show a random distribution under the constraint of the average porosity being $p = j/j_{\text{PS}}$. For *conventional*⁷ PhCs it is yet necessary to have a periodic, and not a random, distribution of materials with different dielectrics. To achieve

⁶divalent (tetravalent) means that in the external electrical circuit 2 (4) electrons are necessary for the removal of one Si atom from the electrode.

⁷Photonic band gaps as a characteristic of photonic crystals can also be observed for structures possessing only local order [52] or quasicrystals [53] [54]

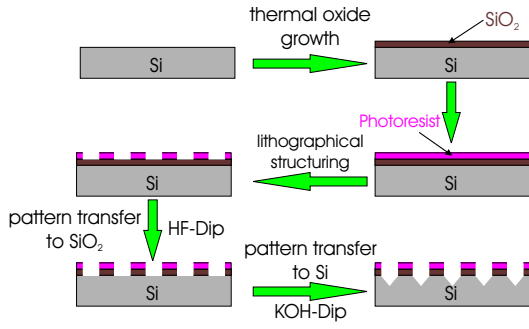


Figure 4.3: Lithographical prestructuring of a Si-wafer for subsequent photo-electrochemical etching.

this it is necessary to determine the sites at which the macropores should grow. This is done by lithographically defining a periodic pattern on top of the Si wafer and subsequent transfer of the pattern into the Si as shown in fig.4.3. By this procedure, so-called *etch-pits* in the form of inverse pyramids are generated which serve as starting points for the subsequent pore growth. The porosity of such an ordered macropore array is given by

$$p = \frac{j}{j_{PS}} = \frac{A_{Pores}}{A_{Sample}} \quad (4.30)$$

with A_{Pores} being the total pore area and A_{Sample} the total HF/Si interface area. Fig.4.4 schematically shows the principle of photo-electrochemically etching ordered macropore arrays. Electron-hole pairs are generated by appropriate illumination of the back of the n-Si wafer. Due to the anodic potential the electrons are sucked away into the voltage source while the holes diffuse through the wafer towards the HF/Si interface where a space charge region (SCR) has formed. To ensure that the holes can reach the HF/Si interface high quality float-zone Si has to be used in which the diffusion length of the holes is on the order of the thickness of the Si wafer. The shape of the SCR follows the physical shape at the interface and is therefore curved. Because the electric field lines are perpendicular to the HF/Si interface the electronic holes that come into the vicinity of the pore tips are focused onto the pore tips where they promote the dissolution of Si. The width x_{SCR} of the SCR depends on the applied anodic voltage and can be described by

$$x_{SCR} = \sqrt{\frac{2\epsilon_0\epsilon_{Si}V_{eff}}{qN_D}} \quad (4.31)$$

where ϵ_0 is the free space permittivity, ϵ_{Si} is the dielectric constant of Si, N_D the doping density of Si and $V_{eff} = V_{bi} - V - k_B T/e$ is the effective potential difference between the electrolyte and the Si anode. $V_{bi} \approx 0.5$ V represents the built-in potential of the contact, V the applied external potential ($k_B T \approx 25$ meV at room temperature). The applied anodic bias has to be chosen high enough such that all of the incoming electronic holes are focused onto the pore tips and none of them penetrate into the Si wall remaining between two pores. If this condition is fulfilled the pore walls are passivated against dissolution.

The porosity of such an ordered array of macropores with radius r_{Pore} , e.g., arranged in a hexagonal lattice with lattice constant a , can be expressed as

$$p_{hex} = \frac{2\pi}{\sqrt{3}} \left(\frac{r_{Pore}}{a} \right)^2 \quad (4.32)$$

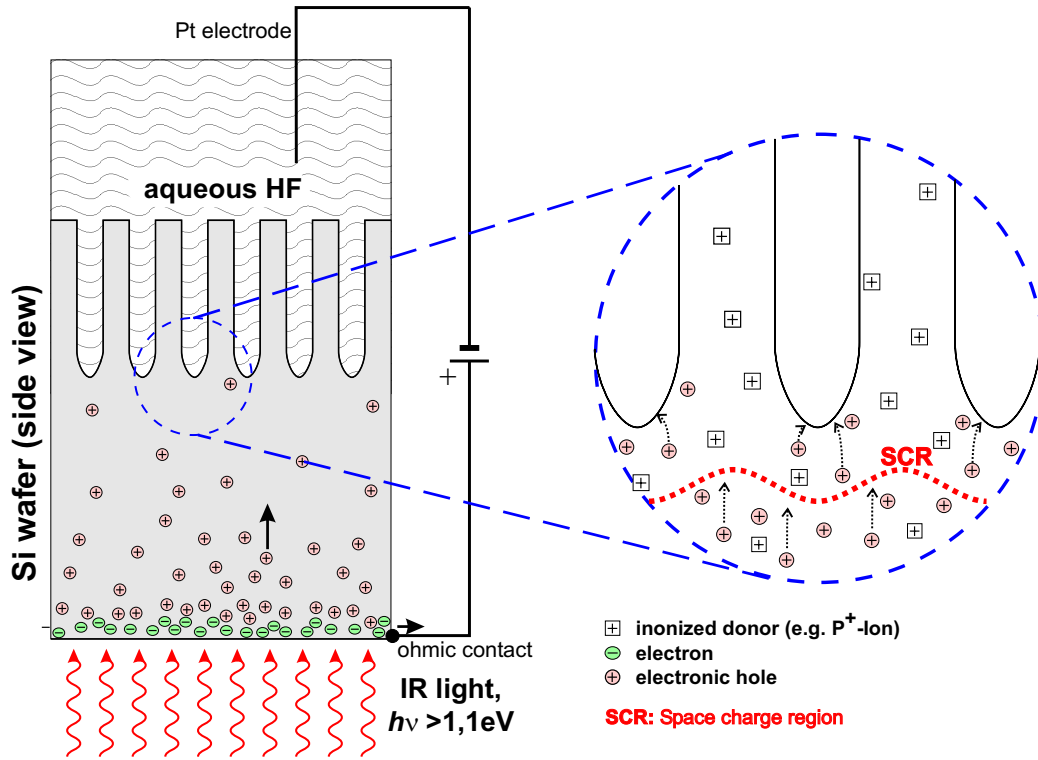


Figure 4.4: Formation of ordered macropores by photo-electrochemical etching of *n*-Si under backside illumination using an anodic potential.

The growth speed of the pores along the [100] direction in the model of Lehmann only depends on the temperature T_{HF} and the concentration c_{HF} of the electrolyte and can be described by

$$v_{100} = \frac{j_{\text{PS}}}{n_{\text{val}}qN_{\text{Si}}} \quad (4.33)$$

with N_{Si} being the particle density of Si ($5 \times 10^{22} \text{cm}^{-3}$) and $n_{\text{val}} \approx 2.6$ the dissolution valence for the dissolution process, i.e., the number of electrons supplied by the external circuit needed for the dissolution of 1 Si atom [46].

4.2.2 Characterization

4.2.2.1 Optical Characterization by FTIR spectroscopy

Fourier-transform infrared (FTIR) spectroscopy is based on the interference of two beams within a Michelson interferometer as shown in fig.4.5a.

Radiation from a light source with spectrum $I(\nu)$, e.g., a heated SiC rod (*GloBar*), is split up into two beams by a beamsplitter. One beam is reflected back by a fixed mirror while the second beam is reflected back by a mirror moving with constant speed v . After having passed the beamsplitter a second time the now parallel beams interfere on a detector. By changing the position of the moveable mirror by $\Delta x = vt$ the difference in optical path Δl of the two beams becomes $\Delta l = 2\Delta x$. For radiation from the light source of wavelength λ constructive interference on the detector can be observed for $\Delta l = m\lambda$ while destructive interference results

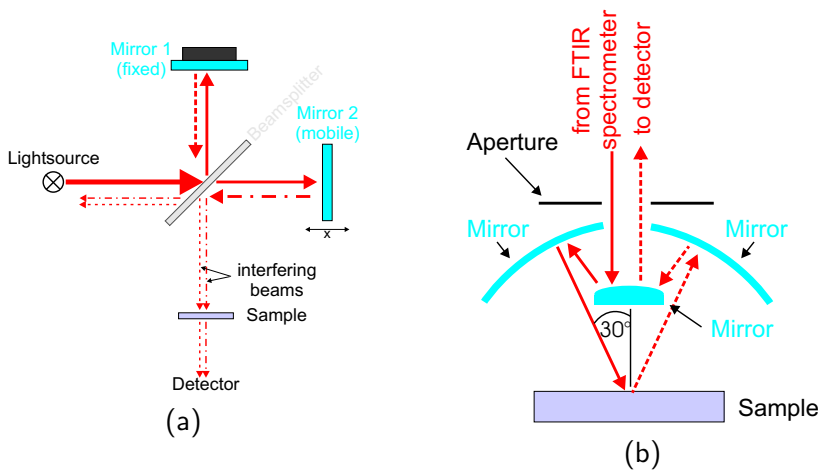


Figure 4.5: **a)** Working principle of a Michelson interferometer used in a Fourier-transform infrared (FTIR) spectrometer. **b)** Cassé-grain optics used in the IR microscope connected to the FTIR spectrometer.

for $\Delta l = (m + 1/2)\lambda$ with integer m . The detector signal $S(t)$, the so-called *interferogram*, contains all the information of the incident spectrum $I(\nu)$. The spectrum $I(\nu)$ can be obtained from $S(t)$ by a Fourier transformation (usually in the form of a FFT performed by the computer controlling the spectrometer). The dynamic of the FTIR spectrometer is about 50 dB.

During this work a *Bruker IFS 66* FTIR spectrometer was used for transmission and reflection measurements. The latter were made using a *Hyperion* IR microscope connected to an external port of the FTIR spectrometer. To measure the reflectance over a spectral range from about 1.5-20 μm mirrors are used in the microscope optics instead of expensive lenses for the IR spectral range, as shown in fig.4.5b. The use of Cassé-grain type optic leads to an opening angle of about 15° and 30° for the two available objectives, respectively. Two moveable, perpendicular slits allow selection of the sample area under investigation. A polarizer in the microscope is used to switch between TE and TM measurements. Depending on the spectral range under investigation CaF and a KBr beamsplitters were used, respectively, for VIS and IR, together with a halogen lamp or a GloBar. A liquid nitrogen cooled Mercury-Cadmium-Telluride (*MCT*) detector was used.

4.2.2.2 Optical Characterization using a QCL

Transmission measurements through a macroporous Si PhC consisting of several hundred pore rows is a challenging task [55]. The emitted power of a thermal emitter, e.g., a GloBar is rather low in the IR ($\leq \text{mW}/(\text{mm}^2 \text{ sterad})$ at $\approx 1000 \text{ K}$ in the spectral range from 9.5-10.5 μm). In addition the loss due to scattering at possibly rough pore walls was also not known. A quantum cascade laser [56] can be used to counteract the first factor. The used setup is shown in fig.4.6. A pulsed (pulse length 50 ns) QCL emitting at a center wavelength of 10.34 μm with a repetition frequency of 9.9 kHz served as high intensity light source. Tuning of the wavelength is achieved by the increase in temperature of the QCL during the pulse. A photovoltaic Mercury-Cadmium-Zinc-Telluride detector cooled by a Peltier element was used. The signal from this fast detector is synchronized to the laser repetition frequency and directly read by a digital oscilloscope. Due to the high output power of the QCL and the sensitive detector a 50 dB dynamic is achieved.

Plane and curved gold mirrors are used for focusing and guiding the laser beam. Key features of this setup are the two mirror objectives. Together with the first pinhole that limits the laser beam diameter to a size of 300 μm , a focal spot size of about 70 μm on the sample surface can be

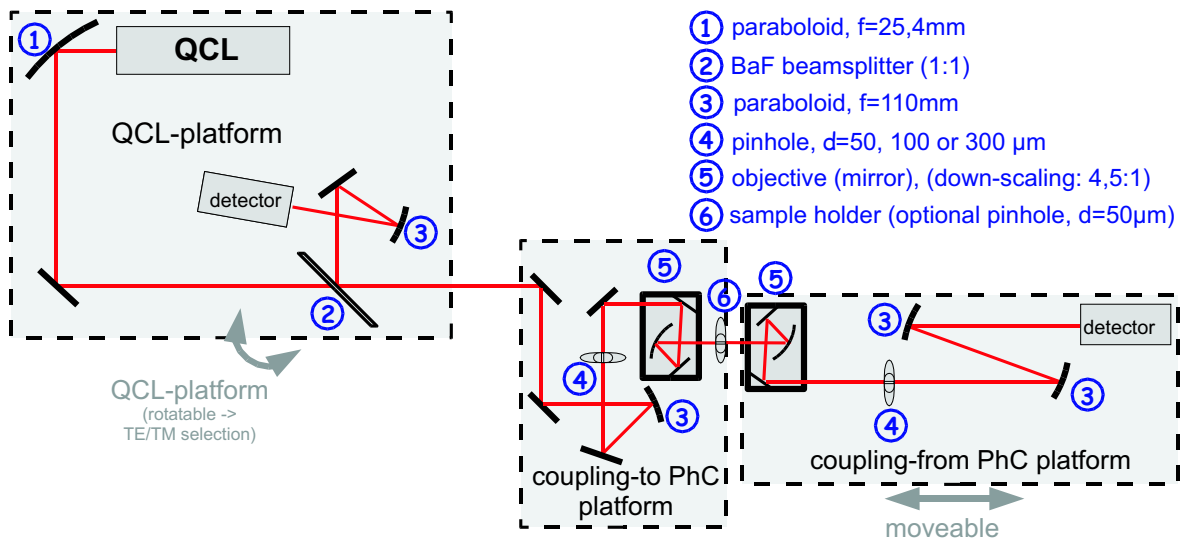


Figure 4.6: Quantum cascade laser setup available at the Fraunhofer Institute for Physical Measurement Techniques (FhG IPM) in Freiburg, Germany.

achieved, giving good control of where the light is coupled into the PhC and from where it is detected on the output side. The position of the coupling spots can be verified by an eyepiece. Since a QCL naturally emits in TM polarization, the laser itself has to be turned by 90° around the beam axis to perform measurements in TE polarization.

4.2.2.3 Surface characterization by AFM

Atomic force microscopy (AFM), also known as scanning force microscopy (SFM), is a powerful tool to examine surfaces as well as tiny objects located on substrate materials. In this work AFM was used to characterize the surfaces obtained by PECE trenches. From the three widespread operational modes, namely non-contact mode, contact mode and tapping mode, the latter was chosen. Its working principle is depicted in fig.4.7⁸. A tiny tip, that is attached to a cantilever, is scanned across the surface under investigation. In the tapping mode the cantilever oscillates at a frequency close to its resonance frequency with amplitudes of several 10 nm. The tip is positioned slightly above the sample surface so that it touches the surface only for a small moment during its oscillation. To detect the tiny deflection caused by tip/surface interactions laser light is reflected off from the backside of the cantilever to a photodiode array. The deflection of the laser spot on the detector is used as measurement signal. Compared to the other two mentioned operating modes, tapping mode offers the advantages to allow high lateral resolution while interacting only very faint (forces of a few pN between tip and sample are sufficient) with the sample under investigation.

⁸Scheme in parts supplied by D. Zschech, MPI MSP Halle

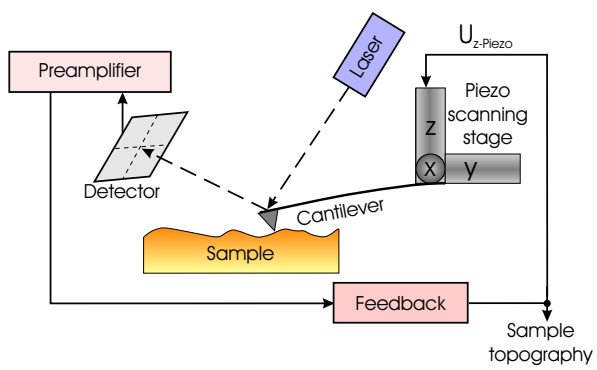


Figure 4.7: Working principle of an atomic force microscope (AFM). A cantilever is used to probe the surface of a sample. The position of light deflected from the cantilever is detected.

Chapter 5

Design of photonic crystal gas sensors

In this chapter the theoretical background for the realization of a PhC-based spectroscopic gas sensor is investigated. Starting from the basic requirements such a PhC should fulfill, the design of the PhC employed as interaction volume is developed. Thereafter, a strategy for the connection of the PhC interaction volume to the outside world is investigated.

5.1 Software used in this work: overview and rating

At this point a few words about the strengths and weaknesses of the described numerical methods concerning the actual design of a PhC-based spectroscopic gas sensor should be said.

Table 5.1 summarizes the different numerical schemes used in this work and their capabilities as well as the available hardware, the latter being one of the limiting factors in Windows[®]-based FDTD schemes.

In this work the free MIT Photonic Bands (MPB) software was used for bandstructure and group velocity calculations as well as field distribution computations. Because the used PWE method assumes *infinite* structures it does not allow transmission calculations. In principle it can be used for simulations of *finite* structures but this requires the use of supercells with unfavorable concomitants such as backfolding of bands at the Brillouin zone boundaries making the analysis of the results rather complicated if not even impossible within reasonable time. Its execution not only on standard desktop PCs but on a new, fast Linux[®]-based 4-processor (Opteron) computer at the University Paderborn with 16GB RAM allows efficient simulations of many different structures.

The commercially available and only recently developed FDTD code CrystalWave was used to simulate transmission through PhC structures with and without tapers (distorted hexagonal lattices and ARL, see 5.4.1 and 5.4.2). While it offers a convenient graphical user interface its main disadvantage lies in the fact, that it was only available as a 32bit Windows[®]-based program. This limits the amount of addressable memory to < 2GB leading to problems when calculating transmission for frequencies having a low v_g . While CrystalWave's algorithm can in principle handle 3D structures, its practical use is miniscule since 2GB are not enough to sufficiently represent the structures and perform numerical simulations, especially not when it comes to high aspect ratio structures. Furthermore, it is not possible to (numerically) access, store or postprocess data like field distributions, etc. The photonic structures can be specified using the graphical user interface or by scripts. The evaluation of the simulation results has unfortunately to be done man-

	PWE	FDTD	FEM
available software	MPB	CrystalWave	FEMLAB / HelmPole
operating system	Linux [®]	Windows [®]	Linux [®]
available hardware	Pentium 4, 2GB RAM (MPI MSP Halle) 4 x Opteron, 16GB RAM (Univ. Paderborn)	Pentium 4, 2GB RAM (MPI MSP Halle)	Pentium 4, 2GB RAM (MPI MSP Halle) 4 x Opteron, 16GB RAM (Univ. Paderborn)
structure size	infinite [†]	finite	finite
structure representation	plane wave expansion [‡]	space/time grid	space grid
solution type	stationary	temporal evolution	stationary
computational speed	fast	slow	medium
structure generation	script	script	script
result evaluation	script	manual	script
PhBS*	+	- *	+
Transmission	-	+	+
Availability	MPI MSP & Univ.Pb	MPI MSP & Univ.Pb	Univ.Pb

Table 5.1: Overview of different numerical methods for PhC calculations used in this work. ([†] finite structures by employing supercells. [‡] MPB uses a modified approach, see 4.1.2.1. * in principle the PhBS can be calculated using FDTD, but the necessary software package was not available. * group velocity can be derived using $\vec{v}_g = \frac{\partial \omega}{\partial \vec{k}}$)

ually. Absorption calculations are not possible because it is not possible to use complex dielectric constants. To avoid artefacts from unwanted reflections at the boundary of the computational domain perfectly matched layer (PML) boundary conditions are applied. The choice of the PML parameters however is a subject to itself.

HelmPole and FEMLAB (together with FEMLAB's electrodynamics package) are both FEM-based programs running under Linux[®] on a fast multiprocessor (4 x Opteron) computer with 16GB RAM at the university Paderborn. Only this powerful computer allows reliable simulations of transmission through large PhCs with and without taper concepts (distorted hexagonal lattice and ARL in this work, see 5.4.1 and 5.4.2). In addition, FEMLAB offers full access to all computed quantities (field distributions, transmission, ...) and offers a nice graphical user interface. PML boundary conditions are also used in this scheme. Furthermore, FEMLAB offers the possibility to simulate semi-infinite PhCs, i.e., PhCs being finite along the propagation direction and infinite along the perpendicular direction, by using periodic boundary conditions. Simulations as well as the analysis of the results can be controlled by scripts, making it rather fast and convenient. In addition, complex dielectric constants can be used. This allows estimation of the expected absorption enhancement. PhBS can also be calculated, but the necessary effort is quite high. This is the reason why MPB was used for this purpose throughout this work.

The above discussion might bring up the impression that FEM schemes are superior to FDTD approaches. But FDTD is the only of the used numerical methods that allows observation of the temporal development of electromagnetic fields. Furthermore, to avoid misinterpretation of results due to numerical artefacts it is important to verify them using different numerical schemes, e.g., FEM and FDTD.

5.2 Basic requirements for a PhC gas sensor

5.2.1 Working principle

The working principle underlying a PhC-based spectroscopic gas sensor is the enhancement of the interaction amongst radiation and gas molecules, as already described in section 1.3.1. This enhancement can be achieved by prolonging the interaction time $t_{\text{int}} = l_{\text{int}}/v_{\text{g}}$ between radiation and gas, given by the fraction of interaction length l_{int} and the group velocity v_{g} . In a PhC this can be obtained by utilizing the possibility of achieving very low v_{g} for certain frequencies ω in the PhBS. The slope of a band in the PhBS corresponds to the group velocity of light v_{g} :

$$\vec{v}_{\text{g}} = \frac{\partial \omega_{\text{norm}}}{\partial \vec{k}} \quad (5.1)$$

with ω_{norm} being the normalized frequency and \vec{k} the wavevector. From this it follows that wherever photonic bands are flat, the group velocity of light is small. The lowest so far experimentally reported group velocities are on the order of a few tenths of percent of the speed of light in vacuum c_0 [57][58][31].

The interaction of radiation and gas molecules can be described by the Lambert-Beer law of absorption (3.1): $I(l_{\text{int}}) = I_0 e^{-\alpha(\tilde{\nu})cl_{\text{int}}}$. It states that the intensity $I(l_{\text{int}})$ after interaction of light and gas along an interaction path of length l_{int} is given by the transmitted intensity I_0 measured without gas being present times an exponential decay determined by the absorption constant $\alpha(\tilde{\nu})$ of the gas, the concentration of the gas c and l_{int} . In a PhC, the effective interaction length $l_{\text{int,eff}}$ to achieve the same absolute absorption should be smaller by the enhanced absorption that can be achieved due to the low v_{g} and therefore would be expected to be only a few percent of the conventional interaction length l_{int} .

But additionally it has to be taken into account that the distribution of the electric field - which mediates the interaction of light and gas - is different for a plane wave as it exists within a conventional interaction volume compared to a Bloch mode in a PhC. Because some of the energy of the incoming plane wave will be stored in the dielectric host material of the PhC and the interaction of light and gas takes place in the pores of the PhC structure, the overall expected enhancement will be smaller compared to what is expected from the v_{g} argument alone.

From the working principle of a PhC-based spectroscopic gas sensor described above, it follows that the following requirements have to be met by the band structure of the PhC:

1. **Resonance condition:** A part of a band having small slope has to spectrally overlap with the absorption frequency of the gas.
2. **Interaction condition:** The portion of the electric field of the mode located within the pores of the PhC has to be as large as possible.
3. **Symmetry condition:** The symmetry of the band has to allow coupling to impinging and outgoing plane waves.

Gas	Formula	Absorption wavenumber (cm ⁻¹)	Absorption wavelength (μm)
Ethanol	C ₂ H ₅ OH	2940	3.4
		1060	9.55
Sulfur-hexafluoride	SF ₆	948	10.55
Carbon monoxide	CO	2200	4.5
Carbon dioxide	CO ₂	2350	4.2
Methane	CH ₄	3000	3.4
		1300	7.7
Nitrogen monoxide	NO	1820	5.5
Nitrogen dioxide	NO ₂	2250	4.4

Table 5.2: Prominent absorption lines for common gases in the NIR/MIR.

5.3 Design of the photonic band structure

5.3.1 Spectral range

The spectral region typically used for spectroscopic gas detection is the infrared. This is because the gases of interest show characteristic fingerprints in the NIR/MIR wavelength range from about 1.5 μm- 30 μm, arising from rotational-vibrational excitations of the gas molecules. As a consequence, a PhC for the IR spectral region has to be designed. This can be achieved using the macroporous silicon material system. The fabrication technique described in section 4.2.1 allows the realization of PhCs consisting of air macropores in a Si matrix. The lattice constant of such a PhC can be chosen between 500 nm up to about 20 μm [49]. While the choice of the lattice constant allows a crude selection of the wavelength range of the PhC, fine tuning of the band structure can be achieved by changing the diameter $d_{\text{pore}} = 2r$ of the pores during fabrication using the PECE process described in 4.2.1, r being the radius of the pores.

In the following we will focus on the spectral region between 3 μm - 11 μm where prominent absorption lines of typical gases as shown in tab.5.2 exist. A PhC to be used for SF₆ detection will be designed. Due to the scale invariance of the master equation (4.9) these results can be used to design a PhC for the detection of other gases such as, e.g., ethanol or methane, by simply applying equations (4.11) – (4.13).

r/a = 0.25 - 0.45	ΓM		ΓK	
	air band	norm. freq.	air band	norm. freq.
1st TE PhBG	B03	0.239 - 0.494	B02	0.256 - 0.521
1st TM PhBG	B02	0.298 - 0.199	B03	0.253 - 0.445
2nd TM PhBG	B04	0.346 - 0.500	-	-

Table 5.3: Fine tuning of the spectral position (in normalized frequencies $(\omega a)/(2\pi c)$) of the upper band edge of the PhBG for a hexagonal lattice of air pores in Si as well as the number of the band. The lower (upper) spectral position of the air band corresponds to $r/a = 0.25$ ($r/a = 0.45$). (Bands that do not couple to incoming plane waves, see 5.3.3, are already accounted for.)

5.3.2 Resonance and interaction condition

Flat bands in a PhBS are, e.g., found at the edges of the PhBG. In addition, the upper band edge of the first PhBG is usually called the *air band*. This is due to the fact, that for this band most of the electric field energy is located in regions of the PhC having the lower refractive index [5] ($n_{\text{air}} \approx 1 < 3.4 = n_{\text{Si}}$). From this argument follows that the above mentioned interaction condition is very likely to be fulfilled by the upper edge of the PhBS. This is verified in the next section (5.3.3) using the 2nd TE band and the 3rd TM band along ΓK whose electric field components are shown in fig.5.1.

Furthermore, the band edges are *spectrally* rather *isolated*, i.e., below (above) the air (dielectric) band there is no other band. This has the advantage that light with a specific frequency impinging onto the PhC does not have the possibility to couple to various other modes with the same frequency as the desired mode. This would lead to a decrease of the amount of energy coupled to the desired gas sensing mode.

Calculations of the band structure of hexagonal and square lattice 2D PhCs based on the macroporous Si material system show, that the spectral position of the first band gap occurs at wavelengths $\lambda \approx 2a$ with a being the used lattice constant. Based on these arguments and the availability and experience in fabrication of hexagonally arranged macropore arrays in n-Si by PECE, a lattice constant of $a = 4.2 \mu\text{m}$ is chosen for the realization of the PhC. Other lattice geometries such as square lattice or hexagonal lattices with 1 and 3 atom bases (i.e., additional pores) have also been considered. But none of them showed distinct advantages compared to the hexagonal PhC lattice. In contrast, introduction of basis atoms into the hexagonal lattice leads to a more complex PhBS. Especially the field distributions of the Bloch modes are becoming very different from plane waves, thereby aggravating coupling to and from the PhC structure. For the ARL concept's functionality an appropriate PhC termination is necessary to allow coupling to the involved surface states. While this PhC termination is already existing along the ΓM direction in the hexagonal lattice, in the case of the square lattice the appropriate surface termination would have to be realized by either shifting the position or by changing the diameter of every second pore in the outermost pore row [59][60]. The latter is not possible in the macroporous Si material system and the first would be similar to the PhC termination using a hexagonal lattice.

To enable a high number of gas molecules being present within the PhC pores, d_{pore} should be as large as possible. This means the porosity of the structure, see equation (4.32), should be as high as possible. Stable macropore growth within Lehmann's model and the experimental setup used in this work is possible up to values of $r/a \approx 0.42$. Larger pore diameters can be obtained by repeated thermal oxidation of the PECE Si and a subsequent HF-Dip. But it has to be taken into account, that higher porosities lead to less mechanical stability, a property worsening the handling of such a sample in the lab and not desired for a PhC to be used in a robust gas sensor. Therefore an upper limit of 0.45 for the r/a ratio is chosen. The minimum r/a ratio for PEC growth of hexagonally ordered macropores is on the order of 0.25. The spectral position of the upper band edge can be fine tuned as shown in tab.5.3.

For a lattice constant of the PhC of $a = 4.2 \mu\text{m}$ the SF_6 absorption wavelength of $10.55 \mu\text{m}$ corresponds to a normalized frequency of $\omega_{\text{norm},\text{SF}_6} = 0.398$. From tab.5.3 it can be seen, that a spectral overlap of the upper band edge of the PhBG with $\omega_{\text{norm},\text{SF}_6}$ can be achieved by choosing the appropriate, practically realizable, r/a ratio (except for the first TM PhBG along ΓK direc-

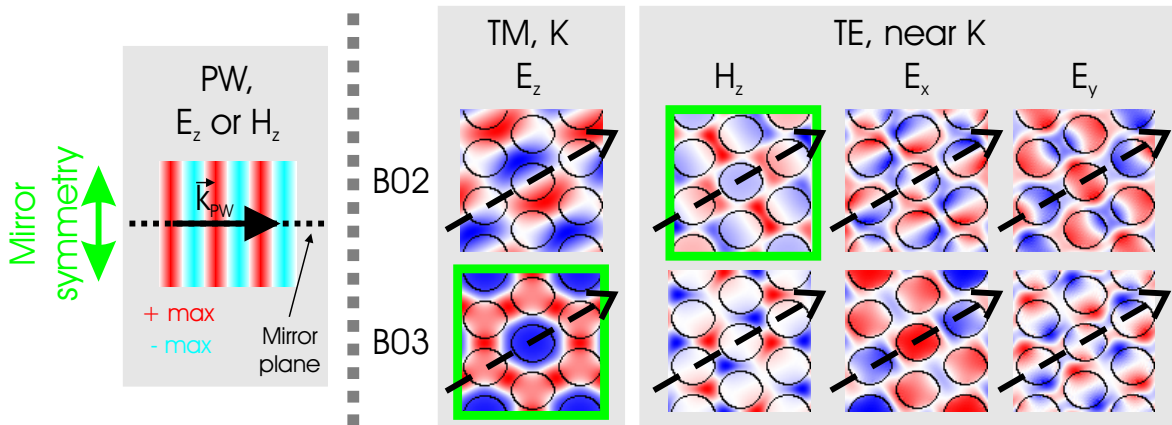


Figure 5.1: Coupling condition for plane waves (PW) and PhC Bloch modes. The mirror symmetry of the H_z (E_z) components of the impinging TE (TM) modes has to be fulfilled by the PhC mode under consideration along the direction of incidence (ΓK in the picture, represented by the black dashed arrow). The 3rd TM mode and the 2nd TE mode fulfill this symmetry condition (marked by the green frame), while the 2nd TM and the 3rd TE mode are anti-symmetric.

tion).

Minor deviations of the spectral position of the air band under consideration, e.g., caused by imperfect PhC structures, are tolerable, because the width of absorption lines of gases in the NIR/MIR wavelength range are on the order of a few hundred nm, corresponding to a spread in normalized frequencies of $\pm 1\%$.

5.3.3 Coupling condition

Besides the necessary spectral overlap of a flat photonic band and the gas absorption line, the symmetry of the PhC Bloch mode under consideration has to allow coupling of incoming plane waves and will be investigated in this section.

The naturally given directions in a hexagonal 2D PhC are the high symmetry directions ΓK and ΓM . Incoming plane waves with TE (TM) polarization have mirror symmetry of the z -component of their magnetic (electric) field with respect to a plane defined by their \vec{k} -vector and the pore axis. A PhC mode to which these incoming plane waves should couple, has to fulfill the same symmetry requirement. The situation is depicted in fig.5.1. The mirror symmetry of the PhC mode along ΓK direction is only fulfilled for the 3rd TM and the 2nd TE band. The 2nd TM and the 3rd TE band cannot couple to a plane wave because the corresponding PhC mode is anti-symmetric under such a mirror inversion.

Furthermore, from the field distribution of the E_x and E_y components of the 2nd TE band, it follows that a considerable fraction of the electric energy is located within the pores, as required by the above stated interaction condition. Calculation of the time-averaged electric field energy density ($D_{pwr} = \epsilon_{air} |\vec{E}|^2$) yields that for the 2nd TE band along ΓK and $r/a = 0.385$ a fraction of about 41% of the electric energy in the whole unit cell is located within the air pore (MPB).

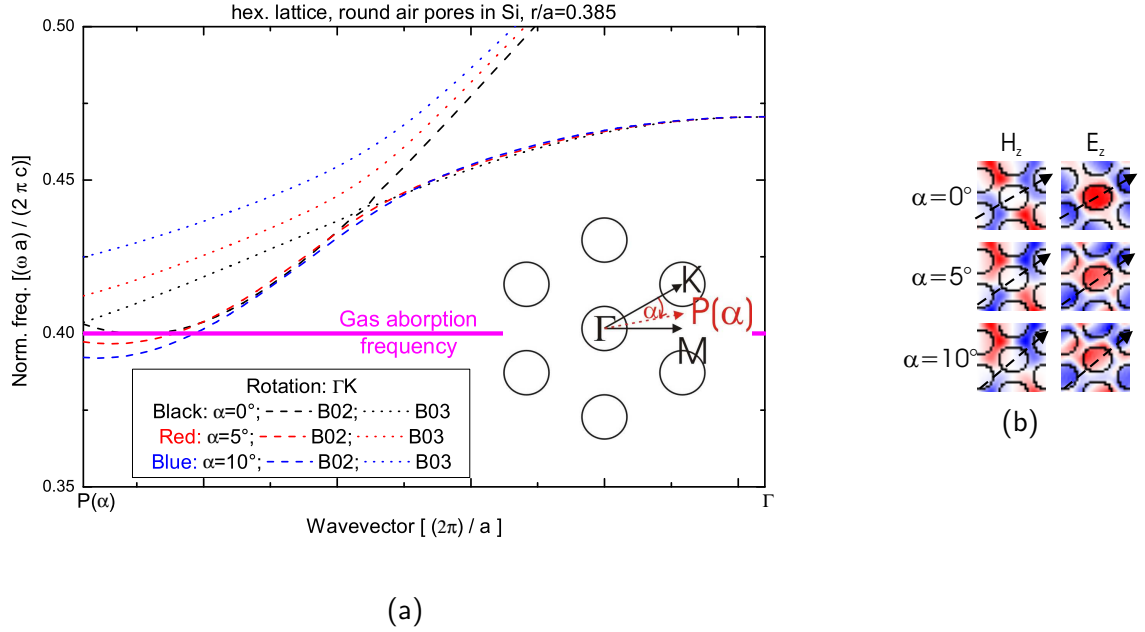


Figure 5.2: Fine tuning of the PhBS by rotation of the PhC around an axis along the pores. **a)** Spectral shift of the PhBS. Note that the degeneracy of the 2nd and 3rd TE bands along the ΓK direction is lifted under rotation. **b)** Change of the field distributions.

5.3.4 PhC interaction volume design: tuning and robustness

From an application point of view two further issues concerning the design of the PhC interaction volume have to be addressed: tuning to compensate, e.g., for fabrication tolerances and robustness, i.e., stability under operating conditions.

5.3.4.1 Tuning of PhC gas sensors

Although the macroporous Si fabrication process can be reasonably well controlled, minor deviations from the designed r/a ratio can occur. In a worst case scenario a too large r/a ratio would lead to a loss of spectral overlap of the gas absorption frequency ω_{abs} and the flat photonic band intended to be used for gas detection (TEB02K). This can in part be compensated by rotating the PhC structure around an axis parallel to the pores as shown in fig.5.2. Such a rotation on the order of a few degrees leads to a spectral red-shift of the PhBS on the order of 1%. The allocation of the magnetic and electric fields within the PhC changes, too, but they keep their characteristic symmetry and intensity distributions. As a result the spectrally red-shifted mode can still be used for gas detection. However, from fig.5.2a it is also obvious, that the slope of the band increases by a factor of 5 and 10 for rotation of 5° and 10° , respectively. As a consequence the enhancement due to low v_g is reduced. While this is explicitly demonstrated for the TEB02K flat band in fig.5.2a, this tuning can be used for all the potential gas sensing points given in tab.5.4.

5.3.4.2 Robustness of PhC gas sensors

To avoid condensation of, e.g., water on the pore walls the PhC gas sensor has to be heated to about 60°C during operation. This leads to a change Δn_{Si} of the refractive index of the Si matrix material as well as a change in the atomic lattice constant of the Si a_{Si} .

The second effect is negligible in the temperature range of interest due to the very small thermal expansion coefficient of Si $\Delta a_{\text{Si}}(T) \approx 2 \times 10^{-6} \text{ K}^{-1}$. Even a temperature change of $\approx 3000 \text{ K}$ would lead to a red-shift of the bands under consideration on the order of 0.1% as derived from PhBS calculations¹. The change in refractive index due to temperature changes is larger. With the thermo-optical coefficient of Si $\Delta n_{\text{Si}}(T) \approx 2 \times 10^{-4} \text{ K}^{-1}$ the refractive index of Si in the IR $n_{\text{Si}} = 3.4$ changes by about 12% for a temperature change of 100 K. This leads to a shift of the PhBS on the order of 1%. This number has to be taken into account when designing a PhC interaction volume for operation at elevated temperatures.

When discussing the versatility of the PhC-based spectroscopic gas sensor concept the chemical stability of the macroporous Si membrane against aggressive/corrosive gases has to be investigated. One possibility to achieve this is to coat the pore walls. Depending on its thickness d_{coat} and its refractive index n_{coat} the coating will influence the PhBS and therefore the functionality of the sensor. SiN could be used as such a coating material. It is chemically inert and would in addition increase the mechanical stability of the membrane structure. The refractive index of SiN, e.g., deposited by low pressure chemical vapor deposition (*LP-CVD*) depends on the SiN composition. A typical value is $n_{\text{SiN}} \approx 2$. With this and typical thicknesses of SiN coatings on the order of 20 nm the shift in PhBS can be calculated to be on the order of about 1%. For the design of a PhC interaction volume to be used in a PhC-based spectroscopic gas sensor device this has to be taken into account.

In summary it is found that external parameters like operating temperature, angle of incidence and eventually applied coatings do have an influence on the PhBS of the interaction volume PhC. However, knowledge of these effects as well as the final operating conditions do allow compensation.

5.3.5 PhC interaction volume design: results

For the design of a PhC interaction volume to be used for detection of SF₆ at an absorption wavelength of 10.55 μm the following conclusions can be drawn:

- a 2D PhC made of hexagonally arranged macropores in Si with a lattice constant of $a = 4.2 \mu\text{m}$ will be used
- In principle four PhC bands fulfill the necessary prerequisites. They are summarized in tab.5.4 below:

¹The melting point of Si is far below this temperature at about 1450°C

Acronym for future reference	\vec{k} -direction	Polarization	Band	\vec{k} -point	r/a ratio	D_{pwr} in pores (%)
TEB03M	ΓM	TE	3	M	0.33	11
TMB04M	ΓM	TM	4	M	0.34	9
TEB02K	ΓK	TE	2	$\approx 0.92 \vec{\Gamma\text{K}}$	0.385	41
TMB03K	ΓK	TM	3	K	0.43	21

Table 5.4: Overview of PhC modes fulfilling the necessary prerequisites to be used for gas sensing. The last column gives fraction of the time-averaged electric field energy density ($D_{\text{pwr}} = \epsilon_{\text{air}} |\vec{E}|^2$) located within the pore.

The investigations below concerning the effective connection of the PhC interaction volume to the outside world will exemplarily be performed concentrating on TEB02K and TMB03K. This is done for clarity of presentation and because the energy within the pores is highest for these two bands. The results derived can in principle be transferred to the other bands (TEB03M, TMB04M) of interest.

5.4 Transmission through a PhC gas sensor

After having designed the PhC interaction volume for the intended gas sensor, the connection to the outside world, i.e., incoming and outgoing radiation, has to be investigated. To achieve high sensitivity of the sensor as well as a good signal-to-noise ratio, as much of the incoming/outgoing light as possible should be coupled to/from the PhC gas sensing mode.

While coupling issues from ridge waveguides and optical fibers to PhC waveguides have been extensively studied due to their potential for application in optical circuits [61][62][63], coupling of light to bulk PhC modes was only addressed occasionally in literature [64]. Unfortunately, the strategies based on changing the local porosity used in those publications cannot be applied to the macroporous Si material system due to its very different etching process compared to dry etching techniques like RIE or ICP used in those publications.²

In the following sections, two coupling strategies of light to bulk PhCs realizable with the macroporous Si material system will be discussed, of which the first one is based on a semi-classical adiabatic taper approach and the second one is a new concept developed in this work, entitled *Anti-Reflection-Layer* (ARL).

5.4.1 Semi-classical approach: adiabatic taper

Since the intended PhC-based gas sensor is supposed to operate in transmission, efficient coupling of the light between the surrounding air and the PhC has to be achieved. When coupling light across dielectric interfaces the three main issues to be addressed are phase matching, mode matching and impedance matching. The reflection coefficient is sensitive to the phases of the fields in the two dielectrics. While in air the phase fronts of incoming/outgoing plane waves

²Macroporous Si remains the material system of choice for the realization of a PhC interaction volume for a spectroscopic gas sensor, though, because with RIE/ICP the necessary aspect ratios $\gg 100$ cannot be achieved.

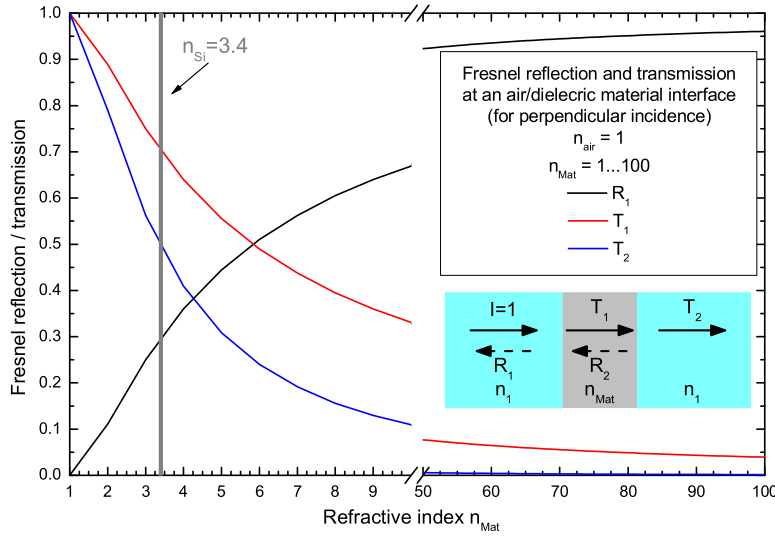


Figure 5.3: Fresnel reflection at an air/dielectric interface and transmission through a dielectric slab for perpendicular incidence as a function of the refractive index n_{mat} .

are planes, their shape might be rather complicated in PhCs where Bloch modes exist. Mode matching concerns the overlap of the fields of the incoming and outgoing waves in the interfacial plane. The worst case of mode mismatch is illustrated by the existence of non-coupling bands, as discussed in 5.3.3. The coupling coefficient

$$\eta \propto \frac{\int_{A_{\text{int}}} dA \vec{E}_{\text{air}}(\vec{r}) \vec{E}_{n,k}^*(\vec{r})}{\int_{A_{\text{int}}} dA \vec{E}_{\text{air}}(\vec{r}) \vec{E}_{\text{air}}^*(\vec{r}) \int_{A_{\text{int}}} dA \vec{E}_{n,k}(\vec{r}) \vec{E}_{n,k}^*(\vec{r})} \quad (5.2)$$

is proportional to the overlap of the electromagnetic fields $\vec{E}_{\text{air}}(\vec{r})$ in air and $\vec{E}_{n,k}(\vec{r})$ in the PhC at the interface with area A_{int} . Due to the different nature of plane waves as they exist in air and Bloch modes within the PhC, it is not possible to increase the coupling efficiency by manipulating the above quantities. But one possibility to improve the coupling of radiation energy between air and a PhC mode might consist in matching of the impedance. The impedance mismatch between air and a dielectric medium is given by $1/n_{\text{mat}}$ with n_{mat} the refractive index of the dielectric. In a PhC n_{mat} is given by the inverse of the slope of the photonic band under consideration for a certain frequency. The working principle of the intended PhC gas sensor is based on utilization of low group velocity v_g . From classical optics it is known that the dispersion in homogenous media with a refractive index of n_{mat} is given by $\omega = c_0 |\vec{k}| / n_{\text{mat}}$. From this the group velocity $|\vec{v}_g| = |\partial\omega / \partial\vec{k}| = c_0 / n_{\text{mat}}$ can be derived. At an interface of two dielectrics, e.g., air and glass, the amount R of light being reflected at this interface is described by Fresnel's equations. For perpendicular incidence relative to the surface, i.e., $\alpha=0^\circ$, they can be written as

$$R(\alpha = 0^\circ) = \left| \frac{n_{\text{air}} - n_{\text{mat}}}{n_{\text{air}} + n_{\text{mat}}} \right|^2. \quad (5.3)$$

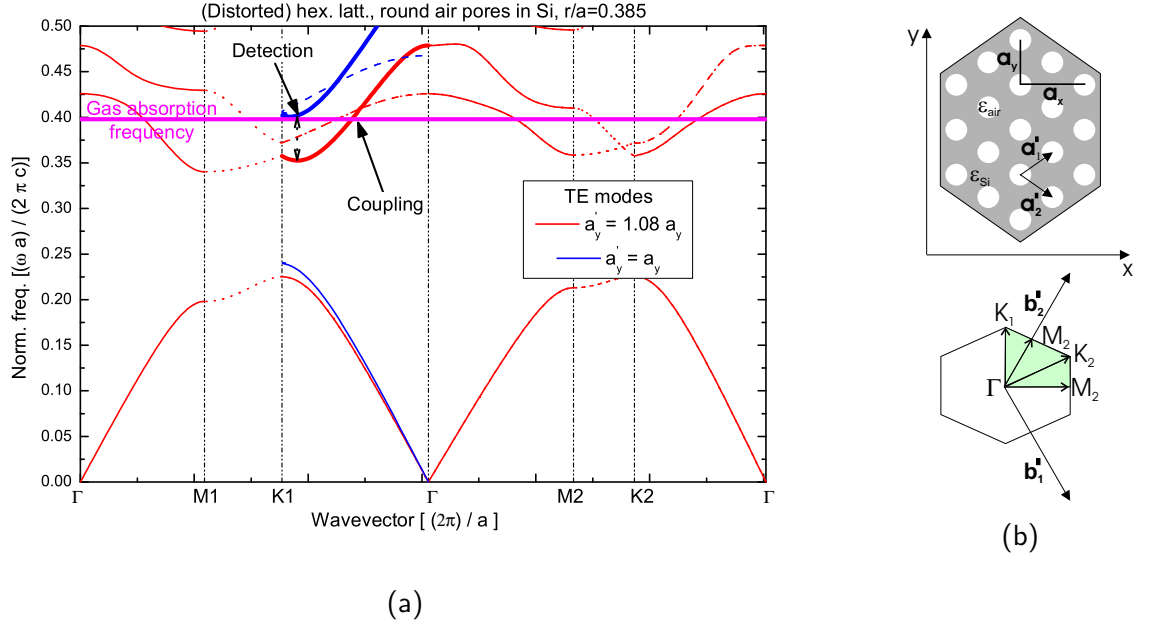


Figure 5.4: Concept of an adiabatic taper for a bulk PhC. **a)** The idea is to couple to a steep part of the mode intended to be used for gas detection (TEB02K) and then transfer the energy adiabatically to the flat portion of the band. (Only the solid lines couple to plane waves, compare 5.3.3). Red: PhBS of the distorted hex. lattice. Blue: PhBS of an undistorted hex. lattice along ΓK projected onto the ΓK_1 path of the distorted hex. lattice. **b)** To achieve spectral overlap of the steep part and the flat part, the mode has to be shifted on the frequency scale. This is achieved by distorting the PhC lattice along ΓK . The real space and the reciprocal space lattices of such a PhC are shown, \vec{a}'_1 , \vec{a}'_2 and \vec{b}'_1 , \vec{b}'_2 being the respective basis vectors (for details see A.1.2). The area highlighted in green represents the irreducible Brillouin zone.

Based on equation (5.3) fig.5.3 shows the reflection and transmission through a dielectric slab in air. The transmission decreases drastically with increasing refractive index of the dielectric. For a glass plate with $n_{\text{mat}} = 1.5$ the total transmission is about 92% while for a bulk Si slab with $n_{\text{mat}} = n_{\text{Si}} = 3.4$ the total transmission is only on the order 50% of the incoming light.

For the flat band intended for use in the gas detection scheme with a low group velocity $v_g \ll c_0/100$ and a corresponding, high effective refractive index $n_{\text{eff}} \gg 100$, the expected transmission through the PhC structure at the gas absorption frequency would be negligible, resulting in a non-functional device.

The first approach to overcome this challenge is based on the following idea: as the reflection is relatively low for interfaces with small difference in refractive index $\Delta n = n_1 - n_2$, impinging light should first be coupled to a relatively steep part of the gas sensing band where n_{eff} is relatively small. Once the energy is in the band it could be transferred into the intended gas sensing mode by adiabatically shifting the PhBS. This principle is shown in fig.5.4a where the point labelled *Detection* is the one to be used for gas detection, while the point labelled *Coupling* should be used for the efficient coupling of an impinging plane wave.

The shift of the PhBS is achieved by an appropriate distortion of the originally hexagonal PhC lattice, shown in fig.5.4b. As a consequence of the distortion the symmetry of the real and the

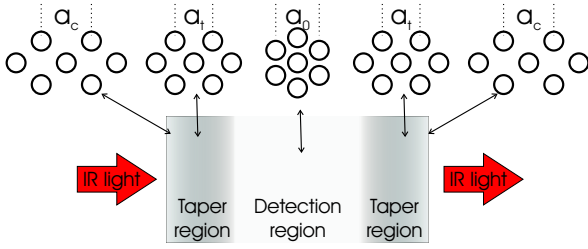


Figure 5.5: Scheme of a PhC gas sensor device incorporating an adiabatic taper. The lattice constant along the direction of distortion a_t is smoothly changed in the taper region from the value for optimum coupling a_c to the value a_0 optimal for gas sensing.

reciprocal space lattices are reduced. Their point groups change from $C_{6\nu}$ to $C_{2\nu}$. The originally 3 high symmetry points $\vec{\Gamma}$, \vec{M} and \vec{K} of the undistorted lattice are replaced by the 5 new high symmetry points $\vec{\Gamma}$, \vec{K}_1 , \vec{M}_1 , \vec{K}_2 and \vec{M}_2 . Furthermore it has to be taken into account that the length of the paths along the high symmetry directions is different in the undistorted and the distorted lattices. So for the purpose of comparing the PhBS an appropriate projection has to be made (similar to the projection of the PhBS of a 2D hexagonal PhC onto the PhBS of a, e.g., W1 waveguide when discussing guiding by a PhC waveguide [65]). The adiabatic transfer of the energy should be accomplished by smoothly changing the lattice constant of the PhC from the optimum lattice constant for coupling to the lattice constant for sensing, as shown in fig.5.5. In the coupling region, the lattice constant a_c along the direction of distortion is chosen to allow the lowest possible v_g . In the taper region the lattice constant a_t is then smoothly changed to the value optimal for gas detection, a_0 .

To find the optimal a_c the group velocity as a function of distortion was calculated (using MPB). It was found that for the 2nd TE band along the ΓK_1 direction a distortion of about 8% yields the steepest slope corresponding to $v_g \approx c_0/3$ for this band at the absorption wavelength of SF_6 , i.e., the distance of the pores should be $1.08a_0$ along the ΓK_1 direction while it remains a_0 along the ΓM direction.

The realization of such PhCs made of macroporous Si with a distorted hexagonal lattice, which (to the knowledge of the author) was never published before, will be discussed in section 6.

The above described coupling approach using an adiabatic PhC taper was so far based on arguments from classical optics, namely adiabatic matching of refractive indices at interfaces, in connection with the interpretation of the slope of a PhC band as the inverse effective refractive index for that mode. The results derived from appropriate calculations of the PhBS using a plane wave expansion method (MPB) seem to be promising to allow high increased transmission through these structures. However, as explained in section 4.1, this computational method does not yield transmission through PhC structures. Transmission was now calculated using FDTD as well as FEM software. Numerous FDTD calculations were performed in which both, the smoothness, i.e., the rate of adaption from a_c to a_0 , as well as the type of transition, i.e., a linear, exponential, quadratic and square-root-like change in lattice constant along ΓK_1 , were investigated. As a surprise it was found that the better the taper, i.e., the smoother the transition from the coupling lattice constant a_c to the detection lattice constant a_0 was chosen, the worse was the transmission.

The reason is that not only the different refractive indices n_{air} in air and n_{eff} in the PhC have to be matched. Much more important is an appropriate adjustment of the very different field distributions - a plane wave in air vs. a Bloch mode in the PhC. This is shown in fig.5.6, where

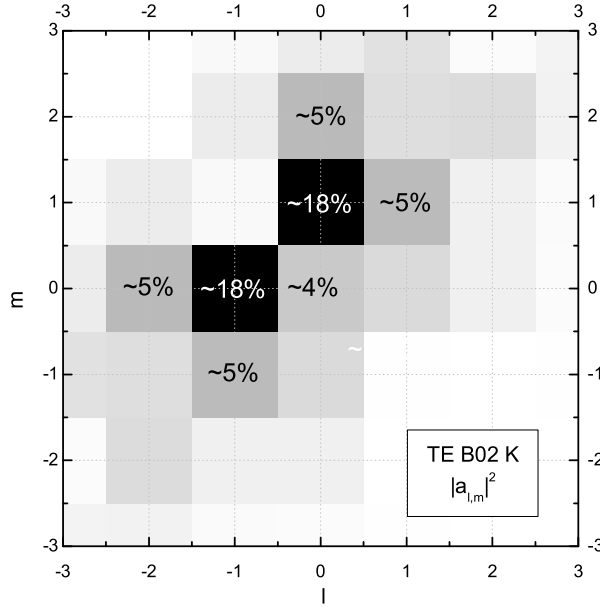


Figure 5.6: Lowest plane wave components of the TE B02K mode. Higher orders strongly contribute to the H_z field distribution, aggravating coupling to a plane wave. (numerical support by A.v. Rhein, Univ. Paderborn)

the contributions of different plane waves to the TE B02K Bloch mode are depicted. The H field for a TE polarized mode in a 2D PhC has the form of a Bloch mode and can therefore be written as

$$\vec{H}_{z,n,\vec{k}}(x, y) = e^{ik_y y} u_{n,\vec{k}}(x, y) \quad (5.4)$$

assuming $\vec{k} = (0, k_y, 0)$, i.e., considering wave propagation along $\Gamma K_1 \parallel y$. Due to its periodicity $u_{n,\vec{k}}(x, y)$ can be expanded into plane waves according to

$$u_{n,\vec{k}}(x, y) = \sum_{l,m} a_{l,m} e^{i(l\vec{b}_1 + m\vec{b}_2) \cdot (x,y)} \quad (5.5)$$

where the $a_{l,m}$ are the complex Fourier coefficients, \vec{b}_1, \vec{b}_2 the basis vectors of the reciprocal lattice, l, m integer numbers and x, y the real space coordinates. Applying a Fourier transformation to the field distribution of the H_z field of TE B02K (depicted in fig.5.1) the plane wave contributions $|a_{l,m}|^2$ were calculated and are plotted in fig.5.6. The zeroth order, i.e., the plane wave component $(l, m) = (0, 0)$ contributes only weakly to the field distribution, while higher order components dominate, thus aggravating coupling to incoming plane waves.

5.4.1.1 Adiabatic PhC taper: conclusions

The above results point out two major facts:

First, physical intuition together with proven approaches from classical optics have to be carefully reconsidered when applying them to PhCs. Simple matching of the (effective) refractive indices by distorting the lattice adiabatically, does not lead to the expected enhancement in transmission. Second, for the realization of a PhC-based gas sensing device utilizing low group velocity, a new method to increase coupling of plane waves to PhC modes has to be found and later implemented. This is discussed in the next section.

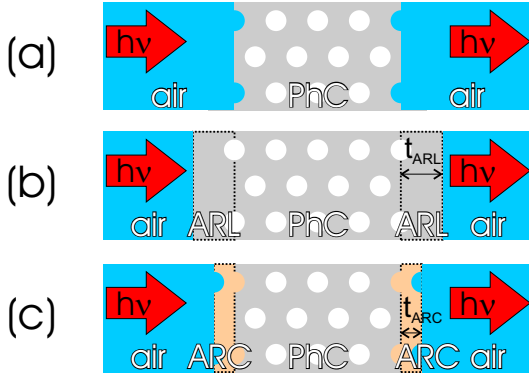


Figure 5.7: Anti-Reflection-Layer (ARL) scheme developed for efficient coupling of light impinging from air to a PhC Bloch mode. **a)** Typical air/PhC interface: corrugated surface. **b)** Interfaces using the ARL approach. Between air and the final PhC pore rows a layer with thickness t_{ARL} consisting of the PhC matrix material is introduced. **c)** Situation using a conventional Anti-Reflection-Coating (ARC): a layer of an appropriate material with refractive index n_{ARC} and thickness t_{ARC} is deposited on the typical PhC interface shown in a).

5.4.2 Novel concept: Anti-Reflection-Layer (ARL)

Since the simple transfer of knowledge from wave optics to PhCs does not result in the envisioned enhanced transmission, a new method had to be found. The solution developed in this work - termed Anti-Reflection-Layer (ARL) - is schematically shown in fig.5.7.

Typically the air/PhC interface has a corrugated surface as depicted in fig.5.7a, resulting from cleaving the PhC sample which breaks along a direction of high porosity, i.e., usually through the centers of pores along a high symmetry direction.

In the ARL scheme proposed, the air/PhC interface is modified by introducing a layer of thickness t_{ARL} of the PhC matrix material between the outermost PhC pore row and air. This minor modification of the interface has drastic consequences on the coupling - and hence the transmission through the PhC, even at frequencies, where the PhC bands are flat. Detailed results and an explaining hypothesis concerning the ARL concept are given further below.

At this point it has to be mentioned that this ARL concept is different from the well known Anti-Reflection-Coating (ARC) extensively used in classical optics to minimize reflection at dielectric interfaces, e.g., eyeglasses, depicted in fig.5.7c. The optimal ARC has a thickness of

$$t_{ARC} = \lambda / (4n_{ARC}) \quad (5.6)$$

and is ideally made of a material with refractive index

$$n_{ARC} = \sqrt{n_1 n_3} \quad (5.7)$$

n_1 and n_3 being the refractive indices of the dielectric materials constituting the uncoated interface. In the case of a flat band in a PhC with effective refractive index $n_{eff} \rightarrow \infty$ this concept would be impossible to implement. Furthermore, practical realization of such a coating would be challenging because the surface to which it should be applied is not plane but corrugated. Interpreting the scheme depicted in fig.5.7b in terms of a classical ARC with $n_{ARC} = n_{Si} = 3.4$ would yield an optimal ARC thickness of $t_{ARC} = 776$ nm using equation (5.6) for a wavelength $\lambda = 10.55$ μm (SF_6 absorption line).

By numerical simulations using FDTD as well as FEM codes it is found, that the transmission through a PhC strongly depends on its surface termination. Fig.5.8a shows the transmission

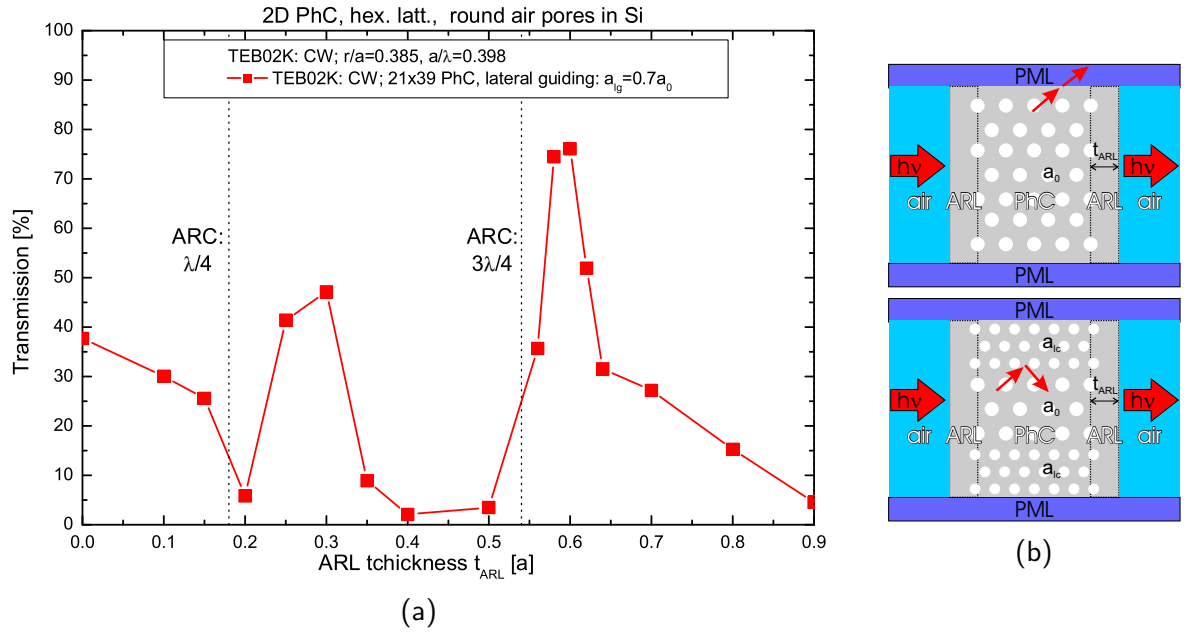


Figure 5.8: a) Transmission T through a PhC as a function of the thickness of the ARL (in units of the lattice constant a_0) for the TEB02K mode. The vertical dotted lines mark the optimum thickness of a classical ARC made of Si-based on (5.6). **b)** Scheme for lateral confinement: by using a 2nd PhC with a PhBG spectrally overlapping with the frequency of TEB02K next to the interaction volume PhC. Light leaving the latter is back reflected.

through a hexagonal PhC for the TEB02K mode ($r/a = 0.385$). For the TEB02K mode the transmission increases up to about 76% from only about 38% with standard surface termination. Similar results are obtained for the TMB03K mode. The optimal thickness of the ARL t_{ARL} is found to be 0.57 - $0.6a_0$. This value is very different from the above derived optimal thickness of an ARC of 776 nm corresponding to $t_{\text{ARC}} = 0.18a_0$ for the lattice constant $a_0 = 4.2 \mu\text{m}$ considered here. This shows that the ARL concept is fundamentally different from the classical ARC approach.

In the FDTD calculations PML boundaries are used. At the interface between the PhC and the boundary of the calculation region parallel to the direction of transmission this leads to loss of light energy. To investigate the influence of this effect, lateral confinement (lc) was introduced by adding a PhC (lc -PhC) whose PhBG lies in the spectral region of the transmitted light on each side of the interaction volume PhC. Now, light reaching the boundary of the interaction volume PhC is not damped away by the PML, but reflected back into the interaction volume PhC by the lc -PhC as shown in fig.5.8b and fig.6.6. The parameter used to control the position of the PhBG - and thereby the backreflection - of the (also hexagonal) lc -PhC was the lattice constant a_{lc} . The other possible parameter, namely the ratio r_{lc}/a_{lc} , cannot be changed independently in the macroporous Si material system, because the porosity p (4.32) achieved by PECE will be the same in all regions of the sample. By choosing an appropriate lattice constant $a_{lc} = 0.7a_0$ for the lc -PhC the transmission can be increased further by about a factor of 2. This has to be taken into account when assessing the transmission calculations. The calculated transmission using FDTD is usually lower than the real one, see also section 4.1, but the results give at least a good impression of what is to be expected.

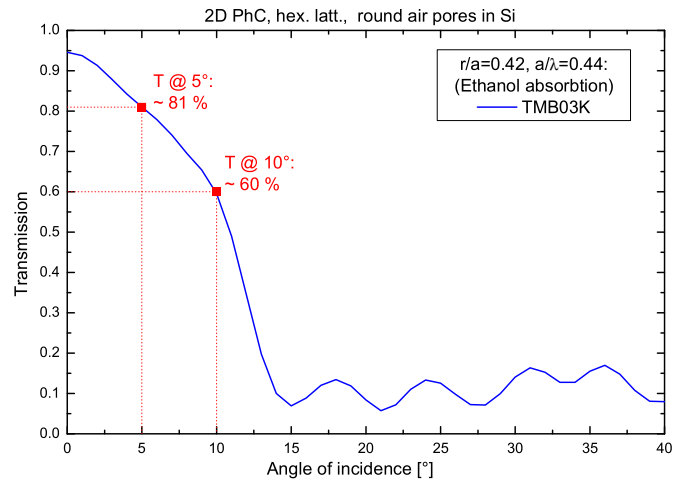


Figure 5.9: Robustness of the ARL concept under non-perpendicular incidence. Even for relatively high incidence angles α the transmission is still higher as compared to a corresponding PhC without ARL. (Calculations by A.v. Rhein, Univ. Paderborn.)

5.4.2.1 ARL concept: robustness

Non-perpendicular incidence As shown in section 5.3.4.1, fine tuning of the spectral overlap of the gas absorption line and the flat PhC mode can be achieved by rotation of the PhC around the pore axes. This corresponds to a non-perpendicular angle of incidence α with respect to the normal of the air/PhC interface. The ARL concept has also proven robust in this case, as shown in fig.5.9 where results from numerical simulations using an FEM code for the TMB03K mode tuned for the $9.46 \mu\text{m}$ ethanol absorption line are plotted. Even for relatively high incidence angles of $\alpha = 5^\circ$ and $\alpha = 10^\circ$ the transmission is with 81% and 60%, respectively, still higher as compared to a corresponding PhC without ARL ($\approx 40\%$).

Proximity effect As discussed later in section 6.4 practical realization of the ARL by conventional means, such as sawing or laser cutting of the porous structure after the PECE process, cannot be achieved with respect to precision and surface quality. Therefore an approach of fabricating the ARL during the PECE of the macropore array was developed and is described in 6.4.2. A characteristic of the PECE process has to be considered. The local porosity depends on the local concentration of electronic holes at the HF/Si interface. The electronic holes are homogeneously generated at the backside of the Si wafer and diffuse through the wafer and therefore a homogeneous hole concentration is achieved at least several μm before the HF/Si interface. This homogeneous distribution of electronic holes is then changed by the space charge region present at the HF/Si interface that focuses the electronic holes onto the pore tips. If the pores are arranged in a regular pattern, each pore will obtain an equal amount of electronic holes and hence adjacent pores have the same diameter. But if this regular pattern is disturbed, as it is the case in the ARL design, the situation changes.

The ARL is realized by PECE a trench next to the last row of pores of the interaction volume

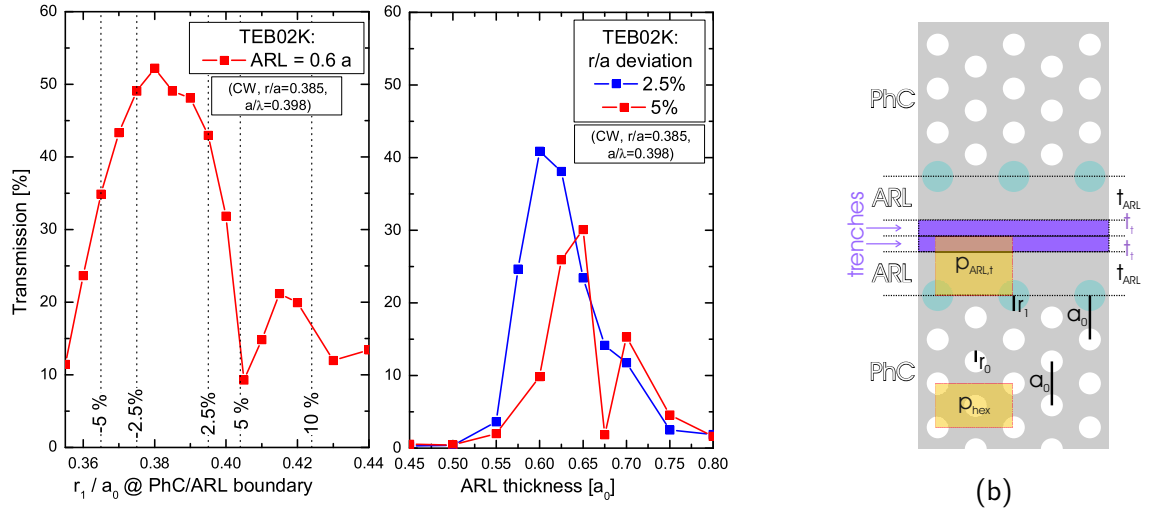


Figure 5.10: Robustness of the ARL concept: **a)** influence of deviations of the pore diameter from the desired diameter for fixed ARL width (left) and compensation of the PECE proximity effect by changing the ARL thickness (right). **b)** Geometrical situation at the PhC/ARL interface during PECE. The yellow regions represent the unit cells used for the calculation of the porosity in the transition region from bulk PhC and ARL.

PhC as depicted in fig.5.10b. While the porosity in the bulk PhC region p_{hex} is given by equation (4.32), the porosity in the ARL region is given by

$$p_{ARL,t} = \frac{\frac{1}{2}\pi r_0^2 + a_0^2\sqrt{3}t_t}{a_0^2\sqrt{3}(t_{ARL} + t_t)} \quad (5.8)$$

$$= p_{hex} \frac{1}{t_{ARL} + t_t} \left(\frac{1}{4} + \frac{t_t}{p_{hex}} \right) \quad (5.9)$$

with a_0 being the lattice constant of the bulk PhC, r_0 the radius of the pores in the bulk PhC, t_{ARL} and t_t the thickness of the ARL and the trench (in units of a_0), respectively. Equal porosity in both regions is achieved for $p_{hex} = p_{ARL,t}$, i.e., for

$$t_t = p_{hex} \frac{t_{ARL} - 0.25}{1 - p_{hex}}. \quad (5.10)$$

This design rule has to be considered when developing a lithographical mask for the prestructuring of the n-Si wafer as described in 4.2.1. But although equation (5.10) yields equal *global* porosity within a unit cell, the symmetry at the boundary of bulk PhC and ARL is strongly disturbed ($C_{6\nu}$ within the bulk PhC \leftrightarrow $C_{2\nu}$ at the PhC/ARL interface). This leads to different *local* porosities within a unit cell resulting in a slight deviation in pore shape from ideally round pores. In addition, experimental results show a slight deviation of the diameter $2r_1$ of the last row of pores as compared to the diameter $2r_0$ in the bulk PhC as depicted in fig.5.10b. This is what is called the *proximity effect* (PE) in this work (experimental results are presented in section 5.4.2.1). Similar effects have already been observed in a less pronounced form in terms of long-wavelength

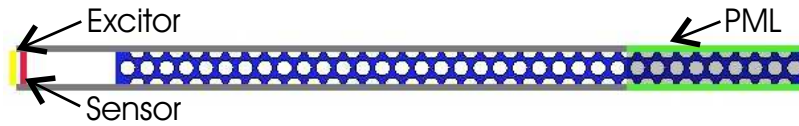


Figure 5.11: Structure used for the calculation of the dispersion of surface modes in the ARL concept. To keep the computational effort bearable, reflection R instead of transmission T was analyzed, assuming the relation $R = 1 - T$ holds.

birefringence [66][55] in 2D macroporous Si PhCs and during investigations of point defects [67]. The influence of smaller/larger pores at the ARL boundary on the transmission is shown in the left graph of fig.5.10a. The transmission strongly decreases for deviations $(r_0/a_0)/(r_1/a_0)$ of the r/a -ratio of the last row of pores of more than 2.5%. But this can be compensated by changing the thickness of the ARL layer as shown in the right graph of fig.5.10a for deviations of the radius r_1 of 2.5% and 5%.

5.4.2.2 ARL concept: working principle

The numerical simulations above have shown that the ARL concept is capable of considerably increasing the transmission through PhC structures. In the remainder of this section a physical model explaining the working principle of the ARL concept is suggested. It is based on coupling the incoming radiation to a surface mode resulting from the non-conventional air/ARL/PhC interface, succeeded by coupling the surface mode to the desired PhC gas sensing mode. Crucial points in this scheme are the surface grating constituted of the air holes next to the ARL and the fact that we are dealing with a *finite* PhC structure, i.e., the translational symmetry of infinite PhC structure is reduced³.

ARL and surface states At this point it should be mentioned that at the interfaces of bulk, i.e., unstructured dielectric materials usually no surface states, i.e., modes located at and confined to the interface exist because of the absence of a restricting mechanism⁴. In dielectric PhC structures, however, surface modes can exist in the frequency region of PhBGs. Because light within this spectral region cannot propagate in the PhC such modes can be confined to the surface [5][70][71][69][72][73].

The non-conventional PhC termination resulting from the ARL leads to the existence of surface states in the ARL. Their spectral position depends on the thickness t_{ARL} of the ARL. By changing t_{ARL} a surface mode can be tailored to spectrally overlap with the desired gas sensing bulk PhC mode, a necessary prerequisite for subsequent mutual coupling. Surface modes are confined to the interface region. As a consequence their wavevector component perpendicular to the interface is zero⁵.

³Only recently comparable schemes were used to explain transmission of light through sub-wavelength apertures in thin metal foils [68] as well as beaming and enhanced coupling phenomena for PhC waveguides [60][59]. However, the ARL concept in this work was developed independently.

⁴At air/metal interfaces surface modes are well known and called surface plasmon polaritons (*SPP*). The confinement to the surface is due to the finite conductivity of the metal. [69]

⁵This will be important when discussing coupling to incoming radiation and the PhC mode in the next

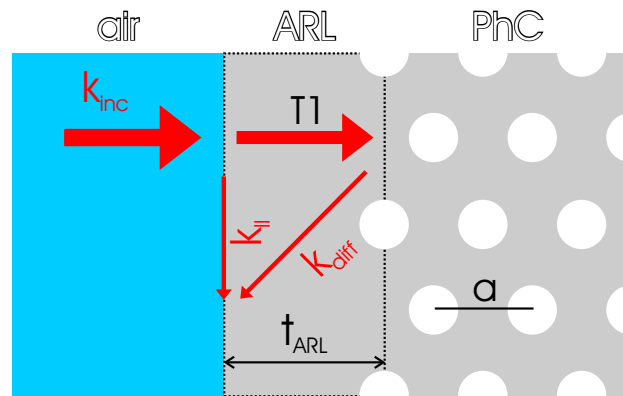


Figure 5.12: Working principle of the ARL concept. Light impinging from air enters the ARL and is diffracted at the ARL/PhC interface, thereby gaining a wavevector component parallel to the surface ($k_{||}$). This allows coupling to the surface mode in the ARL. Since the surface mode and the desired PhC mode spectrally overlap and have, in addition, very similar field distributions mutual coupling among them is possible.

For the calculation of the dispersion of the surface modes the *full, finite PhC structure* and not only *one unit cell* along the transmission direction (ΓK in our case) has to be used. In addition when periodic boundary conditions (*supercell* method [69]) are employed along the transmission direction, e.g., using MPB, relatively large air regions on the order of the width of the PhC structure itself on both sides of the PhC have to be used to prevent coupling of the surface modes of neighboring PhCs through the intermediate air region [72]. Numerical simulations show that the spectral position of the surface modes also slightly depends on the size of the supercell used. However, the results shown in fig.5.13 can be considered to be close to the true spectral position of the surface modes because a variation of the size of the supercell - which is restricted by the available computer hardware - shows that the shift of the spectral position of the surface state is below a few percent. Due to the ARL numerous surface states exist. In fig.5.13 for clarity only the surface states close to the target frequency of the gas sensor are shown. They were calculated using FL because this software allows to specify a target frequency around which bands should be calculated. Using MPB is not favorable here because due to the size of the supercell numerous backfolded bands have to be computed which is time consuming and produces a rather confusing PhBS in which reliable identification of the interesting surface states is almost impossible. The model used for the surface dispersion calculations using FL is shown in fig.5.11.

The spectral position of the surface modes depends on the surface termination of the PhC structure, i.e., on the thickness t_{ARL} of the ARL. Their dispersion is flat indicating their low group velocity along ΓM .

Coupling of light to a PhC using surface modes The key, that allows coupling of the incoming radiative modes in air to the surface mode in the ARL is the periodic modulation of the ARL/PhC interface, leading to diffraction of the incoming radiation. By this mechanism the incoming light with $|k_{||}| = 0$ acquires a wavevector component $k_{||}$ parallel to the surface and can

section.

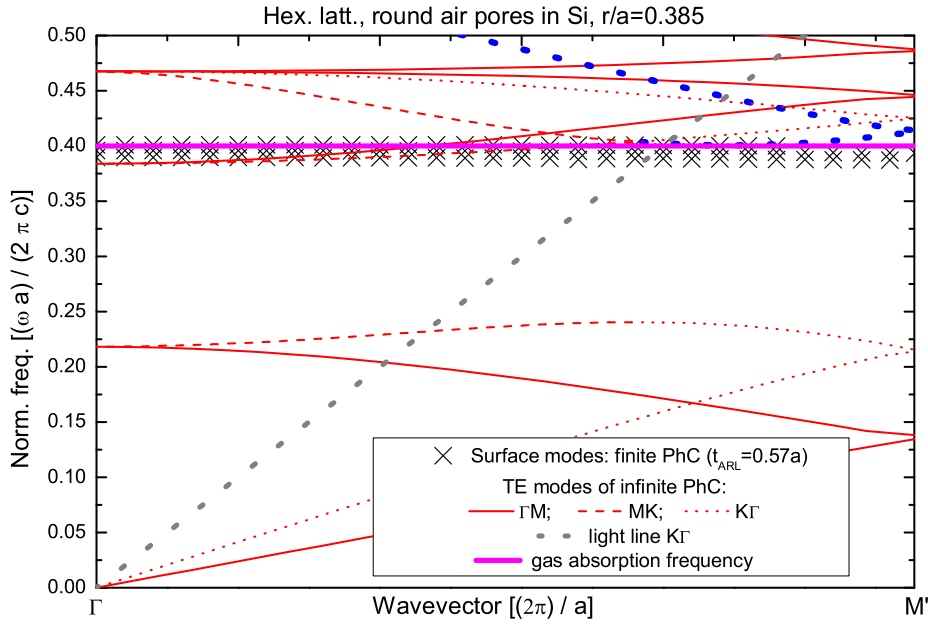


Figure 5.13: PhBS for the 1D BZ to be considered in the ARL concept. The PhBS shown in fig.5.1a is folded at the new BZ boundary $|\vec{M}'| = 0.5|\vec{M}|$ (red lines). The red lines indicate the TE bands of the infinite PhC projected onto the $\Gamma M'$ direction. Solid, dashed and dotted lines indicate that the projected band originates from the ΓM , MK and ΓK direction, respectively. For clarity, the bulk TE_{02K} mode intended to be used for gas sensing is highlighted in blue. The spectral position of the gas absorption line is given by the solid magenta line. In addition the dispersion of the relevant surface modes (black lines) close to the gas sensor target frequency at $a/\lambda = 0.405$ is shown. (Surface modes calculated using FEMLAB and the structure shown in fig.5.11 by D. Pergande, Univ. Paderborn.)

couple to the surface mode, compare fig.5.12.

When considering transmission through a *finite* PhC structure the unit cell used to describe the system is no longer the regular hexagonal lattice shown in fig.4.1a but a one dimensional unit cell has to be used. The *finite* PhC structure possesses translational invariance only along the air/PhC interface (ΓM direction in our case) with a basis vector $\vec{a}_{\text{int}} = a_0\sqrt{3}$ and a corresponding reciprocal basis vector $\vec{b}_{\text{int}} = \frac{2\pi}{a_0\sqrt{3}}$. The length of the BZ in ΓM direction for the conventional hexagonal unit cell is $|\vec{M}| = \frac{2\pi}{a_0} \frac{1}{\sqrt{3}}$ while it is $|\vec{M}'| := |\vec{b}_{\text{int}}| = \frac{\pi}{a_0} \frac{1}{\sqrt{3}} = \frac{|\vec{M}|}{2}$ in the finite PhC case. This has to be taken into account when comparing the PhBS of the *infinite* PhC used in the gas detection region and the situation of the *finite* PhC used for transmission considerations and is shown in fig.5.13. As derived in A.2, light with $\frac{a}{\lambda} > 0.17$ impinging onto the ARL/PhC interface experiences Bragg diffraction. The k -vector of the PhC surface grating along ΓM is $\frac{1}{\sqrt{3}} \frac{2\pi}{a} \equiv 2|\vec{M}'|$. This means that light diffracted into the first order can couple to the surface modes at the Γ point which lies above the light line, see fig.5.13. Due to the flat dispersion of the surface modes along $\Gamma M'$ this light can be regarded as *stored* in the surface mode, slowly

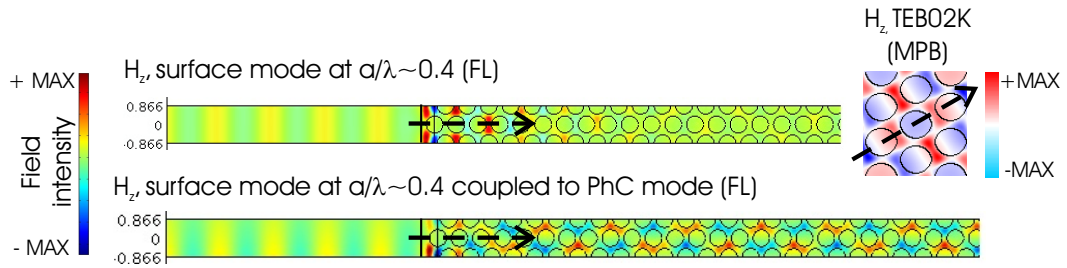


Figure 5.14: Field distributions of H_z for the surface mode (top left) and the desired PhC mode (top right). The arrow marks the ΓK direction. The field distributions look very similar and therefore allow easy coupling between the two modes, as shown in the bottom picture where a surface mode coupling to the desired PhC mode is shown. (Calculations assisted by D. Pergande, Univ. Paderborn).

moving along the air/ARL interface.

Since for the finite PhC no periodicity along the direction perpendicular to the interface exists, as a consequence no dispersion relation along this direction exists. One has to consider the PhBS of the *infinite* PhC projected onto the 1D Brillouin zone of the *finite* PhC. This is shown in fig.5.13. The solid red lines depict the PhBS of the infinite PhC along ΓM folded back onto the $\Gamma M'$ direction of the finite PhC. Because ΓM and $\Gamma M'$ are parallel and ΓM is twice as long as $\Gamma M'$, projecting here simply means to mirror the PhBS of the infinite PhC at $0.5\Gamma M'$. For the other high symmetry directions MK and ΓK the corresponding PhBS has to be projected onto the $\Gamma M'$ direction by taking the wavevector component of MK and ΓK parallel to the $\Gamma M'$ direction, respectively. This is depicted by the dashed and dotted red lines in fig.5.13. The dotted blue line highlights the TE02K mode intended to be used for gas detection. Also the light line along ΓK projected on $\Gamma M'$ is plotted because the PhC-based gas sensor is designed to operate in transmission along ΓK .

In fig.5.13 the spectral overlap of the gas absorption frequency, TE02K and the surface states for $t_{\text{ARL}} = 0.57a$ is obvious.

In addition, the field distributions of the surface mode and the desired PhC mode (TE02K) shown in the upper part of fig.5.14 look very similar. Therefore easy coupling between the two modes is possible, as depicted in the lower part of fig.5.14 where a surface mode coupling to a PhC mode is shown.

Finally, fig.5.15 shows the distribution of the H_z component of the magnetic field (left) and for transmission through a PhC structure designed for sensing of SF_6 . The high amount of energy stored in the surface mode in the ARL is clearly visible.

On the output side the same mechanism is used for the coupling of the light transmitted through the PhC to air, where it can then be detected by a sensor.

However, a flaw comes along with the ARL concept. As a consequence of utilizing a surface state to couple impinging radiation to the desired PhC mode, information about the original wavevector \vec{k} is lost after coupling to the surface mode. Light stored in the surface mode can couple to any Bloch mode having the same frequency (i.e., energy) and suitable field distribution and \vec{k} . One of these modes is the TE02K mode intended to be used for gas detection, but energy transferred to other modes results in reduced transmission. For the PhC-based gas sensor design discussed

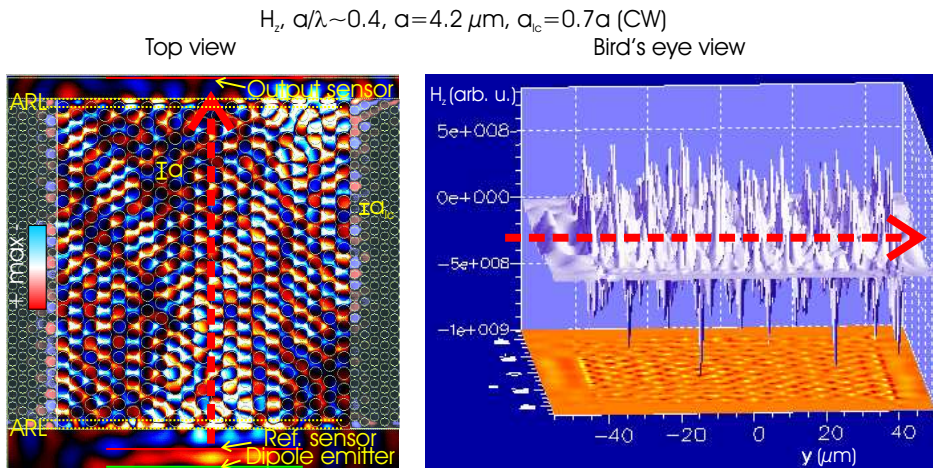


Figure 5.15: Distribution of H_z in a macroporous Si PhC structure designed for SF_6 detection. High fields can be seen in the ARL region, indicating the storage of energy in the surface mode. The asymmetry in the distributions stems from the asymmetric grid created by CW. Furthermore, the effect of the additional PhCs on each side of the central PhC responsible for lateral confinement discussed in 5.4.2 is clearly visible (brighter regions left and right). The dashed red arrow marks the direction of transmission. (CW calculation, round air holes in Si, $t_{\text{ARL}} = 0.57a$, $r/a = 0.385$, 2^{17} time steps, $\text{grid} = \frac{a}{16}$, TE polarization, $a = 4.2 \mu\text{m}$, $a/\lambda = 0.398$)

here, there is one TE band (TEB02M) along the ΓM direction to which energy could be lost⁶. However, the field distribution of the surface mode is more similar to the TEB02K mode than to the TEB02M band. Furthermore, light lost to directions other than the intended transmission direction, can be partially retrieved by using the lateral confinement concept discussed in 5.4.2 and fig.5.8.

5.4.2.3 ARL concept: conclusions

A new⁷ concept to drastically enhance transmission through bulk PhCs - entitled ARL - was developed. Numerical simulations using different methods (FDTD, FEM) show an increase in transmission of more than a factor of 2, even for flat bands. Furthermore the ARL concept has proven stable under variation of incidence angle and it also allows to compensate for the proximity effect occurring during fabrication of the PECE 2D macroporous Si-based PhCs. A physical model to explain the working principle of the ARL concept was developed and discussed.

5.4.3 PhC gas sensor: absorption enhancement

After having designed the PhC-based interaction volume for light and gas in section 5.3.5 and a successful connection of this interaction volume to the outside world by using the ARL concept in

⁶The TM bands along ΓM and ΓK directions located at the same frequency have the wrong polarization to couple strongly to the surface mode.

⁷The existence of surface modes in PhC structures was known for about a decade, but their application to enhance coupling and transmission through PhC structures is conceptually new and has only recently been published, e.g., in [59].

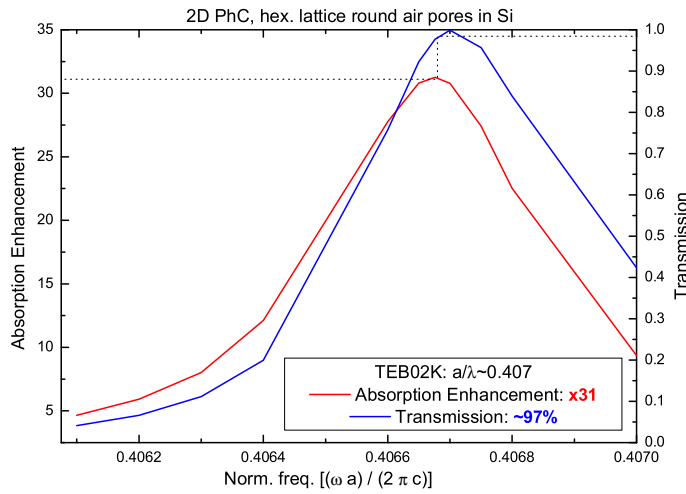


Figure 5.16: Absorption enhancement. The expected increase in interaction between light and gas within a PhC interaction volume is on the order of 30, while still achieving high transmission of about 97%. (FEM calculation, A.v. Rhein, Univ. Paderborn)

section 5.4.2, the effect of the expected enhancement in gas/light interaction has to be investigated. For this purpose it is necessary to have a software that allows calculations using a *complex* dielectric constant to account for the absorption of the gas within the pores. Using FEMLAB both the transmission through a PhC interaction volume with ARL and the corresponding absorption enhancement can be calculated, as shown in fig.5.16. The absorption enhancement (AE) is calculated by comparing the transmission through a conventional interaction volume filled with gas to the transmission through a PhC-based interaction volume of the same size. For the given parameters an AE on the order of 30 is achieved while still allowing very high transmission of about 97% through the (low v_g) structure.

5.4.4 PhC gas sensor: design results

In this chapter the design for a PhC-based spectroscopic gas sensor was developed. Three major points were successfully investigated:

First, the interaction volume was designed for a PhC-based spectroscopic gas sensor tuned to SF_6 detection. A macroporous Si PhC with a hexagonal lattice with $a = 4.2 \mu m$ and an $r/a = 0.385$ are the parameters to be used. Tunability and robustness under expected operating conditions of the design were numerically shown.

Second, efficient coupling of impinging/outgoing radiation to/from the desired PhC Bloch mode was achieved using the novel ARL concept. The optimal ARL thickness was numerically determined to be $t_{ARL} = 0.57a$ for the purpose described above using FDTD and FEM schemes. The robustness of the ARL concept under non-perpendicular incidence as well as compensation of the PECE proximity effect has been shown.

Third, the expected absorption enhancement was numerically determined to be on the order of about 30 while still achieving very high transmission ($> 90\%$).

In the next chapter the practical realization of structures having the above parameters will be discussed.

Chapter 6

Fabrication of PhC gas sensor structures

For the fabrication of the PhC gas sensor structures the macroporous Si material system was chosen. After a brief description of the state-of-the-art of this fabrication process at the onset of this work the further development necessary for the realization of PhC gas sensor structures is presented in the subsequent section. These developments are essentially etching of deep ($\geq 450 \mu\text{m}$), parallel pores, realization of the different taper concepts discussed in chapter 5 and aspects of device integration.

6.1 Why macroporous Si ?

For PhCs in the IR spectral region the dielectric materials used for their realization have to be transparent, i.e., have negligible absorption in that wavelength range. Furthermore it must be possible to periodically structure these materials on an appropriate length scale, i.e., on the order of a few μm . Si fulfills both requirements. As a semiconductor with an electronic band gap of 1.1 eV it is transparent from the FIR spectral region down to a wavelength of $\lambda = 1.1 \mu\text{m}$. Furthermore, Si is the dominating material in today's microelectronics industry and a lot of experience and methods for Si structuring exist. Unfortunately, these conventional methods are well suited for lateral structuring, i.e., features in the x-y-plane, but allow only rather shallow vertical

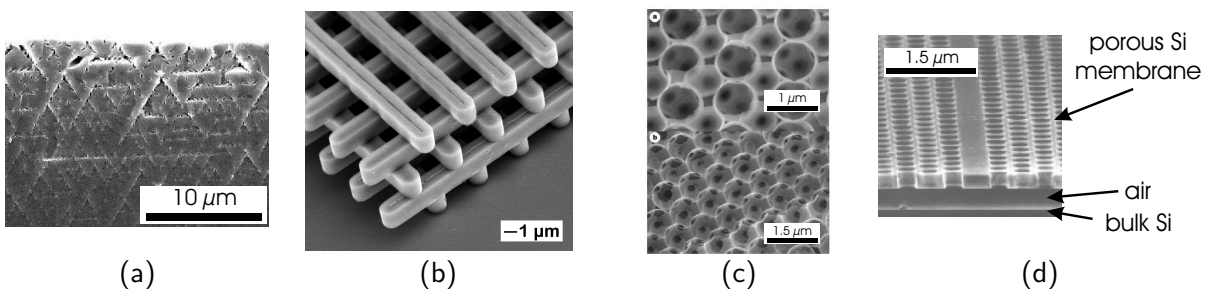


Figure 6.1: (a) *p*-type macroporous Si Kielovite structure [74]; (b) Si Lincoln-Log structure [75]; (c) [110] and [111] facets of a Si inverse opal structure [76]; (d) porous Si membrane [77].

features to be realized. For PhCs, however, it is necessary to realize high aspect ratio structures in Si along the vertical, i.e., along the z-direction.

Several techniques to realize PhC structures in Si have been developed and some results are shown in fig.6.1. The structure in fig.6.1a is called *Kielovite*, named after the German city in which it was invented and realized by photo-electrochemically etching pores into [111] oriented p-type silicon [74]. Unfortunately this pore growth regime is not very stable resulting in limited structuring along the vertical direction.

Another possibility for structuring of Si along the z-axis is the so-called *Lincoln-Log* structure shown in fig.6.1b fabricated by Lin et. al [75]. In this layer-by-layer approach the structure is fabricated by depositing a layer of SiO₂, subsequent lithographical pattern definition, dry etching of the defined trenches, followed by infiltration of poly-crystalline Si into the trenches. By repeating this procedure a 3D PhC can be obtained. But due to the time consuming nature of this approach ($\approx 2\text{...}4$ weeks per layer) the largest so far realized Lincoln Log possessed only 4 repetitions of the unit cell along the z-direction.

Another technique, that manages to get along without complex and costly lithography steps, is based on self-organization of colloidal particles and subsequent infiltration of the structure with Si followed by removal of the colloids, as shown in fig.6.1c [76]. While such structures can in principle be built having several dozens of unit cells in the vertical direction, their major shortcoming is the relatively high defect concentration resulting from the fabrication process.

The structure shown in 6.1d was produced by using conventional semiconductor processing techniques. After patterning the Si by dry etching the sacrificial layer underneath was removed resulting in a free standing Si membrane with an incorporated *W1* PhC waveguide. The fabrication of such a structure is rather straightforward but its disadvantages are mechanical instability and only low achievable aspect ratios.

Unfortunately, the above described methods cannot be used for the realization of a PhC-based gas sensor because the interaction volume realizable with the above procedures is too small, mainly due to the limits in vertical structuring depth. A method that allows Si structuring in the *x-y*-plane as well as along the vertical z-direction is the macroporous Si fabrication process, demonstrated by Lehmann and Föll [47][46], which is described in the following section.

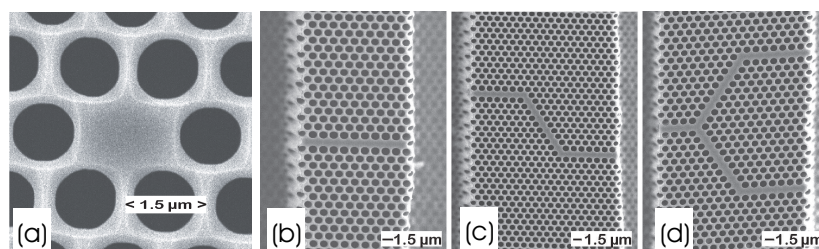


Figure 6.2: SEM micrographs of defect structures in a hexagonal lattice of air pores in Si. **a)** Point defect or cavity. **b), c)** Straight and bent linear defects. **d)** Y-branch.

6.2 Macroporous Si for PhCs: state-of-the-art in 2002

Fabrication of macroporous Si structures to realize bulk 2D PhCs has been a well established technique at the Max Planck Institute of Microstructure Physics (*MPI MSP*) in Halle at the beginning of the PhC gas sensor project in 2002. It was shown that an aspect ratio of ≈ 20 is sufficient to treat the macroporous structures as real 2D PhCs, i.e., the extension along the z -direction parallel to the pores does not have a significant influence on the PhBS. For the lattice constants typically used so far ranging from 0.5-1.5 μm a pore depth of less than 100 μm was therefore sufficient. The structures were typically characterized by IR reflection measurements perpendicular to the pores. The interfaces for the optical measurements were realized by cleaving the macropore arrays along either ΓK or ΓM directions, which in turn were oriented along the Si [110] directions. The incorporation of single point and W1 line defects in hexagonal macropore arrays had been realized. Furthermore, in a cooperation with the group of H. van Driel in Toronto it was shown that it is possible to measure transmission through a PhC consisting of up to about 180 pore rows. This catwalk of macropores had been realized by post-processing the PECE macropore array using lithography and a subsequent dry etching process [78]. A few examples of the above described structures are given in fig.6.2.

6.3 PECE of deep pore arrays

For realization of macroporous Si structures to be used as the interaction volume in PhC-based gas sensors, structures with aspect ratios as high as possible should be used. An IR light source to be used in a PhC-based gas sensor should be broadband and cheap. This excludes the use of, e.g., QCLs, light emitting diodes (*LED*) or lead-salt-lasers. Therefore the likely IR light source will be a simple thermal emitter. Radiation coming from such a thermal emitter is rather divergent. To couple an appreciable amount of it into the PhC - even with the help of some optical elements - the macroporous structure should be as high as possible.

The physical limit for the maximum pore depth is given by the thickness of standard 4-6 inch diameter Si wafers ($\approx 525 \mu\text{m}$) minus the absorption length of the (IR) light used to create the electronic holes for the PECE process (a few μm). Deeper pores could in principle be realized by using standard Si wafers with a thickness of about 700 μm . But taking into account fabrication time and cost issues, an increase in pore depth is not attractive because for standard PECE conditions using HF with a concentration of 5wt% and temperatures around 10°C typical etch times of 10-16 hours are necessary to etch 400-450 μm deep macropores. For pores with a depth of 700 μm the etching time would be on the order of 24-30 hours. Furthermore, the quality of thick Si wafers concerning electronic hole lifetime in the material is a critical issue when it comes to PECE of deep pores.

The functionality of the PhC interaction volume in a spectroscopic gas sensor depends on the PhC's band structure. The PhBS in turn depends on the distribution of the dielectric material. For the fabrication of the macroporous Si structures this means that *deep* macropores with *parallel walls* and *smooth* pore surfaces have to be etched. While the pore walls can be smoothed after the PECE by growth of thermal oxide and a subsequent HF-dip, the parallel shape of the pores has to be realized already during the PECE process.

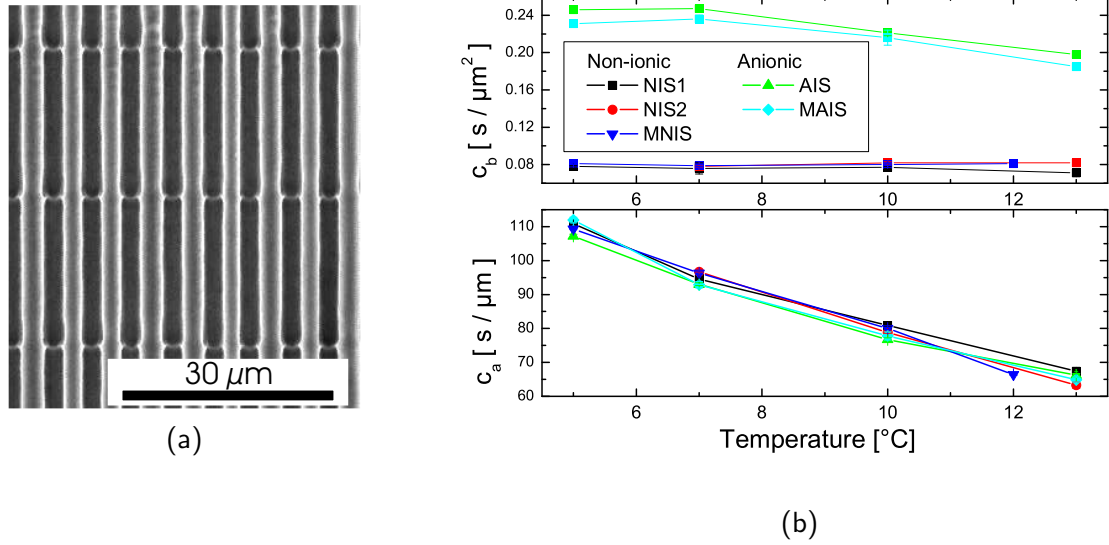


Figure 6.3: PECE of deep macropore arrays. **a)** Electrical breakdown pores used as depth markers. **b)** c_a (bottom) and c_b (top) in the Lehmann model for some surfactants used in this work as a function of temperature. NIS1: **n**-**o**n-**i**onic **s**urfactant **v**ery **s**imilar to the one used by Lehmann, NIS2: **n**-**o**n-**i**onic **s**urfactant, AIS: **a**n-**i**onic **s**urfactant, MAIS (MNIS): **M**ix of **a**n-**i**onic and **n**-**o**n-**i**onic **s**urfactants, dominated by anionic and non-ionic surfactant, respectively.

The empirical model of Lehmann[49] underlying the software controlling the PECE process is based on a 2nd order polynomial relation between the pore depth l_{pore} and growth time t_l necessary to achieve this depth according to

$$t_l = c_a l_{\text{pore}} + c_b l_{\text{pore}}^2 \quad (6.1)$$

with parameters c_a and c_b to be determined from the experiment.

Using Lehmann's values for c_a and c_b , significant deviations of sometimes more than 20% - depending on the detailed PECE parameters - of the measured pore depth compared to the desired pore depth were found. The effect was more pronounced for deep macropores with $l_{\text{pore}} > 150 \mu\text{m}$. In addition it was found that the deviation strongly depends on the type of surfactant added to the electrolyte.

To determine the parameters c_a and c_b relevant for the PECE of deep macropores in this work, depth markers were set during the PECE process by suddenly increasing the externally applied voltage by 20 V for 1 min¹. This leads to the formation of sharp features as shown in fig.6.3a. Their positions along the macropore have been determined using SEM and were then related to the instance of time during PECE when the increased voltage was applied. A least-square-fit using (6.1) to this data yields the parameters c_a and c_b shown in fig.6.3b.

Addition of surfactants to the electrolyte is necessary to avoid formation of gas (H₂) bubbles on the surface of the sample which would prevent HF exchange between the HF reservoir and

¹Depth markers produced by this technique allow a much more precise determination of the marker's position along the pore axis than utilization of conventional depth markers realized by diameter variations of the macropores. It was verified that these unconventional depth markers do not significantly alter the PECE process and therefore yield the same results as in case of diameter modulated macropores.

the macropores, thereby leading to inhomogeneous etching. Two types of surfactants were used: anionic and non-ionic. The concentrations of the surfactants in the electrolyte were chosen to allow stable macropore growth². Addition of anionic surfactant (AIS)³ of concentration c_{AIS} leads to slower pore growth than expected while addition of non-ionic surfactant⁴ (NIS1, NIS2) of concentrations $c_{NIS,1}$ and $c_{NIS,2}$ results in deeper pores than anticipated. The increase in growth speed was less pronounced for NIS1. The surfactant NIS1 is similar to the one originally used by Lehmann et al., but due to environmental concerns no longer available. To ensure the applicability of the concepts developed in this work for potential large scale production of macroporous Si-based PhC gas sensors investigation of the PECE process using the nowadays available successor of NIS1, namely NIS2, was necessary.

Furthermore it can be seen in fig.6.3b that in the case of a mixture of non-ionic (MNIS) and anionic (MAIS) surfactants added to the electrolyte the dominant species, i.e., the species being present with the higher effective concentration, determines the behavior of the pore growth speed. While the values for c_a are similar for all kinds of surfactants, there is a striking difference in the values for c_b for (mainly) non-ionic and (mainly) anionic surfactants.

Grüning related the meaning of the coefficient c_a to the inverse of the initial growth speed of the macropore and c_b to the inverse of the diffusion constant D_{HF} of the HF molecules within the macropores [80]. The data derived in this work is not in agreement with her findings because one would expect an increase in HF diffusion with increasing temperature. For the c_b of the anionic surfactants the opposite is found while for the c_b of the non-ionic surfactants no temperature dependence of the c_b is found. Furthermore, within the model of Grüning, dark currents lead to an additional reduction in pore growth speed. Dark currents arise from HF consumption along the pore wall, i.e., Si etching, at the pore wall/HF (not the pore tip/HF) interface and are on the order of a few $\mu\text{A}/\text{cm}^{-2}$. As a consequence the HF concentration along the pore is further reduced and the growth speed according to (4.33) is reduced and the pore walls are no longer parallel but wedged. This effect becomes important especially for deep pores with large surface area. Based on this model, the faster (slower) etching using non-ionic (anionic) surfactant corresponds to lower (higher) dark currents for the non-ionic surfactant. However, experiments show that the dark currents are higher for the non-ionic surfactant [79]. The lower dark current in the case of anionic surfactant could be explained by an increase in surface potential at the HF/Si interface due to the presence of the anionic species at this interface, thereby aggravating the tunneling of electrons from the electrolyte into the Si. Another observation is that the pore diameter is usually significantly smaller ($\gtrsim 25\%$) than the desired one when using anionic surfactants. From the slower growth rate for anionic surfactants mentioned above one would however expect a larger pore diameter. This is a hint towards a change in the valence n_{val} (compare (4.33)) depending on the type of surfactant used. The observed different behaviors of the anionic and the non-ionic surfactants is not due to changes of the pH-value of the electrolyte depending on the surfactant used, because all the surfactants had approximately the same pH-value of 7-7.5.

Grüning did not specify which/what kind of surfactant and in which concentration was used for her investigations. In addition her goal was to model the PECE behavior using HF concentration and temperature. The influence of different surfactants was neither included in her model nor in

²Stable macropore growth could not be achieved with cationic surfactants [79]

³SLS: Sodium dodecyl sulfate, $\text{C}_{12}\text{H}_{25}\text{NaO}_4\text{S}$, $c_{AIS} = 0.1 \text{ mM}$

⁴ $c_{NIS,1} = c_{NIS,2} = 1 \text{ ml}/90 \text{ l HF (5-7wt\%)}$

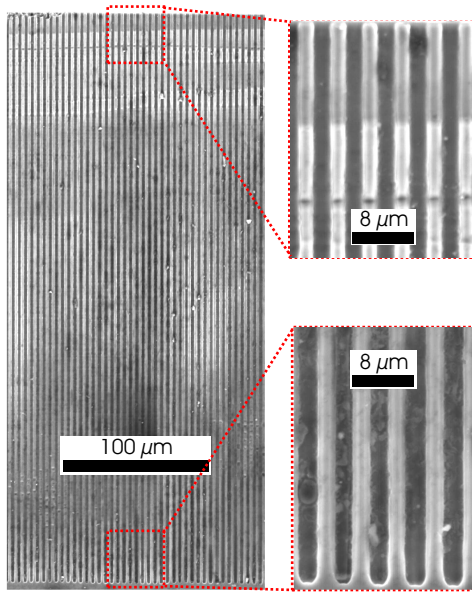


Figure 6.4: Parallel, deep PECE macropores (hex. lattice, $a = 4.2 \mu\text{m}$) with a depth of about $390 \mu\text{m}$. The relative difference of the pore diameters at the top and the bottom of the sample is 0.2%.

her experimental investigations.

All this shows that the processes at the Si/HF interface are rather complex. A detailed study taking into account all relevant microscopic processes, especially the chemical reactions at the interface, has not been undertaken so far and is far beyond the scope of this work.

The main result of this section is the determination of the coefficients c_a and c_b in (6.1) shown in fig.6.3b for the etching parameters relevant for this work because they allow growth of macropores with the desired depth. Fig.6.4 shows an SEM micrograph of $390 \mu\text{m}$ deep macropores with a relative difference of the pore diameters on top and bottom of the sample $\Delta(2r) := \frac{2r_{\text{top}} - 2r_{\text{bottom}}}{2r_{\text{top}}}$ of only 0.2%.

6.4 Realization of PhC tapers in the macroporous Si material system

6.4.1 Adiabatic PhC Taper

As the PECE of macropores in n-type Si provides the freedom to define the pore pattern geometry by lithography, the adiabatic taper concept described in 5.4.1 was implemented by combining regular hexagonally arranged pores together with pores arranged in a distorted hexagonal lattice. An SEM micrograph of the situation is shown in fig.6.5. The green region exhibits pores arranged in a regular hexagonal pattern. This region is intended to be used for gas detection. The regions highlighted in red have pores arranged in distorted hexagonal lattices and are intended to be used for coupling incoming light either along ΓK_1 or ΓM_2 directions. In these regions the hexagonal lattice is distorted along the coupling direction (ΓK_1 and ΓM_2 , respectively, as shown in fig.5.4b). The taper shown is rather abrupt, consisting of only one intermediate step of one pore row (framed by the dotted line) with lattice constant a_t between the coupling lattice constant a_c and $a_0 = 4.2 \mu\text{m}$.

Within all regions and also at the interfaces between coupling and detection regions macropore

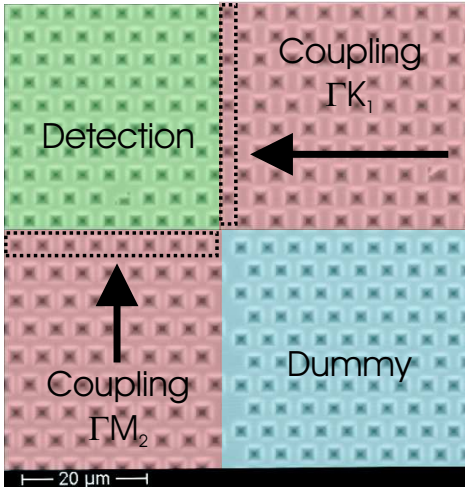


Figure 6.5: Realization of the adiabatic PhC taper during PECE. The green region shows the macropores arranged in a regular hexagonal pattern while the red regions having distorted hexagonal lattices are used for coupling. The blue region is a dummy incorporated to maintain average macropore porosity throughout the sample. Only the lower right part of the actual (square shaped) device is shown. The output sides (left for ΓK_1 and top for ΓM_2) of the (square shaped) device is designed in the same way. The dotted lines frame the taper step used.

growth was found to be stable. This can be mainly considered as a consequence of the only slight disturbance of the ideal, i.e., undistorted hexagonal lattice case⁵.

6.4.2 Anti-Reflection-Layer: PECE of deep trenches

The above described realization of an adiabatic PhC taper by distortion of the hexagonal lattice is similar to PECE of *perfectly ordered* macropore arrays in terms of *etching pores next to pores* - with a minor change in symmetry and interpore distances.

For the realization of the ARL during PECE it was necessary to go a step further. A trench has to be etched next to an ordered array of macropores, within a distance of less than one lattice constant of the ordered pore array. Such a procedure disturbs the PECE process by far more than the adiabatic taper scheme. The approach and the results are presented in the following part of this chapter.

Keeping in mind the design rule of constant porosity within a unit cell stated in 5.4.2.1 the ARL layer can be realized by lithographically defining a trench to be etched next to the last row of pores of the interaction volume as schematically depicted in fig.6.6a. The thickness t_{ARL} of the remaining ARL - as defined in the theoretical design in section 5.4.2 - is given by the distance of the edge of the trench and the center of the adjacent pores as shown in fig.6.6b. By lithography the x - y -positions of the pores and the trench are fixed. But the width of the etched trench depends on the r/a ratio chosen during PECE according to

$$t_t = \frac{\pi \left(\frac{r}{a}\right)^2 (2t_{\text{ARL}} - 0.5)}{\sqrt{3} - 2\pi \left(\frac{r}{a}\right)^2} \quad (6.2)$$

with the symbols used in fig.6.6a. As a consequence the intended r/a ratio necessary for spectral overlap of the PhC gas sensing mode with the gas absorption frequency has to be taken into account when defining the position of the trench on the lithography mask. Because the above arguments are based on simple geometric considerations and the assumption of a homogenous distribution of charge carriers it is not expected that the desired ARL thickness is precisely achieved

⁵Equipotential surfaces for this situation are shown in fig.7.2

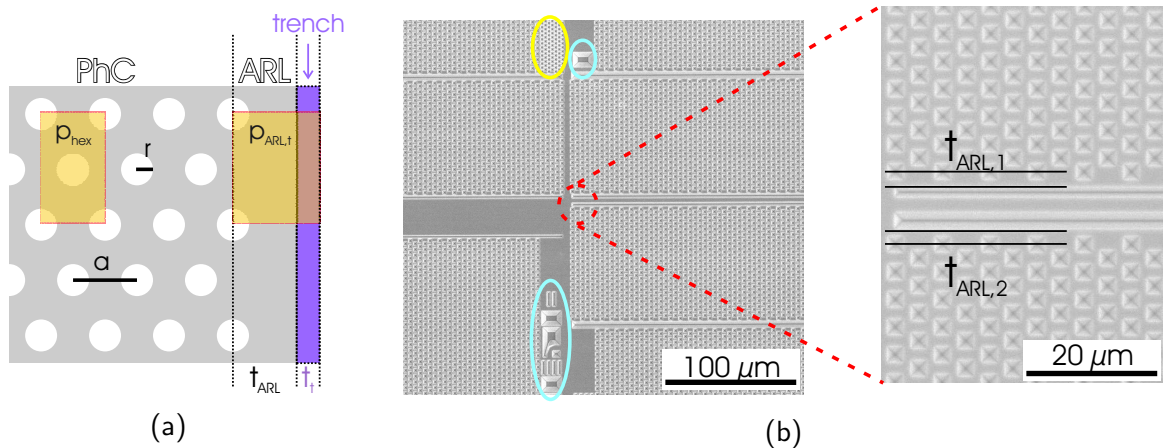


Figure 6.6: Realization of the ARL during PECE. **a)** Design principle **b)** SEM micrographs of the etch pits for the macropores and the trenches in a Si wafer. Left: overview. Right: zoom revealing ARLs with different thicknesses. The yellow and blue circles mark a region with smaller lattice constant for the lateral confinement discussed in 5.4.2 and markers allowing distinction of the individual devices on the wafer, respectively.

after PECE. For this purpose a series of ARLs with different thicknesses around the desired optimal t_{ARL} has to be implemented on the lithography mask.

It should be mentioned that PECE of trenches has been published before by Barillaro et al. [81][82]⁶. However, the trenches etched by Barillaro et al. were parallel to each other, i.e., they etched *trenches next to trenches* where the symmetry in the vicinity of each trench was the same, namely C_{2v} . In contrast in the design developed in this work, a plane trench faces a corrugated boundary made up by the adjacent air pores. For this reason it can be expected that stable growth of the trenches facing the macropores is harder to achieve and deserves investigation. Furthermore, while using comparable lattice constants of about 4-6 μm , the depth of the published trenches is limited to about 30 μm , corresponding to relative low aspect ratios below 10. For comparison, the goal in this work is to achieve macropores and trenches with an aspect ratio $\gtrsim 150$.

Fig.6.7 depicts successfully etched, 450 μm deep trenches next to arrays of hexagonally arranged macropores. Both, the macropores as well as the trenches grow stable. However, an increase in roughness of the ARL surface is observed with increasing depth. This issue is discussed in 7.1. Due to the observance of the before stated design rules, stable trench-next-to-macropores-growth could be achieved by using PECE parameters comparable to the parameter set used for the fabrication of pure macropore arrays.

However, it is clear that constant porosity in the bulk PhC and the ARL/trench regions is a necessary but not sufficient prerequisite to achieve stable macropore/trench growth. If the system is disturbed too much by, e.g., creating too thick ARLs with $t_{\text{ARL}} \gtrsim 1a$ the PECE process becomes unstable. As a result dying of trenches or branching of pores and trenches is observed as shown in fig.6.8.

⁶Christophersen et al. also report on the growth of deep trenches using PECE [83]. But they did not lithographically define trenches to be etched but were investigating Si dissolution and underetching at the edge of a large masked area. Their trenches were only several 10 μm deep and the shape was strongly wedged.

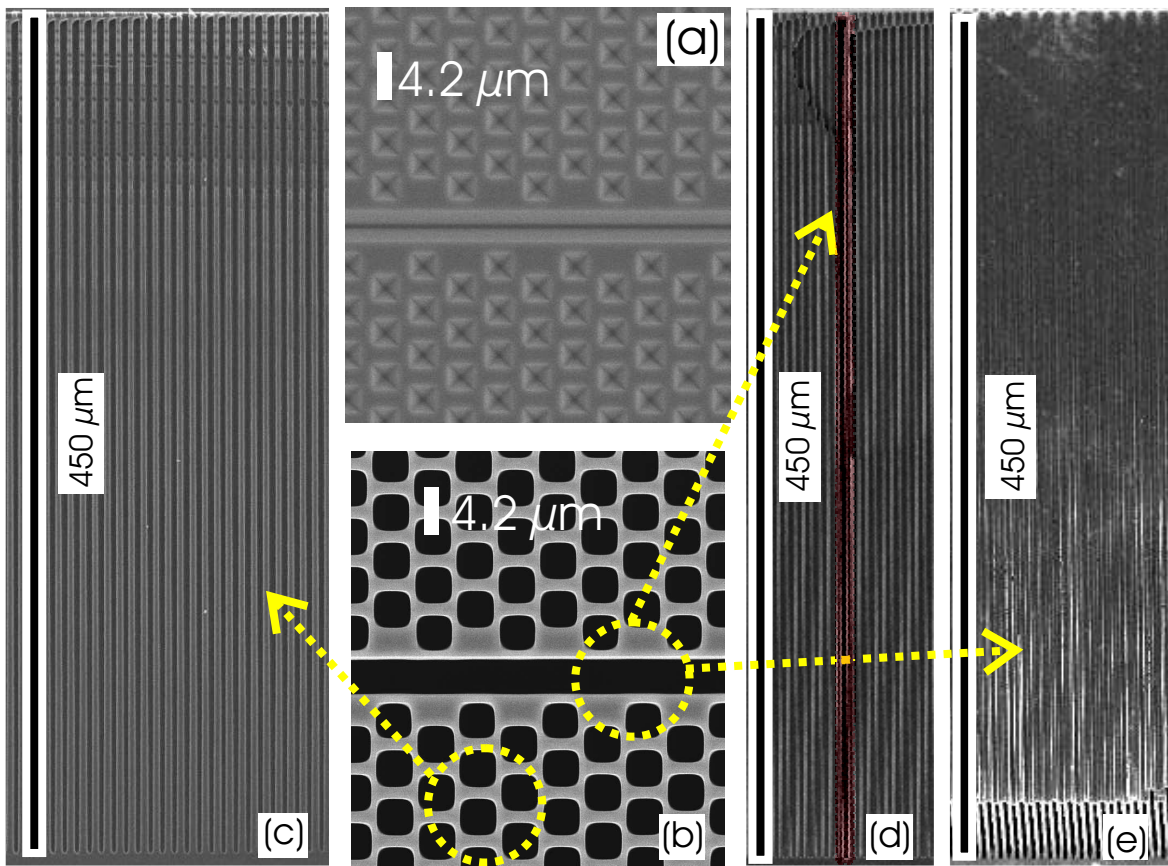


Figure 6.7: Deep trenches next to macropores realized by PECE (SEM micrographs). **a)** Lithographically prestructured *n*-Si wafer (top view). **b)** Trench and adjacent macropore array after PECE. **c)** Side view of the cleaving edge through the macropore array. **d)** Side view of the cleaving edge perpendicular to the trench. (trench highlighted by the red dotted line) **e)** Side view of the cleaving edge parallel to the trench. (The broken trench surface at the bottom is a consequence of cleaving.)

PECE of trenches, which was originally investigated to enable highly efficient coupling to macroporous Si PhC structures, opens the possibility to realize additional interesting structures. Figs.6.9a and d show how PECE trenches next to macropore arrays can be used to precisely define thin

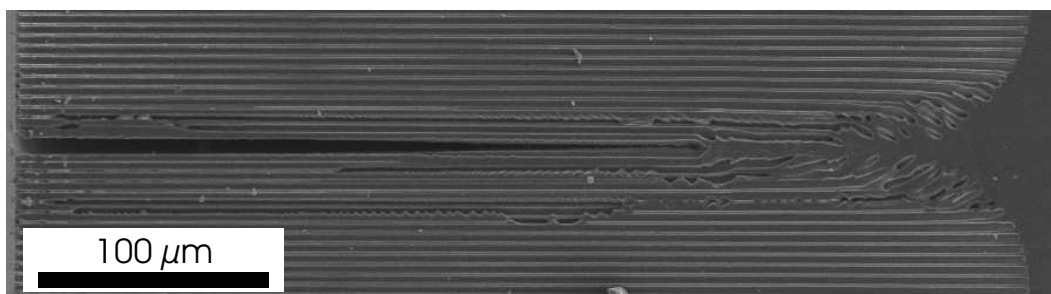


Figure 6.8: Trench etched next to a macropore array. The nominal thickness of the ARL is $t_{\text{ARL}} = 1a$, resulting in unstable PECE conditions which in turn lead to branching and dying of pores and trenches.

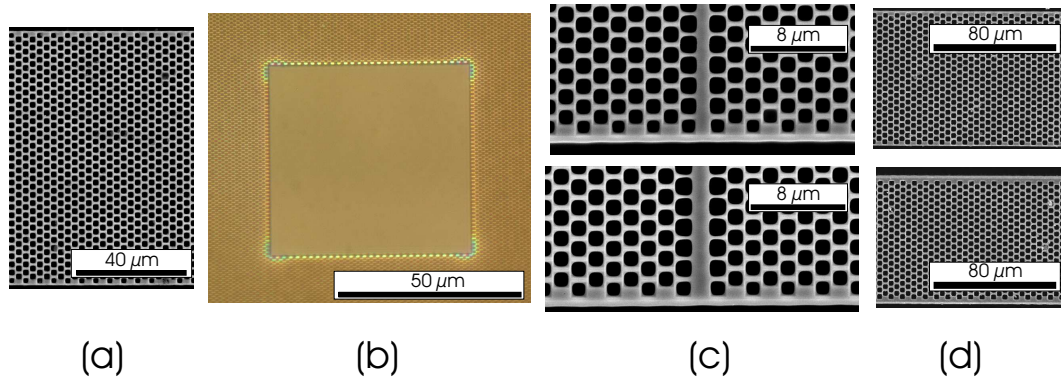


Figure 6.9: PECE trenches: **a)** two trenches used to define a thin stripe of 61 pore rows in ΓK direction ($a = 2 \mu\text{m}$). **b)** Trenches along ΓK and ΓM directions to realize a $50 \times 50 \mu\text{m}^2$ hole within a macropore array. ($a = 2 \mu\text{m}$) **c)** $W0.7$ (top) and $W1$ (bottom) PhC waveguides, terminated with an ARL. ($a = 2 \mu\text{m}$) **d)** Two trenches used to define thin stripes of 35 (bottom) and 39 (top) pore rows in ΓK direction ($a = 4.2 \mu\text{m}$). (SEM: a, c, d; optical microscope: b)

stripes of arbitrary numbers of pore rows along, e.g., the ΓK direction. While this is shown for lattice constants of $2 \mu\text{m}$ and $4.2 \mu\text{m}$ in fig.6.9a and d, respectively, trench etching is expected to work in principle independent of the lattice constant of the macropore array. These thin stripes are generated during the PECE process without any post processing (except from cleaving using a pair of tweezers). By standard procedures, i.e., inscribing the Si with a diamond scribe and mechanical cleaving, such thin stripes cannot be realized. The thin macropore stripes can, e.g., be used to determine the transmission through macroporous Si structures as a function of the sample length. However, effects resulting from the presence of the ARL have to be accounted for. The importance of the surface termination not only of bulk PhCs but also of PhC waveguide structures has been discussed in literature theoretically [59]. Experimentally, beaming was found to occur at the output side of a $W1$ waveguide in macroporous Si structures with conventional surface termination [84]. The now available macroporous Si structures with ARL terminations of varying thickness allow verification of the theoretically predicted effects. Such experiments are planned for the near future. Fig.6.9c shows that PECE of trenches allows realization of well defined, macroscopic hole structures in macropore arrays. The macropore array in the center of the hole can easily be removed after membrane fabrication by pushing with a small tip or blowing with pressurized air. These holes could be used to host light sources, for mechanically mounting macroporous Si structures onto device substrates, as electrical feedthroughs or for alignment purposes.

6.5 Fabrication of macroporous Si membranes

As shown in fig.1.3, a macroporous Si membrane through which the gas can flow is needed for the realization of a PhC-based spectroscopic gas sensor. For this purpose the bulk Si remaining below the PECE pores has to be removed. Several approaches have been investigated in the framework of this thesis.

Conventional approach: wet etching using KOH/TMAH and SiO_2 passivation layer: The remaining Si below the macropores can be removed by wet etching from the wafer backside using

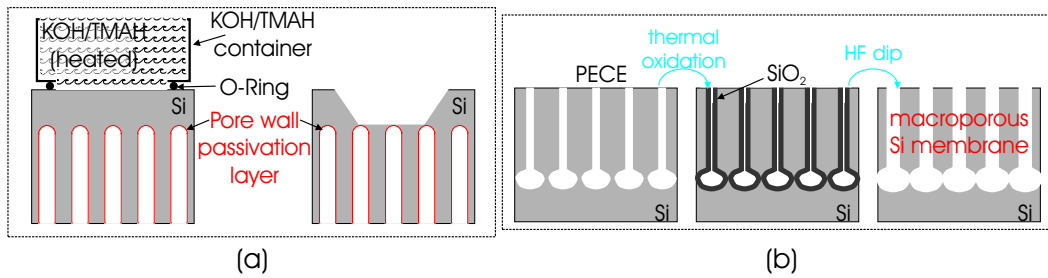


Figure 6.10: Post-PECE macroporous Si membrane fabrication methods. **a)** Conventional approach using wet etching from the backside and pore wall passivation layers. **b)** Membrane detachment by thermal SiO₂ growth and subsequent HF dip applied to pores that were widened during PECE at the bottom.

KOH, as depicted in fig.6.10a. To prevent the porous structure also being etched the pore walls have to be passivated by a KOH resistant layer. Typically a thermal oxide of 100-200 nm thickness is used. But the selectivity of KOH with respect to Si and SiO₂ is only on the order of 150-200:1 [49]. This makes large scale ($\approx\text{cm}^2$) fabrication of macroporous membranes a difficult task. To increase the selectivity and thereby the reproducibility of this process other wet etchants such as EDP or TMAH could be used. The etch contrast for Si and SiO₂ of TMAH (25% wt) at 60°C amounts to more than 15000. However, the Si etch rate of TMAH is about 2.5 times lower compared to KOH of the same concentration and temperature, resulting in increased fabrication time.

Wet etching using KOH/TMAH and alternative passivation layers: The disadvantage of some alternative wet etchants is their high toxicity and their complex handling compared to KOH. Therefore in this work the approach of alternative passivation layers was investigated. One possibility is to use SiN deposited by low pressure chemical vapor deposition (*LP-CVD*) which increases the etch contrast by almost a factor of 1000 [49]. Although it was possible to deposit about 50 nm thick SiN layers even in about 350 μm deep macropores and use it as etch stop, it turned out that SiN has strong absorption in the wavelength region of interest ($\approx 10 \mu\text{m}$). Another possibility is to infiltrate the pores by polymers that are KOH resistant using the wetting method developed by Steinhart et al. [85]. The drawback of this method is that the polymer layer is not completely closed so that KOH can penetrate through the polymer layer and etch away the pore walls.

Wet etching using HF and thermal oxidation: An alternative method for the fabrication of macroporous Si membranes is shown in fig.6.10b. The bottom part of the macropores is widened during PECE. Subsequent repetition of thermal oxide growth and HF-dip cycles leads to the connection of the widened bottom part of the pores and finally to the release of the membrane structure. The main advantage of this approach is that large scale ($\approx\text{cm}^2$) membrane formation can be achieved relatively well controlled. The widening of the pores during the oxide growth/HF-dip cycles has to be taken into account during PECE with respect to the desired pore diameter.

In-situ membrane fabrication during PECE: Within the framework of this thesis a third membrane fabrication method was developed. It allows *in-situ realization* of macroporous Si membranes and is depicted in fig.6.11. The porosity for a hexagonal array of macropores is given by (4.32). From this it follows that a porosity of 100% (corresponding to removal of all Si atoms in a certain

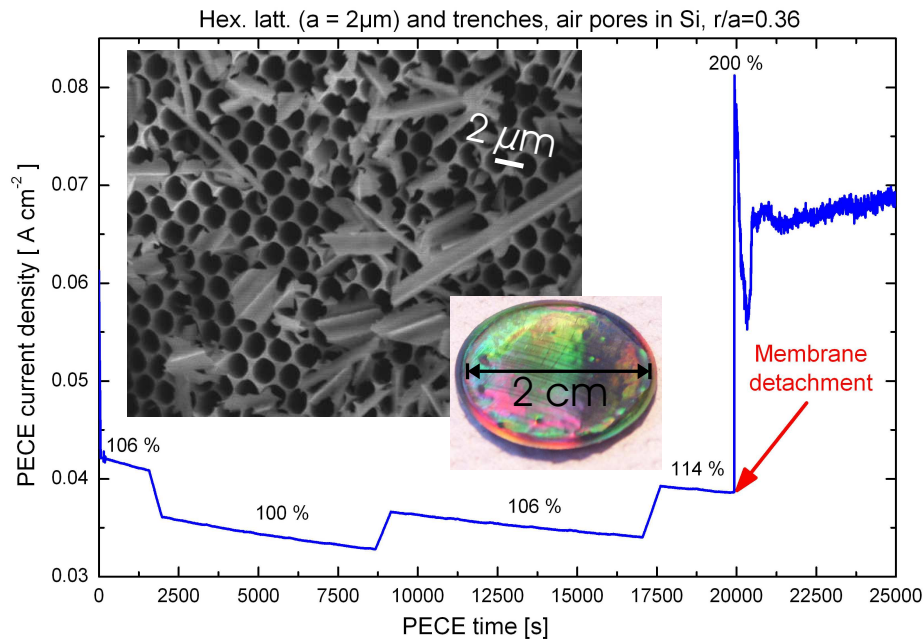


Figure 6.11: *In-situ macroporous Si membrane fabrication by drastically widening the pores during the last phase of PECE, shown here for pores with various diameter modulations (the numbers give the increase in pore diameter). The larger SEM inset shows the bottom of the porous membrane fabricated with this process. The smaller inset is a photograph of a membrane fabricated using this process.*

etch depth) is achieved for $r/a \geq 0.525$. By choosing the corresponding etch current density according to (4.30), overlap of neighboring macropores can be achieved and a macroporous Si membrane is formed. However, the PECE process is not in a stable regime for such extreme conditions. As a consequence the bottom part of the pores does not grow as nicely as in the stable PECE regime. This can be seen in the larger inset of fig.6.11 where an SEM micrograph of the bottom of a membrane fabricated in-situ at the end of PECE is shown. The pore ends are rather brittle and Si fragments cover parts of the membrane. They can be easily removed by mechanical treatment (e.g., scraping) and/or blowing with pressurized air or nitrogen. The smaller inset shows a photograph of a macroporous Si membrane with 2 cm diameter fabricated by this technique. This method offers the advantage, that no complex post-PECE process steps are necessary for membrane fabrication. Furthermore, large-scale ($\approx \text{cm}^2$) membrane fabrication is possible. For typical wafer sizes of 6 or 8 inch diameter, however, this method might not be applicable, since the necessary power supplies and illumination apparatus able to deliver the required high currents are no off-the-shelf components.

Chapter 7

Characterization of photonic crystal gas sensor structures

7.1 Characterization of the PECE ARL surface

Prior to optical PhC/ARL measurements, the quality of the PECE trenches and the ARL, respectively, was investigated using SEM and AFM as shown in fig.7.1. Already from the SEM micrographs taken at different etch depths an increase in roughness with etch depth can be seen. This increase is more pronounced for the thicker ARL. The AFM micrographs taken allow quantification of this observation. The average surface roughness¹ r_s of the upper part of the trench for the device with $t_{\text{ARL}} = 0.6a$ is rather smooth with a value of $r_s = 100$ nm. But with increasing growth depth, r_s increases reaching a value of $r_s = 165$ nm in about $350 \mu\text{m}$ depth. Taking into account that the surface roughness for low, tolerable scattering of incident light of wavelength λ at dielectric interfaces should be below $\approx \lambda/20$, the optical quality of the ARL achieved during the PECE should be sufficient for wavelengths around $\lambda \approx 10 \mu\text{m}$.

A closer look onto the SEM micrographs of the device with $t_{\text{ARL}} = 1.0a$ reveals the emergence of small holes with diameters on the order of 500 nm after a growth depth of about $30 \mu\text{m}$. As these holes do not show up in the device with $t_{\text{ARL}} = 0.6a$ it can be concluded that a transition between stable and unstable growth of PECE trenches next to macropores occurs if the ARL is chosen too thick. Both effects, the increase in r_s with growth depth and the instability of the PECE process for thick ARL layers, can be understood by looking at fig.7.2 where the equipotential surfaces for the PhC/ARL geometries used are schematically shown. When homogeneously distributed electronic holes created by illumination at the back of the Si wafer approach the growth front, they are focussed onto the pore tips and the bottom of the trench, respectively, by the gradient of the potential. In the case of the thick ARL with $t_{\text{ARL}} = 1a$, a region with only small potential gradient exists. Here only weak focussing of holes onto either the pore tips or the trench is achieved, resulting in an instable PECE process.

¹given as root-mean-square (*rms*) of the surface profile

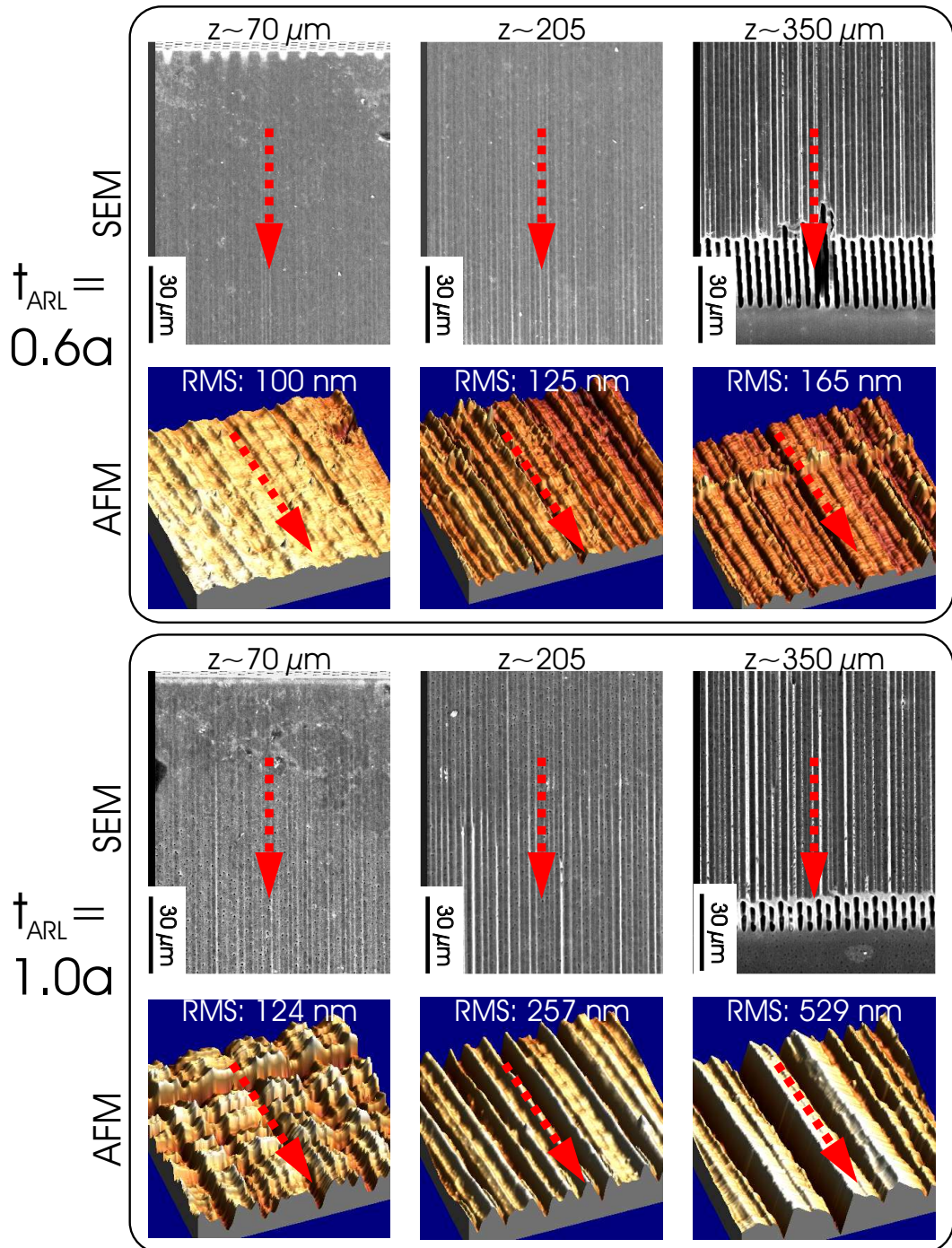


Figure 7.1: SEM and AFM micrographs of PECE ARLs with different thicknesses ($t_{\text{ARL}} \approx 0.6a$, $t_{\text{ARL}} \approx 1.0a$), taken at different growth depths z . Increase of surface roughness with increasing ARL thickness as well as growth depth can be observed. Red arrows mark the pore growth direction, i.e., the z -axis. The peaks/valleys perpendicular to the z -axis in the AFM micrographs are measurement artefacts due to external shock events and the very rugged part at the bottom of the pores is due to cleaving of the sample, i.e., these effects do not relate to the PECE. AFM performed on a $35 \times 35 \mu\text{m}^2$ area. ($r/a = 0.38$, $a = 4.2 \mu\text{m}$, $l_{\text{pore}} = 410 \mu\text{m}$)

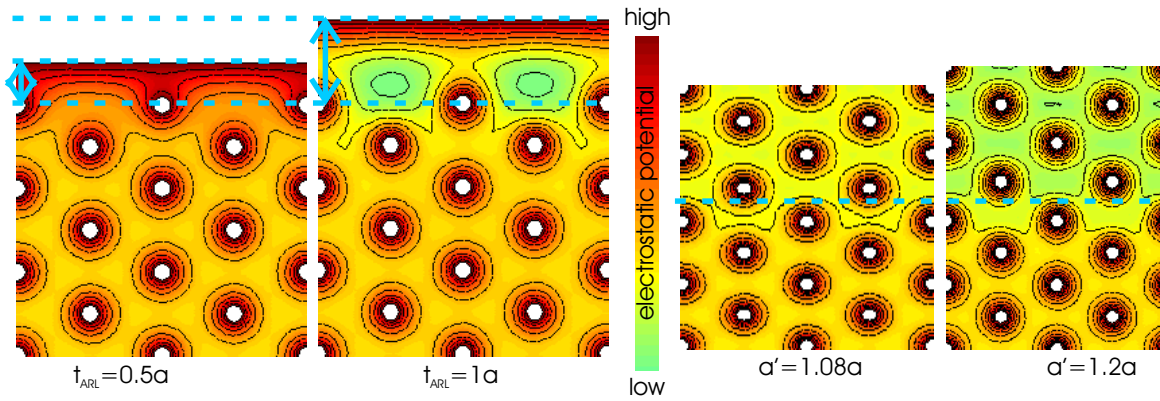


Figure 7.2: Left: equipotential surfaces for a regular hexagonal pore pattern and at a PhC ARL interface for two different ARL thicknesses during PECE. Right: equipotential surfaces in the interfacial regions of regular and distorted hexagonal lattice PhCs with distortions along ΓK of $f = a_y/a_x = 1.08$ and $f = 1.2$ (Dashed blue lines/arrows mark ARL thickness and interface position, respectively). The strong disturbance compared to the regular/distorted hexagonal lattice PhC interface at the PhC/ARL interface is clearly visible.

The increase in surface roughness of the ARL is a consequence of the disturbed potential distribution. At the beginning of pore growth the pore and trench locations are determined by lithography. But the asymmetric potential leads to a slightly inhomogeneous consumption of electronic holes. As a consequence, the pore/trench shapes and positions gradually change with increasing depth. In regions where the pores are close to the ARL, the latter will be a little thicker than designed while in regions where the pores are further away from the ARL, the ARL can consume more electronic holes during growth and therefore will become a little bit thinner than intended. That the pores next to the ARL influence the ARL's surface morphology is also confirmed by the observation that the lateral distance of the vertical stripes on the surface of the ARL is on the order of $\sqrt{3}a$, i.e., the lattice constant along ΓM direction.

This tendency to form a wavy, not perfectly flat surface with vertical texture was observed for all implemented ARL thicknesses $0.5a \leq t_{\text{ARL}} \leq 1.1a$, being more pronounced for thicker ARLs. Also changes in PECE parameters such as temperature $5^\circ\text{C} \leq T_{\text{HF}} \leq 13^\circ\text{C}$, electrolyte concentration $5\% \leq c_{\text{HF}} \leq 7\%$, applied external voltage $1.5 \text{ V} \leq V \leq 3.5 \text{ V}$, voltage ramps as well as anionic and non-ionic surfactant added to the HF electrolyte did not lead to a suppression of surface roughness.

From all these observations it can be concluded that the surface morphology of the ARL is related to its neighborhood, i.e., the pores next to it. To verify this, a series of parallel trenches could be implemented on a future lithography mask. PECE and subsequent investigation of these *comb* structures should reveal flat trench surfaces. To exclude the influence of crystallographic orientation of the trenches relative to the Si crystal axes, such comb structures should be implemented under several angles relative to, e.g., the Si [110] axis. Due to time and financial constraints such investigations could not be performed within the framework of this thesis. But looking at the reports of Barillaro et al. [81][82], influence of crystal orientation is unlikely and the surfaces of trenches in comb structures are flat, supporting the argument that the morphology of the *trenches next to pores* investigated in this work is due to the disturbed space charge region.

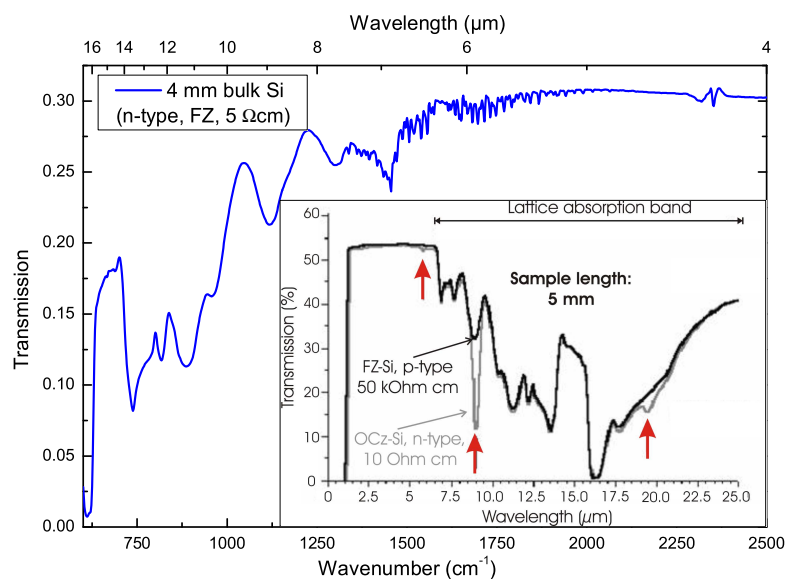


Figure 7.3: Absorption in bulk float zone Si (n-doping, 5 Ωcm) due to phonons (and oxygen). Inset: Transmission through 5 mm long bulk Si pieces with doping and resistivity given in the figure. The additional absorption peaks marked by the red arrows result from higher oxygen concentrations in the Cz-Si as compared to the FZ-Si (from: www.tydex.ru; OCz=Optical Czochralski, FZ=float zone)

7.2 Optical characterization of PhC gas sensor structures

7.2.1 Intrinsic macroporous Si absorption

The intended PhC-based spectroscopic gas sensor is based on the measurement of the reduced transmission through the PhC structure in case of presence of an absorbing gas. As a consequence, in spectral regions where the (macroporous) Si itself shows absorption, gas detection is not possible. While it is clear that Si as a semiconductor with a PhBG of 1.1 eV is strongly absorbing for wavelengths shorter than about 1.1 μm and is usually considered transparent in the NIR/MIR, some additional effects have to be taken into account. First, Si phonons are a possible source of unwanted absorption. Strong multiphonon absorption occurs at about 1118 cm^{-1} with a FWHM of about 50 cm^{-1} (300 K) due to two transverse optic and one transverse acoustic phonon. This is close to the ethanol absorption line at 1060 cm^{-1} and might reduce the performance of a PhC-based ethanol sensor, and is depicted in fig.7.4. While this Si phonon absorption is strong and therefore well known, Si exhibits many more, weaker phonon absorption peaks that play an important role only when considering transmission through thick ($\geq 5\text{ mm}$) Si pieces. This is shown in fig.7.3, where the transmission through a 4 mm long, bulk n-Si piece was measured by IR spectroscopy. The piece originates from a prestructured Si wafer normally used for PECE of macroporous Si PhCs. For wavelengths longer than about $6.5\ \mu\text{m}$ transmission is strongly reduced by phonon absorption, especially at wavelengths around $6.9\ \mu\text{m}$, $7.7\ \mu\text{m}$, $9\ \mu\text{m}$, $11.4\ \mu\text{m}$, $12.3\ \mu\text{m}$ and $13.6\ \mu\text{m}$. Hence, a macroporous Si-based spectroscopic gas sensor is not suitable for detection of gases having absorption lines close to the above wavelengths. However, for shorter

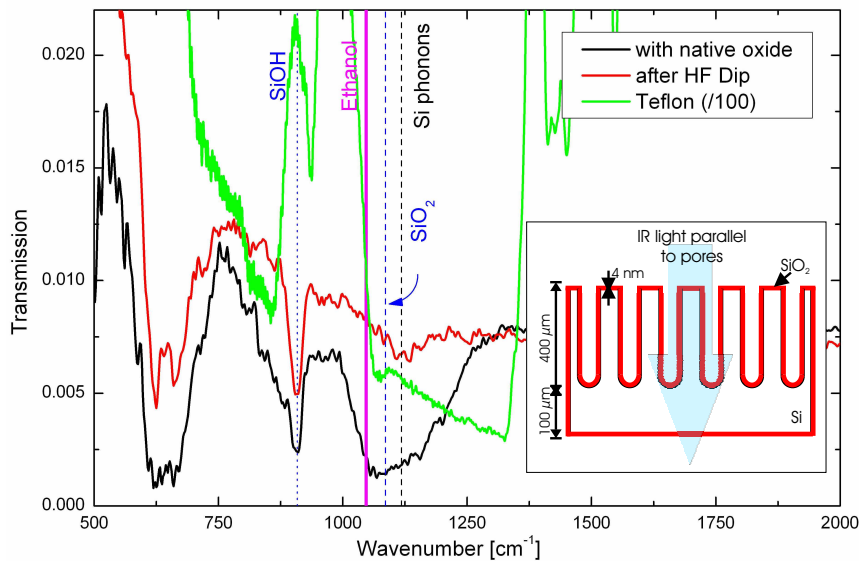


Figure 7.4: Absorption in macroporous Si due to oxides on the surface and phonons. Teflon is an attractive pore wall coating material since it shows much higher transmission in the spectral range of interest. The inset shows configuration used for the IR transmission measurement. (Measurement in parts by D. Pergande, Univ. Paderborn)

wavelengths than $6.5 \mu\text{m}$ macroporous Si PhCs are well suited for gas detection.

Second, effects due to the increased surface area of a macroporous Si sample as compared to a bulk Si piece have to be considered. An *ideal* Si surface is hydrogen (*H*) terminated. This may not necessarily be true for macroporous Si samples after PECE due to, e.g., influences of the surfactant added to the electrolyte. In addition, when stored in air, a native oxide begins to grow on the Si surface. In fig.7.4 it can be seen that the absorption due to SiO_2 is spectrally close to the absorption line of ethanol. This absorption can be reduced by an HF dip, so a PhC-based ethanol sensor is still feasible if the pore walls are, e.g., covered with passivating layers that prevent the formation of native oxide. For pores with a depth of several hundred μm , IR transmission measurements along the pores showed that the time necessary to remove the native oxide from the pore walls is on the order of several hours. Typically the samples were exposed to HF with a concentration of 5-10%(wt.) for 8-12 hours. This is in strong contrast to macropores with a depth of only about $100 \mu\text{m}$ where a HF dip of typically 10-30 minutes is sufficient to remove the native oxide from the pore walls for pores with comparable diameters. Another important issue for transmission measurements through macroporous structures is the residues that might remain in the pores after taking the macroporous samples out of the HF. Simple drying using a nitrogen gun only removes the superficial liquids. Transmission measurements through such structures exhibit strong absorption features due to, e.g., water. Our experiments showed that heating of the samples at about $100\text{-}150^\circ\text{C}$ for 2 min is sufficient to remove the aqueous residues from the pores. However, water vapor in the surrounding air tends to condense back into the pores. As a consequence, an HF dip followed by an annealing step is therefore strongly recommended right before IR measurements of the macroporous structures to yield meaningful results. The HF

dip shows a much weaker influence on the Si-OH absorption line. This is not an critical issue, however, because it lies far enough away from the ethanol absorption.

An attractive material for coating of the pore walls is Teflon since it is chemically inert, can withstand temperatures of more than 100°C and could be infiltrated using the wetting process developed by Steinhart et al.[85]. The transmission through a 550 μm thick Teflon foil (divided by a factor of 100 for scaling reasons) is shown in fig.7.4 in green.

The strong impact of the increased surface area of the macroporous Si can be estimated from fig.7.4. Taking the parameters of the sample measured in fig.7.4 (hexagonal lattice, $a = 4.2 \mu\text{m}$, $r/a = 0.385$, 4 nm native oxide thickness on each pore Si surface) it follows that in the transmission measurement parallel to the pores the native oxide covers about 0.5% of the unit cell (and hence the total sample) area. Taking into account the pore depth of 400 μm this corresponds to transmission through bulk native oxide with a thickness of about 2 μm . In the case of transmission perpendicular to the pores along the ΓK direction through the intended PhC interaction volume of about 1 cm length, light has to travel through about 20 μm native oxide. From the exponential decrease of transmission following from Lambert's law it is obvious that no light would reach the far end of the PhC gas sensor interaction volume. As a consequence, native oxide on the pore walls has to be avoided to achieve a functional macroporous Si ethanol gas sensor.

7.2.2 PhC structures without taper

Since in the beginning of this work only standard samples, i.e., samples without any taper, were available, first optical experiments were performed on conventionally cleaved PhCs. Despite the difficulty to achieve *two, parallel* cleaving edges, *only a few mm apart* routinely, the sample under investigation showed coupling interfaces to promise successful transmission measurements. To avoid absorption due to oxides (1085 cm^{-1}) close to the QCL wavelength (976 cm^{-1}) an HF dip before the experiment is mandatory². To further increase the chance of measuring transmission through the 5 mm long sample (in ΓK direction), an $r/a = 0.345$ was chosen. For this porosity the QCL emission lies in the steep part of the band intended to be used for gas sensing and not in the flat, low v_g part. The pore depth was on the order of 380 μm , leaving a 145 μm thick bulk Si substrate below. With the pinholes and focussing mirrors of the QCL setup described in 4.2.2.2 the beam coming from the QCL could be well focussed onto the center of the macropore region. To determine the transmission, first the coupling losses have been estimated, based on transmission/reflection measurement through the Si substrate below the pores. The transmission and reflection through the bulk Si substrate were measured to be 15% and 20%, respectively. These values are much lower than the theoretically expected values based on Fresnel's equations of 55% and 45%, respectively, and are a consequence of roughness of the cleaving edge and screening effects of the pinholes. The loss due to coupling can therefore be estimated to be about 55% (or 3.5 dB) for the reflected light. In the following the same coupling loss is assumed for light transmitted through the porous region. Now, transmission through the macroporous PhC was measured and found to be 0.1% as shown in fig.7.5. After annealing the sample for 30 s to 350° and measuring the transmission again, the latter was determined to be 0.3%. The increase in transmission is due to desorption and driving out of aqueous residues from the pores. From the above values the loss in the PhC region can be estimated to be on the order of 3.7 dB/mm.

²Strong oxide absorption will reappear after several hours of storage in air[49].

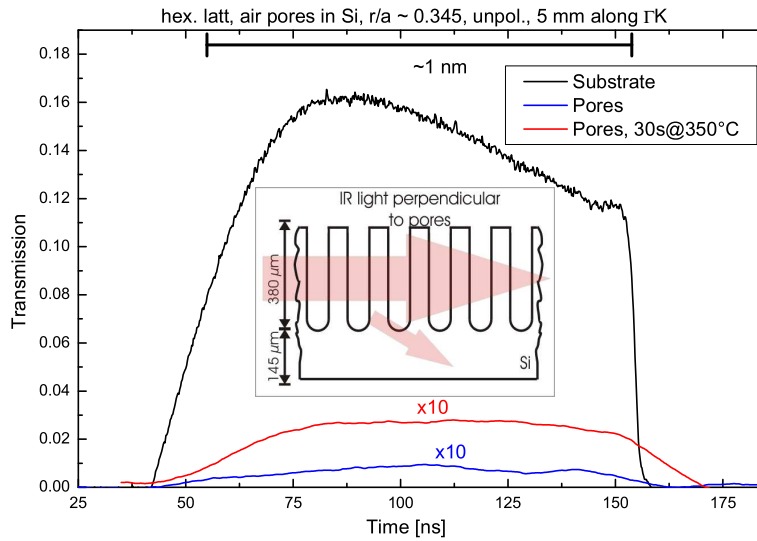


Figure 7.5: Transmission through conventionally terminated PhC using a QCL. The pore depth was measured to be 380 μm (below pores: 145 μm bulk Si substrate).

However, it has to be taken into account that this large value does not only describe the true losses due to the PhC, but also accounts for the light lost to the substrate. In several experiments it was found, that light coupled to the porous PhC region tends to leak into the substrate and is therefore lost for detection at the output side of the PhC in the porous region. This could be quantified by comparing this experiment with transmission through a comparable *membrane* PhC. Unfortunately, such a sample could not be successfully prepared during this work.

7.2.3 Adiabatic PhC Taper

Although the adiabatic PhC taper concept developed in 5.4.1 using PhBS calculations and physical intuition later turned out in FDTD simulations not to increase the transmission through a PhC, its optical properties can still be explored by reflection measurements. The working principle underlying adiabatic PhC taper is based on distortion of a regular hexagonal lattice. FTIR reflection measurements on a macroporous Si sample with air pores arranged in a distorted hexagonal lattice (distortion 21%) are shown in fig.7.6. The measured spectral position of the first two PhBGs reasonably well matches the calculated normalized frequencies. Furthermore, the high reflection resulting from non-coupling bands is clearly visible, indicating the good quality of the sample.

7.2.4 Optical properties of ARL PhC structures

7.2.4.1 PhC with ARL: IR reflectance

In 5.4.2 a concept entitled *ARL* was developed to increase transmission through PhC structures even in spectral regions where the bands are flat. This is achieved by increasing the coupling

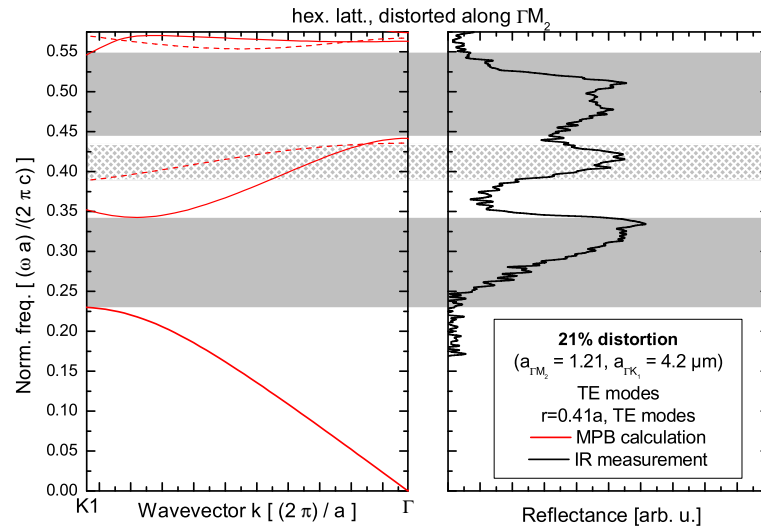


Figure 7.6: Optical characterization of a macroporous Si PhC. The air pores are arranged in a distorted hexagonal lattice with 21% distortion along the ΓM_2 direction. High reflection in the spectral regions of the first two PhBGs as well as the non-coupling band (dashed lines) is clearly visible. (Note the MCT detector cutoff frequency of $\approx 600 \text{ cm}^{-1}$ corresponding to $a/\lambda \approx 0.25$.)

efficiency of plane waves impinging on the PhC interface to the desired PhC modes by utilizing a surface mode in the ARL. This increase in coupling efficiency leads to a decrease in reflection for that specific wavelength. In fig.7.7 the reflectance for a macroporous Si PhC with a conventional, i.e., corrugated air/PhC interface and an ARL interface is presented. The left graph shows the results of FDTD calculations, the right graph depicts the results obtained by IR reflection measurements. Introduction of the ARL layer leads to dips in the reflectance spectrum at 809 cm^{-1} and 1008 cm^{-1} as a result of newly created surface modes. The interesting feature here is the reduction in reflectance at the air band edge since this is the low v_g mode intended to be used for gas detection. One could now speculate that introduction of the ARL simply shifts the whole PhBS towards longer wavelengths. As a result, the frequency intended to be used for gas detection would no longer lie at the edge of the air band but above. This would also lead to a reduced reflectance. The advent of the reduced reflectance at 809 cm^{-1} contradicts this hypothesis since no comparable feature is seen neither in the FDTD calculation nor in the IR experiment for the conventionally terminated PhC. Another remarkable feature is the fact that for the ARL terminated sample reflectance dips *within* the PhBG appear. This is also a typical surface state related feature reported for non-conventionally terminated PhCs [5]. The modes created as a result of disturbance of the ideal PhC symmetry cannot couple to air due to the dielectric contrast at the air/ARL interface and they can also not escape into the PhC due the broad PhBG of the ideal PhC. As a result defect states within the PhBG are created and the surface states are localized within the ARL.

In addition to IR reflection, ARL samples were also characterized using IR transmission. Both, broadband IR measurements using an FTIR microscope as well as narrow bandwidth spectral

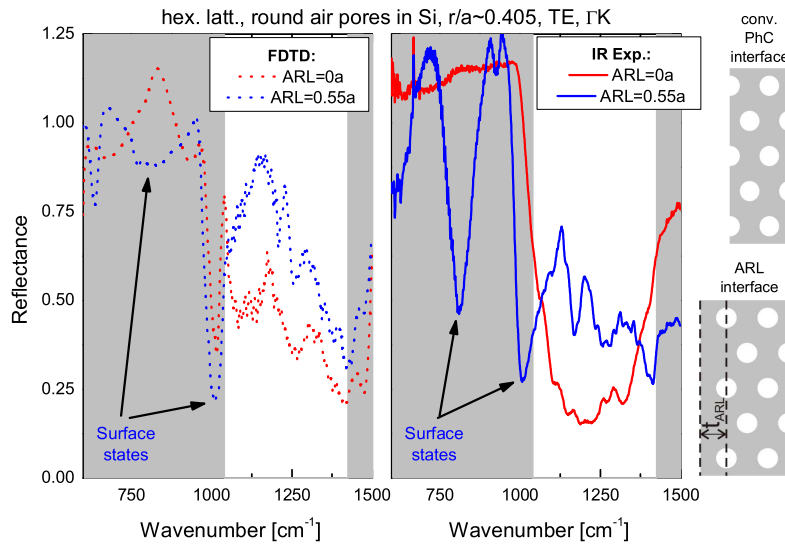


Figure 7.7: Optical characterization of a macroporous Si PhC with incorporated ARL. The ARL was realized in-situ during PECE. Left: reflectance using FDTD simulations. Right: measured reflectance using an FTIR microscope. The inset on the far right shows the different interfaces considered. The grey regions mark the position of PhBGs for TE polarization.

characterization using a QCL have been performed.

7.2.4.2 PhC with ARL: QCL transmission

Fig.7.8 shows the transmission measured through a thin macroporous Si sample with a QCL ($\lambda_{\text{QCL}} = 4.46 \mu\text{m}$). The sample was a membrane structure with a pore height of about $380 \mu\text{m}$. To avoid light passing by on any side of the sample, it was mounted on a pinhole with diameter of $100 \mu\text{m}$. The transmission through that pinhole without a sample mounted to it served as reference signal and is plotted as a solid black line in fig.7.8. The y -axis states the detector signal (in V). The x -axis is given in time units. This is due to the fact that spectral tuning of the QCL is achieved by the temperature change while the QCL is heated during the applied power-on pulse. For this QCL the time span of about 250 ns corresponds to a shift of the spectral emission of about 1 nm, i.e., a true narrow band experiment is performed here. The peak transmission for TE and TM polarization, normalized to the reference signal, are 17% and 7%, respectively, corresponding to losses of 96 dB/mm and 144 dB/mm, respectively. Qualitatively this agrees well with the reflection of this sample (inset in fig.7.8) measured with an FTIR microscope. At the position of the QCL line the reflection for the TM polarization is higher than for the TE polarization. The high values for the losses are a consequence of the fact that the transmission was measured in the extreme high frequency range of $a/\lambda = 0.94$. In addition to coupling losses at the air/ARL interfaces³ and losses due to PhC structure imperfections, coupling of light from the PhC to air modes is very possible since the operating frequency lies far above the light line of the PhC. While

³With the setup used for this experiment it was not possible to determine the reflection at the air/ARL interface. Therefore no estimation of the coupling loss can be given.

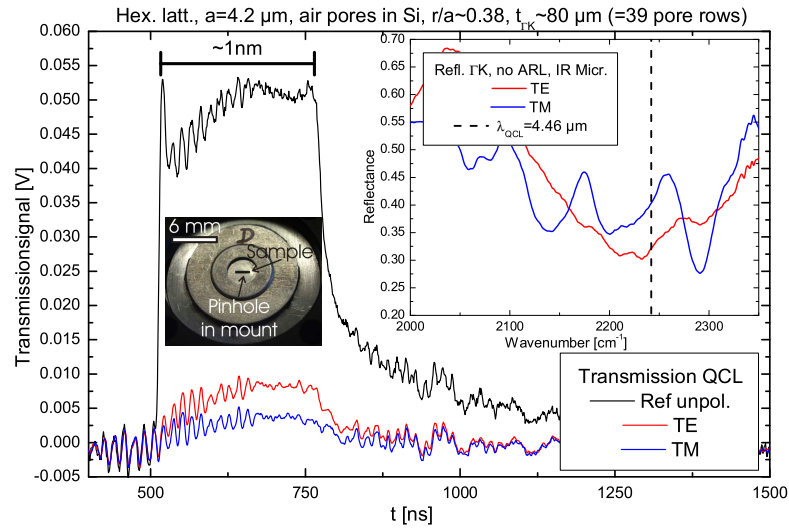


Figure 7.8: IR transmission measured along ΓK using a QCL with $\lambda_{\text{QCL}} = 4.46 \mu\text{m}$. The sample (membrane with height $380 \mu\text{m}$, width $\approx 2 \text{ mm}$), about $80 \mu\text{m}$ thick along ΓK (=transmission) direction with an ARL of thickness $t_{\text{ARL}} \approx 0.55a$, (corresponding to 39 pore rows, $a = 4.2 \mu\text{m}$) was put on a pinhole (diameter $100 \mu\text{m}$). The inset graph shows IR reflection performed on the same sample using the FTIR microscope. The inset photograph shows the sample mounted on the pinhole.

these losses to air modes probably contribute most to the total loss, this loss channel is not existing for modes lying below the light cone, such as the modes intended to be used for gas detection.

7.2.4.3 PhC with ARL: IR transmission

Broadband transmission measurements were performed using an IR microscope connected to an FTIR spectrometer. Since spectrally resolved, broadband IR transmission through long (≥ 1000 pore rows/unit cells) PhCs has not been demonstrated in the macroporous Si material system up to now⁴ PhC samples with ARL having different thickness along the (ΓK) transmission direction were fabricated by PECE. Figs.7.9 and 7.10 compare the reflection and transmission through macroporous Si membranes with pore depths of about $380 \mu\text{m}$. Transmission was measured by mounting the PhC sample (about 2 mm wide) on a pinhole with $100 \mu\text{m}$ diameter to ensure all of the detected light passed the macroporous sample. Both, the reflectance as well as the transmission spectra clearly show the onset of the PhBG at about 1050 cm^{-1} (black arrow in figs.7.9 and 7.10). Furthermore, for almost each dip in reflectance a peak in transmission can be found (grey arrows in figs.7.9 and 7.10). Their relative shift is due to sample inhomogeneities since the measurement spots for transmission and reflectance have not been the same.

In the fundamental band the mode profile of the corresponding Bloch mode is very similar to a plane wave for TE as well as TM polarization. In addition, the slope of the TE and TM bands

⁴to the author's best knowledge

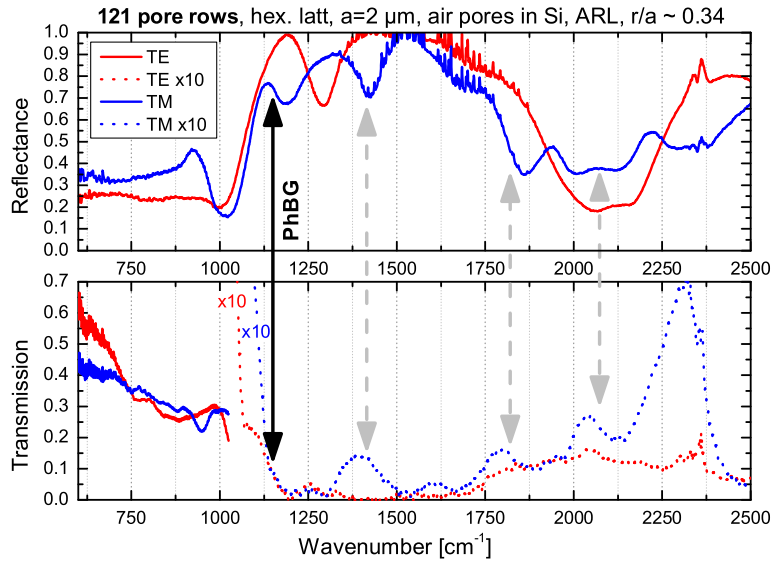


Figure 7.9: Reflectance (top) and transmission (bottom) for TE and TM polarization, respectively, for a macroporous Si sample having 121 pore rows along ΓK direction and ARL with nominal thickness $t_{\text{ARL}} = 0.58a$. The onset of the PhBG is clearly visible (black arrow). Spectral regions of high transmission correspond to low reflection and vice versa (grey arrows). The slight spectral misfit results from sample inhomogeneities, i.e., the spot used for transmission measurements was different from the spot used for reflection measurements.

is comparable ($\Delta n_{\text{eff}}^{\text{TE, TM}} \approx 0.2$). As a result one would expect comparable transmission. The observed difference in transmission is probably due to sample imperfections or effects of the ARL. In the long wavelength limit the transmission is on the order of about 40% for the shorter sample with 121 pore rows and about 30% for the longer sample (249 pore rows). This corresponds to losses of about 66 dB/mm and 88 dB/mm.

While a dip in reflectance in the spectral region of the PhBG can be explained by surface states due to the ARL, the observed transmission at about 1400 cm⁻¹ is not evident, since there are no photonic bands that enable transmission within the PhBG. The reason for the observed effect might be overlap of the surface modes at the two ARL interfaces. As can be seen in fig.5.14, ARL/PhC surface mode spatially extends over several pore rows into the PhC structure. For short structures this can lead to direct coupling of the two surface modes at opposite interfaces without any mediating photonic bands. For higher frequencies beyond the fundamental PhBG the transmission through the longer sample is about one order of magnitude smaller compared to the transmission through the short sample ($\approx 3\%$), corresponding to huge losses of about 255 dB/mm for the short sample. There are two possible reasons. Higher frequencies are closer to the light cone. Therefore, the loss increases drastically with sample length.

Another source of loss, to which higher frequencies are more sensitive, is surface roughness. Although from SEM and AFM images the surface roughness can be estimated to be on the order of 10-40 nm and therefore small compared to the wavelength used (several μm), it might still be a source of Rayleigh scattering. And since Rayleigh scattering scales with the fourth power of

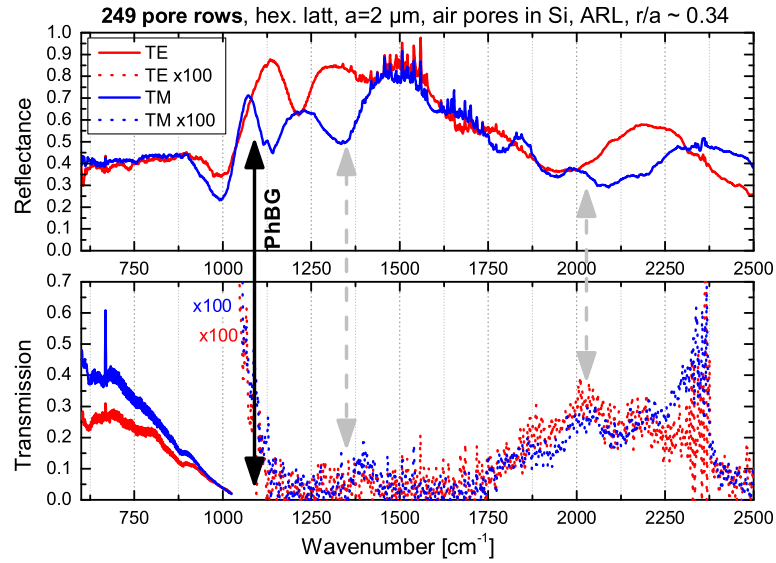


Figure 7.10: Reflectance (top) and transmission (bottom) for TE and TM polarization, respectively, for a macroporous Si sample having 249 pore rows along ΓK direction and ARL with nominal thickness $t_{\text{ARL}} = 0.58a$. The onset of the PhBG is clearly visible (black arrow). Spectral regions of high transmission correspond to low reflection and vice versa (grey arrows). The slight spectral misfit results from sample inhomogeneities, i.e., the spot used for transmission measurements was different from the spot used for reflection measurements.

the light frequency, loss increases drastically for higher frequencies. Fig.7.11 shows the calculated transmission as a function of the number of pore rows. For the transmission an exponential decay of the form $T = T_0 \exp(-\alpha_s N_{\text{PR}})$ is assumed where α_s is the scattering loss per pore row and N_{PR} is the number of pore rows. For losses of 1% per pore row, the transmission signal is reduced to 50% and 10%, respectively, after only 70 and 227 pore rows, respectively. Assuming $\alpha_s = 0.1\%$, 3 dB and 10 dB damping are reached after 691 and 2300 pore rows, respectively. From this approximation follows, that it should be possible to measure transmission through macroporous Si PhC structures of the intended length of about 1 cm (corresponding to 2380 pore rows along ΓK with $a = 4.2 \mu\text{m}$) - presumed scattering is the only source of loss and $\alpha_s \leq 0.1\%$ for the frequency of interest.

From the transmission measurements shown in figs.7.9 and 7.10, α_s for some frequencies can be estimated. For the three frequencies given in tab.7.1, the average of the transmission measured for TE and TM polarization was calculated⁵. Assuming exponential decay of the transmitted intensity according to $T_{121 \text{ PR}} = T_0 \exp(-121\alpha_s)$ and $T_{249 \text{ PR}} = T_0 \exp(-249\alpha_s)$, the scattering loss per pore row α_s was calculated and is also given in tab.7.1.

Close to the long wavelength limit (625 cm^{-1}) where λ is 8 times larger than the lattice pitch ($2 \mu\text{m}$), the situation resembles transmission through bulk Si. From Fresnel's equations the expected transmission is $T \approx 50\%$. This is close to the measured value of 48% for the shorter

⁵The transmission for the frequencies considered were comparable for the TE and TM polarizations. Therefore the average transmission was used.

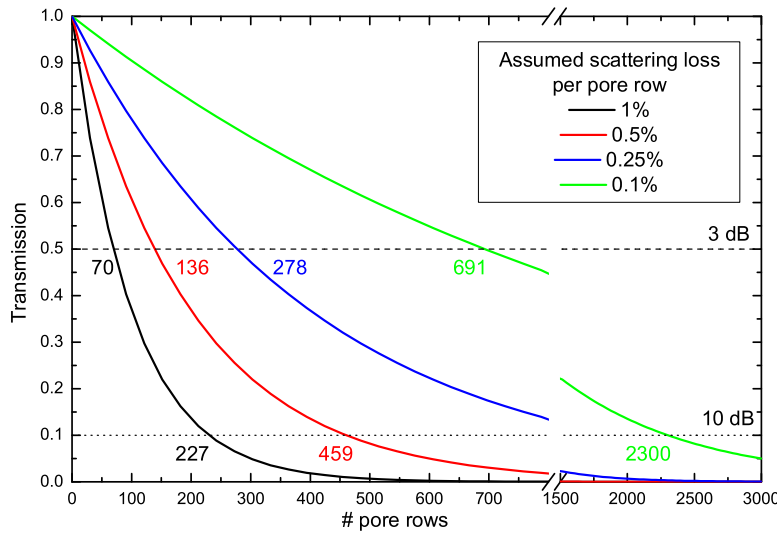


Figure 7.11: Transmission as a function of the number of pore rows for different values of scattering loss per pore row. The horizontal black dashed and dotted lines represent 3 dB and 10 dB attenuation, respectively. The colored numbers show after how many pore rows the corresponding attenuation is reached.

sample. The measured transmission of only 32% through the longer sample, however, indicates that the long wavelength approximation is not totally valid, i.e., the porous structure has a significant influence on the transmission. Since the dispersion in this frequency range is not heavily influenced by PhC bandstructure effects, it can be concluded that the influence on the transmission originates from the pores itself, e.g., the pore wall roughness, and not from their periodic arrangement. Below the first PhBG (625 cm^{-1} and 750 cm^{-1}), α_s is on the order of a few tenths of a percent. In the spectral region of the PhC-based gas sensor at about 2000 cm^{-1} , the parameter describing the scattering loss is found to be $\alpha_s = 1.3\%$ from the data in figs.7.9 and 7.10. It has to be taken into account, however, that for such high frequencies PhBS effects also play an important role concerning transmission and reflection. Studies dealing with the influence of surface roughness are currently being performed. Fig.7.12a shows a rather rough surface of a macropore after PECE. Such a high roughness is a consequence of non-optimal PECE parameters

	Transmission at		
	625 cm^{-1}	750 cm^{-1}	2000 cm^{-1}
121 pore rows	$(48.0 \pm 5)\%$	$(35.0 \pm 5)\%$	$(1.6 \pm 0.5)\%$
249 pore rows	$(32.0 \pm 5)\%$	$(27.5 \pm 5)\%$	$(0.3 \pm 0.5)\%$
α_s	$(0.3 \pm 0.04)\%$	$(0.2 \pm 0.03)\%$	$(1.3 \pm 1.1)\%$

Table 7.1: Scattering loss per pore row derived from the data in figs.7.9 and 7.10. The averaged transmission $(T_{TE} + T_{TM})/2$ of both polarizations was used and scattering is assumed to be the only source of loss.

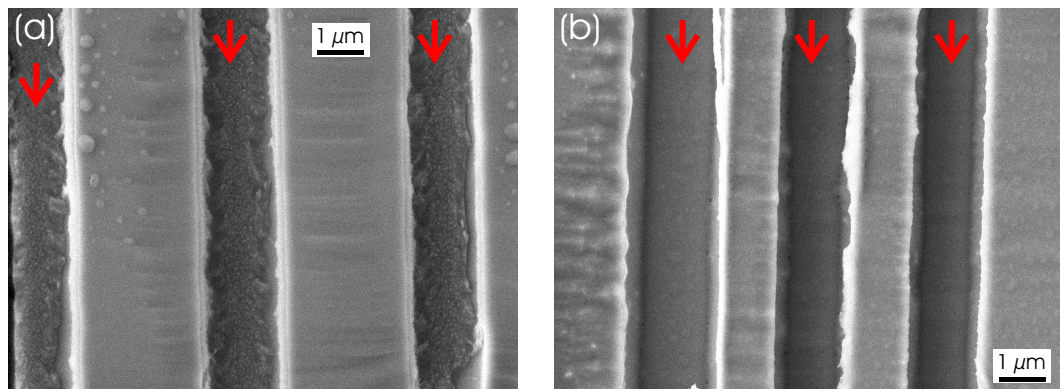


Figure 7.12: **a)** Rough pore walls of PECE macropores. **b)** Smoothened pore walls after KOH (5% wt) dip (15 min). Red arrows mark the pores.

as well as the used surfactant⁶. However, the roughness can be reduced by appropriate post-PECE treatment such as, e.g., a KOH dip, as shown in fig.7.12b. In principle it should be possible to achieve atomically flat surfaces by choice of appropriate surface treatment. Currently several wet etchants including diluted hydroxides such as NaOH, KOH, combinations of alcohols and HF as well as organic species are investigated.

At this point the determination of the exact r/a -ratio of PhC structures *with* ARL should be discussed as it is not straightforward. Usually the porosity of the PECE sample can be obtained by comparing reflectance/transmission spectra of bulk PhCs with numerical simulations of the PhBS. Introduction of the ARL however leads to numerous and strong modifications of the PhC spectra. In addition, now not only the r/a -ratio determines the PhC's spectrum but also the thickness of the ARL. Therefore, a wide parameter space exists that aggravates the exact determination of the characteristic parameters of the sample. The values given in this work usually are based on information gathered from various sources such as optical characterization, SEM and nominal PECE parameters. Currently different strategies concerning the characterization of PhCs with ARL are discussed within our group. One possibility probably consists in getting the samples r/a -ratio from transmission measurements parallel to the pores. After this parameter is fixed, the actual ARL thickness could be determined by comparing the measured spectra to numerical simulations. A second approach concerns the incorporation of marker/reference structure into each PhC with ARL device. The r/a -ratio could also be derived from the resonance frequency of, e.g., an incorporated point defect, somewhere at a boundary of the PhC gas sensor structure⁷.

⁶Using other surfactants and optimized PECE conditions the pore wall roughness is typically much lower. The high roughness shown here was chosen for instructive reasons.

⁷Cleaving of the macroporous sample and determination of the spectral properties at such a conventional interface seem to be the most straightforward approach. However, as discussed before, cleaving of deep macropore arrays usually leads to very rough coupling edges and as a consequence insufficient measurement signals.

Chapter 8

PhC gas sensor: device integration

The macroporous Si PhC studied in the previous sections is supposed to replace the conventional interaction volume in a spectroscopic gas sensor. The integration of such a macroporous Si PhC in an actual device is discussed in this section. From fig.1.3 the topics to be addressed are obvious. First, a suitable light source has to be chosen. Next, efficient coupling of light to and from the PhC has to be realized. The outgoing radiation has finally to be measured by an appropriate detector.

8.1 Choice of the IR light source

For the intended spectral operating range (NIR/MIR) several kinds of light sources are conceivable. The source with the highest spectral output power and the narrowest line width to date is a QCL. In addition, the radiation leaving a QCL is spatially narrow and already polarized. However, due to its sophisticated design and fabrication (epitaxy of several hundred layers with exact composition and thickness), a QCL is by far too expensive (\gtrsim several 10,000 US\$ per device) for application in widely used sensor systems. Furthermore, due to its narrow line width, the use of a QCL imposes rather stringent requirements to be met by the PhC structure, thereby limiting fabrication tolerances. Usage of an LED would reduce this constraint to some extent. But the emitted spectral power of an LED is significantly smaller than that of a QCL leading to an inferior signal to noise ratio. For the realization of cheap sensor systems a simple thermal emitter with a spectrum similar to a black body is the most likely choice for a light source. However, the spectral output power is rather small. The emitted radiation is not polarized. This necessitates the use of polarizers in a PhC gas sensor device since the PhC interaction volume is designed to work at a specific wavelength and for a specific polarization. While such a polarizer decreases the usable spectral power further, the light with the other polarization could be used as a reference signal.

8.2 Coupling of radiation to and from the PhC

Since the most likely kind of light source to be used in a PhC based spectroscopic gas sensor is a thermal emitter, one challenge is to couple its rather divergent light to the PhC. This is especially tricky because the size of the coupling interface is on the order of 10 mm wide and

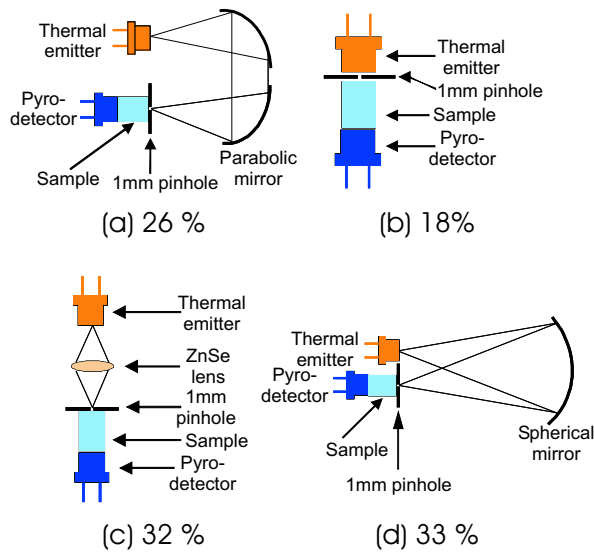


Figure 8.1: Device integration: various schemes investigated concerning the coupling of thermal emitter, PhC and detector. The numbers below the figures give the transmission measured through bulk Si pieces of about $1 \times 1 \times 0.5 \text{ cm}^3$ size. (Simulations performed at FhG IPM, Freiburg)

only 300-450 μm high. Several focussing setups have been simulated and some are shown in fig.8.1 together with measured transmission through bulk Si pieces. The maximum transmission achieved was on the order of 30% using a lens and mirrors, respectively (fig.8.1c and d). However, due to its simplicity and the still reasonable transmission of 18%, direct coupling of light leaving the thermal emitter in close vicinity to the PhC and collecting the light right after the PhC as shown in fig.8.1b is also an interesting design scheme.

8.3 Device dicing: realization of optically high grade interfaces

To use a PhC as the interaction volume in a spectroscopic gas sensor, light impinging from air has to be coupled to certain Bloch modes in the PhC. This coupling takes place at the air/PhC interfaces. Because the equipment necessary for the microstructuring process of macroporous Si structures developed by Ottow et al.[78] that would in principle also have allowed the fabrication of appropriate air/PhC interfaces was no longer available, various other fabrication strategies for the realization of conventional as well as ARL interfaces have been investigated and are discussed in the following.

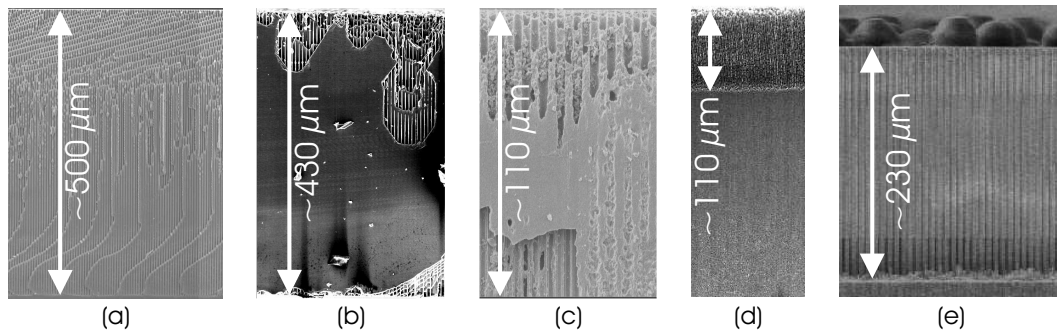


Figure 8.2: SEM micrographs of Air/PhC interfaces obtained by different dicing techniques. (a) Cleaving of deep macropores, (b) sawing using a rotating diamond disc, (c), (d) cutting using a fs laser and (e) RIE/ICP.

8.3.1 Cleaving

Typically an air/PhC interface as shown in fig.5.7a is realized by inscribing the PECE macroporous Si sample along a high symmetry direction like ΓK or ΓM with a diamond scribe for a few mm and subsequent cleaving using, e.g., tweezers.

This procedure works fine if the ratio of the length of the pores l_{pore} to the thickness of the remaining bulk Si under the pores $t_{\text{Wafer}} - l_{\text{pore}}$ fulfills $l_{\text{pore}}/(t_{\text{Wafer}} - l_{\text{pore}}) \lesssim 1/4$, i.e., pores with a length of about $100 \mu\text{m}$ in a approximately $500 \mu\text{m}$ thick wafer. In this case the Si crystal lattice underneath the macropores guides the rupture along the $[110]$ direction. Because during lithography the high symmetry directions of the PhC have been chosen to be parallel to the $[110]$ direction, together this leads to a cleaving edge running through the region of highest porosity, i.e., the center of the macropores, along a high symmetry direction.

However, if the ratio $l_{\text{pore}}/(t_{\text{Wafer}} - l_{\text{pore}}) \gtrsim 0.5$, the above procedure usually leads to very rough and arbitrarily rugged surfaces as shown in fig.8.2a. In this case the high symmetry directions of the highly porous PhC structure compete with the relatively thin bulk Si region below the pores in guiding the rupture. Usually this results in rough surfaces leading to a high amount of scattering of the incoming light and therefore a bad coupling at the air/PhC interface as shown in fig.8.2a.

8.3.2 Sawing

A widely used method to separate, e.g., different electronic devices fabricated on a Si wafer is sawing using a rotating disc whose cutting edge is tipped with diamond pieces. While this is a suitable technique for cutting through bulk materials, it reaches its limits when applied to porous materials. The jittery rotation of the disc leads to an irregular break away of the pores as shown in fig.8.2b. Furthermore, the precise alignment of the rotating disc relative to the intended cut imposes a challenge. Based on the ARL design developed in section 5.4.2 resulting in a optimal thickness of the bulk Si forming the ARL of about 700 nm for a hexagonal lattice with $a = 4.2 \mu\text{m}$ and $500 \mu\text{m}$ deep pores, a vertical tilt of less than 0.1° leads to the desired ARL thickness at the top of the pores but to 0 nm thickness at the bottom of the pores, i.e., the ARL is non-existing in this region. Another practical problem consists in the lateral precision achievable with typically used disc saws which lies in the range of μm . However from numerical simulations it follows that the ARL thickness has to be precise within $\pm 200 \text{ nm}$.

8.3.3 Laser cutting

Cutting of various materials using high power lasers, e.g., CO_2 -lasers in mechanical engineering to cut through metals, is nowadays a well established technique. Due to the high power applied to the material high amounts of thermally induced mechanical stress build up along the cutting edge. Application of this technique to macroporous Si structures would therefore lead to a rough, optically low grade air/PhC interface due to destruction of the pores along the cut resulting from high, thermally induced, stress.

To avoid build up of thermal stress the feasibility of cutting using a femto second laser was investigated. A Ti:Sapphire laser system with an emission power between $70\text{-}150 \text{ mW}$ at 780 nm wavelength with pulse durations ranging from $50\text{-}150 \text{ fs}$ and 1 kHz repetition frequency was used to cut both bulk Si as well as macroporous Si samples. The laser beam was focused onto the

sample using a microscope objective and the sample was mounted onto an x - y - z - Θ stage below the objective, allowing lateral drive velocities between 0.5-1 mm per minute¹.

While bulk, i.e., non-porous Si can be laser cut with flat, shiny, optically high grade edges as shown in the lower part of fig.8.2d, this approach does not yield the desired results for porous structures as can be seen in the upper part of fig.8.2d and fig.8.2c. One reason for this was the insufficient lateral alignment precision of the cutting edge relative to the pores. This challenge could be solved by equipping the system with optical components having higher magnification to allow precise alignment of the cutting edge relative to the micrometer sized pores. A more severe limitation of this technique turned out to be the vertical profile of the laser beam. Along the z -axis the intensity distribution is approximately Gaussian. As a result the vertical profile of the laser cut will not be straight but curved. For the ARL this means that its thickness t_{ARL} is not homogeneous along the z -direction, either resulting in reduced performance or even in cutting through the outermost pore row(s) of the air/PhC interface at certain depths².

As a second approach polishing using the fs laser was investigated. For this purpose a fast, crude cut approximately at the desired position of the ARL was made using the fs laser. Now the fs laser beam was slowly brought closer to the resulting cutting edge and moved along the cutting edge to polish it, i.e., to make it smoother. Unfortunately this approach did also not yield the desired flat, optically high grade interfaces.

Furthermore, this technique which is not based on off-the-shelf components is relatively expensive (several hundred EUR/hour while one cut of about a mm takes between several minutes up to several ten minutes, depending on the parameters chosen).

8.3.4 RIE etching

As another approach to realize high grade air/PhC interfaces RIE was investigated together with the FhG IPM in Freiburg which contributed lithography and etching facilities. The Bosch process - a method developed for deep Si etching - was used. After PECE fabrication of the macropore array, the pores were covered with Al and in a subsequent lithography step a mask defining the boundaries of the various gas sensor devices was applied. After that the Al was opened and the RIE of the macropore array was realized. The result is shown in fig.8.2e. While this method could in principle be used to realize nice corrugated PhC interfaces, it proved insufficient to fabricate the ARL. The main obstacle is again the necessary, but not achievable, lateral alignment precision.

8.3.5 PECE of the ARL

From the discussion of the preceding sections 8.3.1, 8.3.2, 8.3.3 and 8.3.4 it is obvious that device dicing *after* fabrication of the macropore array is not the method of choice for the realization of PhC interaction volumes, no matter whether with or without ARL.

The fabrication of the ARL layer during the PECE process described in section 6.4.2 not only

¹The fs laser cutting experiments have independently been performed at the Fraunhofer Institute for Applied Physics (*FhG IAP*) in Jena and at the Laser Zentrum Hannover (*LZH*) associated with *Micreon* company, Hannover.

²An improvement in vertical beam quality could be achieved using the systems sold by Synova (<http://www.synova.ch>). Index guiding of the laser beam injected into a fluid jet is used for confinement along the z -direction.

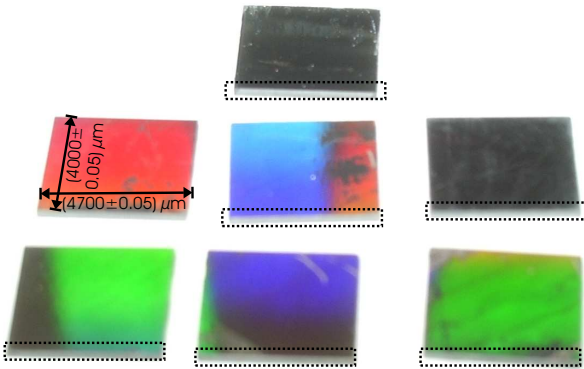


Figure 8.3: Successful device dicing: trenches etched during PECE. The size of the devices can be defined to fractions of microns and the coupling interfaces (highlighted by the black dotted lines) are flat and shiny, i.e., optically high grade concerning surface roughness scattering losses. In addition the ARL functionality is integrated. The colorful surfaces stem from the lithographically defined pore pattern on the front of the Si wafer. Two samples are shown from their bottom side. The rough surface of the pore bottoms results in the pitch black color.

allows the realization of the ARL concept developed to achieve high transmission through the PhC. It also simplifies device dicing.

A deep trench ($\gtrsim 350 \mu\text{m}$) etched into the initially massive Si wafer has a higher porosity than the surrounding macropore array. If now force is applied next to the trench, e.g., by a pair of tweezers, the trench - which was aligned in the [110] direction of the Si during lithography - neatly guides the rupture and an optically high grade air/PhC interface defined by the ARL is achieved. This simple yet powerful concept of PECE trenches is the key concept and a major step towards macroporous Si-based PhC spectroscopic gas sensors because on one hand it allows the realization of the ARL and on the other hand it enables easy access to physically handy devices with sub-micron precision, as shown in fig.8.3.

Chapter 9

Summary

The goal of this work was to study the feasibility of PhC-based spectroscopic gas sensors. Both, the theoretical design as well as the fabrication of appropriate structures utilizing the macroporous Si material system were successfully demonstrated and first optical characterizations were carried out.

In a PhC-based spectroscopic gas sensor a macroporous Si membrane is to replace the conventional interaction volume. Utilizing the possibility to design the bandstructure of the PhC to exhibit low group velocity of light allows to enhance the interaction between the gas flowing through the pores and the light transmitted perpendicular to the macropores. As consequences, either the size of the interaction volume of the gas sensor could be reduced while maintaining the same sensitivity as a conventional spectroscopic gas sensor or by maintaining the size of the interaction volume the sensitivity could be increased by the enhancement factor. For this purpose the macroporous Si PhC is designed in such a way that a mode having low group velocity v_g spectrally overlaps with an absorption frequency of the gas to be detected. If, in addition, a large part of the electric field of that PhC mode is located within the pores and the symmetry of the Bloch mode allows coupling to plane waves, the interaction of light and gas within the PhC membrane is enhanced. Due to the linearity of Maxwell's equations the PhC-based spectroscopic gas sensor concept is scalable. Using the macroporous Si material system gas absorption lines in the NIR and MIR spectral ranges are accessible. The design of a PhC-based gas sensor was discussed using SF_6 and ethanol as an example.

First, the interaction volume was appropriately designed. Starting from a hexagonal array of air pores embedded in a Si matrix four promising bands (TEB02K, TMB03K, TEB03M, TMB04M) useful for gas detection were identified. During the further design steps in this work focus was put on the bands TEB02K and TMB03K because among the four promising gas sensing bands they have the highest amount of energy stored in the pore region (41% and 21%, respectively). Fine tuning ($\Delta\lambda \pm 100$ nm) of the developed interaction volume design, e.g., to compensate for minor fabrication tolerances, is possible by rotating the PhC structure by a few degrees ($< 10^\circ$) around an axis parallel to the macropores. The design is furthermore robust concerning typical temperature changes ($\Delta T < 100^\circ$).

Next, strategies to achieve efficient coupling of incoming and outgoing radiation to the PhC interaction volume were investigated. This is necessary because due to the low group velocity of the mode under study, high reflection at the air/PhC interfaces is expected. The first approach was

based on adiabatic adjustment of the effective refractive index by distorting the hexagonal lattice. While this taper strategy looks reasonable from bandstructure arguments and physical intuition, it was shown by FDTD and FEM simulations to worsen coupling. As reason for this the large portion of higher order contributions of the Bloch mode under consideration was identified. As an alternative, a concept entitled **Anti-Reflection-Layer**¹ was developed. It utilizes surface modes created by non-conventional termination of the PhC surface to couple incoming and outgoing radiation to the desired Bloch mode. In numerical simulations it was shown that by using the ARL concept the transmission through the PhC structure could be drastically increased, even in a spectral region where the photonic bands are flat. The robustness of this design under rotation ($T > 60\%$ even for incidence angles of 10°) was demonstrated. The enhancement factor was determined to be on the order of 30.

The so far theoretically studied and numerically simulated structures were then fabricated using the macroporous Si material system. By exposing lithographically prestructured n-Si wafers to aqueous HF electrolytes, it is possible to grow ordered, macroporous structures by applying an appropriate external potential and illumination of the wafer from the backside. The already well established growth of about $100\ \mu\text{m}$ deep macropores was extended to achieve high quality macroporous structures with a depth of more than $400\ \mu\text{m}$. Effects of surfactants added to the electrolyte were investigated. Furthermore, growth of distorted hexagonal lattices of air pores in Si was shown. In addition, the growth of trenches next to ordered arrays of macropores was successfully demonstrated. This is a major achievement since it allows in-situ realization of the ARL concept during photo-electrochemical etching, i.e., no postprocessing of the samples is necessary. In addition, this technique allows the realization of *almost flat coupling interfaces* of the PhC structure, a necessary prerequisite for minimal scattering loss of incoming and outgoing light. Furthermore, the in-situ trench etching allows device dicing with *sub-micron precision*. The observed increased roughness and texture on the ARL coupling interface was explained by looking at the potential gradients in the vicinity of the ordered macropore/ARL interface within the framework of the space charge region model.

First experiments concerning the optical characterizations were performed. Although up to now no transmission through large (cm scale) devices could be achieved, reflection measurements show the predicted formation of surface states due to the ARL and reduced reflection for the corresponding frequencies. Polarization dependent transmission through sub-mm scale PhC structures was however demonstrated using FTIR spectrometry as well as a QCL setup. As likely sources of loss phonon absorption and scattering due to pore wall roughness were identified. Other sources of loss such as imperfections of the PhC structure itself (e.g., variations in pore position and/or pore diameter) are currently under investigation.

In the last part the integration of the PhC interaction volume into a complete gas sensor device was considered. Although direct coupling of a thermal emitter to the sample and then to the detector yields the lowest transmission (18%), the simplicity of this design makes it rather attractive.

¹Not to be confused with the classical Anti-Reflection-Coating known from wave optics to reduce reflection at dielectric interfaces.

Chapter 10

Conclusion and outlook

The experimental proof-of-principle of a PhC-based spectroscopic gas sensor by measuring the enhanced absorption and the enhanced interaction of light and gas, respectively, has not yet been demonstrated. However, after the design and the progress in fabrication techniques developed in this thesis a demonstrator seems to be within reach. The challenge consists in the achievement of transmission through PhC structures of several mm length. Currently, the roughness of the pore wall surfaces is suspected to be the major reason for high scattering losses. Investigation of this topic and reduction of the surface roughness by either changes in the PECE parameters or, e.g., wet chemical postprocessing, is currently being performed.

The chances of such a new type of spectroscopic gas sensor to make its way to a commercial product are promising. However, to bring the fabrication from laboratory to industrial production scale will take some more time, money and manpower. Recent developments indicate that photonic crystal structures might find their application first in sensing schemes and not so much in optics, as was envisioned when this field emerged.

Further developments of the design suggested so far might concern alternative or improved coupling schemes, different from the ARL concept. Vertical confinement of light in the PhC structure could be achieved and optimized by using index guiding along the z -direction as depicted in fig.10.1a. Macropores with increased diameter in their top and bottom part and a central part used for gas detection are a possible realization. In case it turns out that transmission of light through several hundred or thousand unit cells of a PhC structure is not realizable, a reflection-based PhC gas sensor shown in fig.10.1b might be an alternative. Here the total interaction would be limited by the penetration depth of light into the PhC structure. This would then have to be

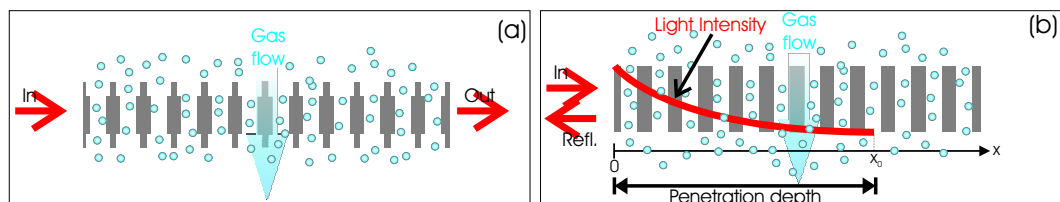


Figure 10.1: Alternative PhC-based gas sensor schemes: **a)** Transmission-based with vertical light confinement by index guiding due to lower n_{eff} above and below the detection region. **b)** Reflection-based.

(over)compensated by the enhancement factor.

Another option to avoid problems arising from transmission through very large bulk PhC volumes is to use PhC waveguide structures. Light transmission through PhC waveguides of several hundred lattice constants has been demonstrated. In addition it is possible to tailor its dispersion properties to realize low group velocities. The interaction with the gas in the surrounding pores could be achieved by the parts of the guided mode that penetrate into the surrounding pores. Closely packed waveguides could therefore be almost as effective as a bulk PhC. Such structures could in principle also be realized in the macroporous Si material system and are compatible with the ARL concept, promising efficient coupling as well as precise and easy device fabrication.

In principle, other material systems such as, e.g., opals, could also be explored since they can also be produced on a macroscopic scale. Due to their inherently 3-dimensional nature their photonic band structure might offer promising bands for gas sensing with additional interesting properties.

Appendix A

Miscellaneous

A.1 Lattices

In this section important vectors etc. used in this work are given.

A.1.1 The hexagonal lattice

The basis vectors \vec{a}_1, \vec{a}_2 for a regular hexagonal lattice with lattice constant a can be chosen as

$$\vec{a}_1 = \left(\frac{a\sqrt{3}}{2}, \frac{a}{2} \right), \quad \vec{a}_2 = \left(\frac{a\sqrt{3}}{2}, -\frac{a}{2} \right). \quad (\text{A.1})$$

The corresponding basis vectors of the reciprocal lattice are

$$\vec{b}_1 = \frac{2\pi}{\sqrt{3}a} \left(1, \sqrt{3} \right), \quad \vec{b}_2 = \frac{2\pi}{\sqrt{3}a} \left(1, -\sqrt{3} \right). \quad (\text{A.2})$$

The coordinates of the high symmetry points $\vec{\Gamma}, \vec{M}, \vec{K}$ in reciprocal space coordinates, i.e., in multiples of \vec{b}_1 and \vec{b}_2 are

$$\vec{\Gamma} = (0, 0), \quad \vec{M} = (0, 0.5), \quad \vec{K} = \left(-\frac{1}{3}, \frac{1}{3} \right). \quad (\text{A.3})$$

A.1.2 The distorted hexagonal lattice

The basis vectors \vec{a}'_1, \vec{a}'_2 for a distorted hexagonal lattice with lattice constants a_x and a_y along the ΓM_2 and the ΓK_1 directions with the distortion expressed in terms of a factor $f := a_y/a_x$ can be chosen as

$$\vec{a}'_1 = \left(\frac{a_x\sqrt{3}}{2}, \frac{a_y\sqrt{3}}{2} \right), \quad \vec{a}'_2 = \left(\frac{a_x\sqrt{3}}{2}, -\frac{a_y\sqrt{3}}{2} \right) \quad (\text{A.4})$$

The corresponding basis vectors of the reciprocal lattice are

$$\vec{b}'_1 = \frac{2\pi}{\sqrt{3}} \left(\frac{1}{a_x}, \frac{\sqrt{3}}{a_y} \right), \quad \vec{b}'_2 = \frac{2\pi}{\sqrt{3}} \left(\frac{1}{a_x}, -\frac{\sqrt{3}}{a_y} \right) \quad (\text{A.5})$$

The coordinates of the high symmetry points $\vec{\Gamma}$, \vec{K}_1 , \vec{M}_1 , \vec{K}_2 and \vec{M}_2 in reciprocal space coordinates, i.e., in multiples of \vec{b}'_1 and \vec{b}'_2 are

$$\vec{\Gamma} = (0, 0), \quad \vec{K}_1 = (-\beta', \beta'), \quad \vec{M}_1 = (0, 0.5), \quad \vec{K}_2 = (1 - \delta', \delta'), \quad \vec{M}_2 = (0.5, 0.5) \quad (\text{A.6})$$

with

$$\beta' = \frac{3 + f^2}{12} \quad \text{and} \quad \delta' = \frac{9 - f^3}{12}. \quad (\text{A.7})$$

A.2 Bragg diffraction at PhC interfaces

Light of wavelength λ impinging onto a dielectric/PhC interface as depicted in fig.5.7a sees a periodically structured surface and therefore Bragg diffraction may occur, if the relation

$$k_{\text{inc},\parallel} + k_{\text{diff},\parallel} = mk_{\text{surf}} \quad (\text{A.8})$$

is fulfilled. Here $k_{\text{inc},\parallel}$ and $k_{\text{diff},\parallel}$ are the wavevector components parallel to the interface for a wave with wavevector \vec{k}_{inc} incident under an angle α_{inc} and a diffracted wave with wavevector \vec{k}_{diff} reflected under an angle α_{diff} (the angles measured with respect to the surface normal) and m is an integer number. The components parallel to the interface can be expressed as

$$k_{\text{inc},\parallel} = \frac{2\pi n}{\lambda} \sin(\alpha_{\text{inc}}) \quad (\text{A.9})$$

$$k_{\text{diff},\parallel} = \frac{2\pi n}{\lambda} \sin(\alpha_{\text{diff}}) \quad (\text{A.10})$$

with n being the refractive index of the dielectric medium. For a hexagonal PhC the surface grating vectors along ΓK and ΓM are $k_{\text{surf},\Gamma\text{K}} = \frac{2\pi}{a}$ and $k_{\text{surf},\Gamma\text{M}} = \frac{2\pi}{a\sqrt{3}}$ with a the lattice constant of the PhC. Together with (A.8), (A.9) and (A.10) the frequency range in which Bragg diffraction can occur can be calculated as a function of the incidence angle. For the limiting cases of incidence perpendicular ($\alpha_{\text{inc}} = 0^\circ$) and parallel ($\alpha_{\text{inc}} = 90^\circ$) to the interface Bragg diffraction can occur for normalized frequencies given in tab.A.1.

	ΓK	ΓM
$\alpha_{\text{inc}} = 0^\circ$	$\frac{1}{n} \leq \left(\frac{a}{\lambda}\right) < \infty$	$\frac{1}{n\sqrt{3}} \leq \left(\frac{a}{\lambda}\right) < \infty$
$\alpha_{\text{inc}} = 90^\circ$	$\frac{1}{2n} \leq \left(\frac{a}{\lambda}\right) < \frac{1}{n}$	$\frac{1}{2n\sqrt{3}} \leq \left(\frac{a}{\lambda}\right) < \frac{1}{n\sqrt{3}}$

Table A.1: Normalized frequencies for which Bragg diffraction at a hexagonal PhC interface can occur.

Appendix B

Publications and presentations

B.1 Publications

B.1.1 Publications primarily related to this thesis

Application of photonic crystals for gas detection and sensing

R.B. Wehrspohn, S.L. Schweizer, J. Schilling, T. Geppert, C. Jamois, R. Glatthaar, P. Hahn, A. Feisst, and A. Lambrecht

Photonic Crystals: Advances in Design, Fabrication and Characterization, ed. K. Busch, S. Lölkes, R.B. Wehrspohn and H. Föll, Wiley-VCH, 238 (2004)

Silicon-Based Photonic Crystals

T. Geppert, J. Schilling, R.B. Wehrspohn, and U. Gösele

Silicon Photonics, ed. L. Pavesi and D.J. Lockwood, Springer: Topics in Applied Physics, **94**, 295 (2004)

Photonic Crystals: Fundamentals and Applications

A.v. Rhein, T. Geppert, and R.B. Wehrspohn

Encyclopedia of Materials, (2005) (in press)

Photonic crystal gas sensors

T.M. Geppert, S.L. Schweizer, J. Schilling, C. Jamois, A.v. Rhein, D. Pergande, R. Glatthaar, P. Hahn, A. Feisst, A. Lambrecht, and R.B. Wehrspohn

Tuning the Optical Response of Photonic Bandgap Structures, ed. Philippe M. Fauchet and Paul V. Braun, Proceedings of SPIE, **5511**,5511-07 (2004)

Photonic crystal gas sensors

R.B. Wehrspohn, T.M. Geppert, S.L. Schweizer, A. v. Rhein, D. Pergande, T. Beyer, A. Lambrecht

Proceedings of SPIE - 17th International Conference on Optical Fibre Sensors, **5585**,24-29 (2005)

Design of a New Taper for Light Coupling Between a Ridge Waveguide and a Photonic Crystal Waveguide

C. Jamois, T. Geppert, and R.B. Wehrspohn

Mat. Res. Soc. Symp. Proc., **797**, W6.7.1-W6.7.5 (2004)

B.1.2 Further publications

Lithium niobate microtubes within ordered macroporous silicon by templated thermolysis of a single source precursor

L. Zhao, M. Steinhart, M. Yosef, S.K. Lee, T.M. Geppert, E. Pippel, R. Scholz, U. Gösele, and S. Schlecht

Chemistry of Materials, **17**,(1), 3 (2005)

SOI planar photonic crystal fabrication: Etching through SiO₂/Si/SiO₂ layer systems using fluorocarbon plasmas

A.P. Milenin, C. Jamois, T.M. Geppert, U. Gösele, and R.B. Wehrspohn

Microelectronic Eng., **81** (1), 15 (2005)

Preferential Formation of Al-N bonds in low N-content AlGaAsN

T. Geppert, J. Wagner, K. Köhler, P. Ganser, M. Maier

Appl. Phys. Lett., **80**, (12), 2081 (2002)

Quaternary GaInAsN with high In content: dependence of bandgap energy on N-content

D. Serries, T. Geppert, P. Ganser, M. Maier, K. Köhler, N. Herres, and J. Wagner

Appl. Phys. Lett., **80**, 2448 (2002)

SIMS depth Profiling of InGaAsN/InAlAs quantum wells on InP

M. Maier, D. Serries, T. Geppert, K. Köhler, H. Güllich and, N. Herres

Appl. Surf. Sci., **486**, 203 (2003)

Bonding of nitrogen in dilute GaInAsN and AlGaAsN studied by Raman spectroscopy

J. Wagner, T. Geppert, K. Köhler, P. Ganser, and M. Maier

Solid-State Electronics., **47**, 461 (2003)

Dilute Group III-AsN: Bonding of Nitrogen in GaInAsN and AlGaAsN on GaAs and Realization of Long Wavelength ($\lambda = 2.3 \mu\text{m}$) GaInAsN QWs on InP

D. Serries, T. Geppert, K. Köhler, P. Ganser, and J. Wagner

Mat. Res. Soc. Symp. Proc., **744**, 627 (2003)

The realization of long-wavelength ($\lambda=2.3 \mu\text{m}$) GaInAsN quantum wells on InP by molecular-beam epitaxy

K. Köhler, J. Wagner, P. Ganser, D. Serries, T. Geppert, M. Maier, and L. Kirste

J. Phys. Condens. Matter, **16**, 2995 (2004)

Epitaxy and characterization of dilute III-As_{1-y}N_y on GaAs and InP

K. Köhler, J. Wagner, P. Ganser, D. Serries, T. Geppert, M. Maier, and L. Kirste

IEEE Proceedings "Optoelectronics", **151**, 247 (2004)

B.2 Selected Talks

B.2.1 Invited

Photonic crystal gas sensors

T.M. Geppert, S.L. Schweizer, J. Schilling, C. Jamois, A.v. Rhein, D. Pergande, R. Glatthaar, P. Hahn, A. Feisst, A. Lambrecht and R.B. Wehrspohn

SPIE 49th Annual Meeting: Optical Science and Technology, 2.-6. August 2004, Denver (Co),

USA

Si-based Photonic Crystals

T.M. Geppert and R.B. Wehrspohn

2nd Sino-German Symposium "The Silicon Age: Silicon for Micro- and Nanoelectronics, Photovoltaics, Photonics, Electrical Biochips and Micro-Opto-Electro-Mechanics", September 19.-24. 2005, Cottbus (Germany)

B.2.2 Contributed

Photonic Crystal Based Spectroscopic Gas Sensors

T.M. Geppert, D. Pergande, A.v. Rhein, S.L. Schweizer, R.B. Wehrspohn, and A. Lambrecht
Frühjahrstagung der Deutschen Physikalischen Gesellschaft, March 04.-09. 2005, Berlin (Germany)

Towards Photonic Crystal-based Spectroscopic Gas Sensors

T.M. Geppert, D. Pergande, A.v. Rhein, S.L. Schweizer and R.B. Wehrspohn
MRS Fall Meeting, November 28-December 02, 2005, Boston, MA (USA)

B.3 Posters

Gas Sensors Based on 2D Photonic Crystals

T.M. Geppert, S.L. Schweizer, R.B. Wehrspohn, and A. Lambrecht
Frühjahrstagung der Deutschen Physikalischen Gesellschaft, March 08.-12. 2004, Regensburg (Germany)

Compact Gas Sensors Based on 2D Photonic Crystals

T.M. Geppert, A.v. Rhein, S.L. Schweizer, R.B. Wehrspohn, and A. Lambrecht
323. WE-Heraeus-Seminar "From Photonic Crystals to Metamaterials: Artificial Materials in Optics", April 26.-30. 2004, Bad Honnef (Germany)

Photonic Crystals for Compact Gas Sensors

T.M. Geppert, D. Pergande, A.v. Rhein, S.L. Schweizer and R.B. Wehrspohn
PECS-VI: International Symposium on Photonic and Electromagnetic Crystal Structures, June 19.-24. 2005, Aghia Pekaghia, Crete (Greece)

B.4 Patents

Strahler, sowie Vorrichtung und Verfahren zur Analyse der qualitativen und/oder quantitativen Zusammensetzung von Fluiden mit einem solchen Strahler (Selektiver thermischer Emitter) T.M. Geppert, A.v. Rhein, S.L. Schweizer, R.B. Wehrspohn, A. Lambrecht; Patentanmeldung: DE102005008077.4

Einkoppelschichten für Gassensoren T.M. Geppert, D. Pergande, A.v. Rhein, R.B. Wehrspohn; Patentantrag wird momentan bearbeitet

Appendix C

C.1 Eidesstattliche Erklärung

Ich erkläre hiermit an Eides Statt, dass ich die vorliegende Arbeit selbstständig und ohne Benutzung anderer als der angegebenen Hilfsmittel angefertigt habe; die aus fremden Quellen direkt oder indirekt übernommenen Gedanken sind als solche kenntlich gemacht.

Die Arbeit wurde bisher in gleicher oder ähnlicher Form keiner anderen Prüfungskommission vorgelegt und auch nicht veröffentlicht.

.....

Torsten Geppert

C.2 Declaration in lieu of oath

Hereby I declare that I have prepared this thesis by myself and without the use of resources other than the ones indicated in this thesis. Quotations, verbatim or with regard to content, from other sources are marked as such. This work, in the same or any similar form, was neither handed in to any other doctorate committee nor was it published before.

.....

Torsten Geppert

Appendix D

Curriculum Vitae

Personal

Family name: Geppert
First name: Torsten, Michael
Date of birth: March 10, 1975
Place of birth: Offenburg (Germany)
Nationality: German
Present address: Parkstrasse 20, D-06108 Halle (Germany)
e-mail: tgeppert@mpi-halle.mpg.de

Education:

June 1985–June 1994 Secondary school Gengenbach (Baden-Württemberg), Germany

Apr. 1995–Sep. 1995 University of Education, Freiburg i. Br., Germany

Oct. 1995–Aug. 1998 Undergraduate courses in physics (*Vordiplom*) at the Albert-Ludwigs-Universität, Freiburg i. Br., Germany

Sep. 1998–May 1999 Courses of physics (Max-Kade Fellowship) at the University of Michigan, Ann Arbor, USA

June 1999–Sep. 2000 Graduate courses in physics at the Albert-Ludwigs-Universität Freiburg, i. Br., Germany

Oct. 2000–March 2002 Master's thesis (*Diplomarbeit*) at the Fraunhofer-Institut for Applied Solid State Physics (*FhG-IAF*), Freiburg i. Br., Germany: " *Molecular beam epitaxy and characterization of dilute III-Arsenide/Nitride semiconductors*"; Grade: A+ (1.0)

March 2002–Aug. 2002 Epitaxy of Ga(In)N for UV LEDs and lasers by Metal-Organic-Chemical-Vapor-Deposition (*MOCVD*)

Sept. 2002–present Max Planck Institute of Microstructure Physics, Halle (Germany) and University Paderborn (Germany), PhD thesis " *Towards Photonic Crystal-based Spectroscopic Gas Sensors*"

Appendix E

Acknowledgements

Here I would like to express my gratitude and appreciation to all the persons and entities who supported me during the last three years in which I prepared my thesis.

Thank you, Prof. Gösele for supervising my thesis and giving me the opportunity to work at the Max Planck Institute of Microstructure Physics. I enjoyed your broad scientific background and your focussed nature. There were many useful lessons to learn...

Thank you, Prof. Wehrspohn for giving me the opportunity to work on such an interesting topic and the necessary freedom. Thanks for your optimism, your motivational character, your creative ideas and financial support.

Special cheers to the **Paderborn team !**

Thank you, Andreas and **Daniel** for your support concerning theoretical questions, the fruitful discussions, your creativity, your teamwork, and last but not least the numerical support !

Thank you, Stefan for introducing me to the macroporous Si etching, your assistance in our attempt of large scale sample fabrication - and for the evening program during my scientific visits in Paderborn.

Finally, thanks to Prof. Wehrspohn's assistant **Stefanie Jack** who gave me the necessary support in issues related to administrative and organizational challenges...

I would also like to say thanks to the MPI MSP photonic crystal people,

Dr. Frank Müller and **Dr. Sven Matthias** for discussions about the macroporous Si material system.

Thank you, **Cécile** for your introduction to the MIT package and sharing your waveguide coupling problems with me. I think we learned a lot during our discussions.

Kornelia Sklarek, thanks for your outstanding support concerning laboratory issues. Without your commitment much less experiments would have been possible and chaos would have taken over our labs. It was my pleasure to work with you !

Thanks, Danilo for the AFM support.

Thanks to Dr. Volker Lehmann of Infineon Technologies for making it possible to use Infineon's capabilities in Si technology. Only his commitment and the dedication of Infineon's **Barbara Hasler** and **Alfred Martin** gave us access to Si wafers of the quality necessary for the realization of our PhC structures.

I acknowledge the financial support from the BMBF within the framework of the *PhoKiss* project (13N8525) as well as the cooperation with the partners in this project, especially **Hans Matthiessen** and **Dr. Axel Lamprecht** of Drägerwerk AG, AMAT's **Prof. Dr. Hellmut Föll** and **Eugen Foca** and **Dr. Thomas Beyer**, **Jürgen Hildenbrand**, **Susanne Hartwig**, **Dr. Iliyana Hinkov** and **Dr. Armin Lambrecht** of Fraunhofer IPM, Freiburg.

Cheers go to all my colleagues and friends at the MPI MSP, in Halle and the University Paderborn who supplied the necessary motivational background and atmosphere to make it possible for me to compile this thesis. Thanks, Frank for the awesome Squash battles, **Sven** and **Martin** for the running support, **Florian**, **Mindy** and **Ulrike** for the broadening of our horizon concerning tasty wines, **Franz** for joining the vegetarian community, **Dr. Martin Steinhart**, **Dr. Reinald Hillebrand**, **Luise**, **Andreas**, **Johannes**, **Jan**, **Carsten**, **Petra**, **Kathrin**, **Stefan**, **Silko**, **Claudia**, **Yun** and **Jinsub** for just being part of the MPI community.

Last but not least I want to thank my **family** and my **SO Ursula** for their continuous support, tolerance and motivation during my studies and the time of my thesis.

Appendix F

Abbreviations and symbols

$1D, 2D, 3D$: 1-, 2-, 3-dimensional

∇ : Nabla-operator

Δa_{Si} : change of the atomic lattice constant of bulk Si, e.g., due to a temperature change

α, α_{inc} : angle of incidence (relative to surface normal)

α_{diff} : angle of diffraction (relative to surface normal)

α_s : scattering loss per pore row

$\alpha_{TIR, Si/air}$: angle at which total internal reflection occurs at a plane Si/air interface

$\alpha(\tilde{\nu})$: absorption coefficient of gases

a : lattice constant of a PhC

a_0 : lattice constant of the PhC in the region used for detection

$\vec{a}_1, \vec{a}_2, \vec{a}_3$: basis vectors of the real space lattice of a hexagonal PhC

$\vec{a}'_1, \vec{a}'_2, \vec{a}'_3$: basis vectors of the real space lattice of a distorted, originally hexagonal PhC

a_B : Bohr radius 5.3×10^{-11} m

a_c : lattice constant of the PhC optimal for coupling (in the adiabatic taper approach)

AE : absorption enhancement due to a PhC interaction volume compared to light/gas interaction in free space

AFM : Atomic Force Microscopy

\vec{a}_{int} : basis vector of the real space lattice along the interface of the *finite* PhC

a_{lc} : lattice constant of a PhC used to achieve lateral confinement

a_t : lattice constant of the PhC in the taper region (in the adiabatic taper approach)

A_{pores} : area of the pores in a porous Si sample

AR : aspect ratio

ARC : Anti-Reflection-Coating

ARL : Anti-Reflection-Layer

A_{sample} : total area of the HF/Si interface

a_{Si} : atomic lattice constant of bulk Si

\vec{B} : magnetic induction

BAW : bulk acoustic wave

\vec{b}_{int} : basis vector of the reciprocal lattice along the interface of the *finite* PhC

$\vec{b}_1, \vec{b}_2, \vec{b}_3$: basis vectors of the reciprocal space lattice of a hexagonal PhC (with high symmetry points Γ , M and K)

$\vec{b}'_1, \vec{b}'_2, \vec{b}'_3$: basis vectors of the reciprocal space lattice of a distorted, originally hexagonal PhC with high symmetry points Γ , K_1 , M_1 , K_2 and M_2

BZ : Brillouin zone (the Wigner-Seitz-cell in reciprocal space)

ΔC : change of capacitance

- c_0 : speed of light in free space
 c : concentration of the gas under study
 c_a, c_b : empirical constants used to relate growth time and macropore depth in Lehmann's model
 c_{HF} : HF concentration of the electrolyte (in weight %)
 CH_4 : methane (gas)
 $c_{\text{HF,tip}}$: HF concentration of the electrolyte (in weight %) at the pore tip
 CO, CO_2 : carbon monoxide, carbon dioxide (gases)
 $c_{\text{AIS}}, c_{\text{NIS},1}, c_{\text{NIS},2}$: concentration of non-ionic, original anionic and new anionic surfactant added to the HF electrolyte
 CW : Crystal Wave (commercial FDTD Software by Photon Design, www.photond.com)
 $\Delta\epsilon$: change of dielectric constant of a material
 \vec{D} : dielectric displacement
 ΔI_e : change in electric current
 Δn : dielectric contrast $n_1 - n_2$
 Δs_{R2} : additional optical path light travels in the ARL
 d_{coat} : thickness of a coating layer on the pore walls
 D_{HF} : diffusion coefficient of HF ($\approx 10^{-5} \text{ cm}^2 \text{ s}^{-1}$), independent of HF concentration for $2\% \leq c_{\text{HF}} \leq 10\%$
 d_{Pore} : diameter of the pores
 d_{Porewall} : thickness of the remaining pore walls between macropores
 ϵ_{air} : dielectric constant of air
 ϵ_0 : dielectric constant of free space
 ϵ_{mat} : dielectric constant of a dielectric material
 ϵ_{Si} : dielectric constant of Si
 e : exponential function
 e^- : electron
 \vec{E} : electric field
 $\vec{E}_{\text{air}}(\vec{r}), \vec{E}_{n,k}(\vec{r})$: electric fields in air and in a PhC, respectively
 em : electro-magnetic
 $\text{C}_2\text{H}_5\text{OH}$: ethanol (gas)
 F_C : Faraday's constant
 FDTD : Finite-difference time-domain
 FEM : numerical scheme based on finite elements
 FFT : Fast-Fourier-Transformation
 FL : FEMLAB (FEM software for multiphysics modelling)
 FTIR : Fourier-transform infrared spectroscopy
 \vec{G} : reciprocal lattice vector
 h^+ : electronic hole
 \vec{H} : magnetic field
 H : hydrogen
 HF : hydrofluoric acid
 HP : HelmPole (FEM software developed at ZIB, www.zib.de)
 ICP : inductively coupled plasma etching
 IFFT : Inverse Fast-Fourier-Transformation
 I_0 : transmitted intensity without gas being present in the detection volume
 $I(\nu)$: spectrum of light, e.g., of a GloBar
 $I(l_{\text{int}})$: transmitted intensity after interaction of light and gas along a path of length l_{int}
 $\text{IR}, \text{NIR}, \text{MIR}, \text{FIR}$: infrared, near infrared, medium infrared and far infrared spectral regions, respectively
 j : current density across the sample during PECE

- j_{PS} : current density at which electropolishing of Si occurs
 \vec{k} : wavevector
 k_{B} : Boltzmann's constant
 $\vec{k}_{\text{diff}}, k_{\text{diff},\parallel}$: wavevector of a wave incident onto a PhC and its parallel component, respectively
 $\vec{k}_{\text{inc}}, k_{\text{inc},\parallel}$: wavevector of a wave incident onto a PhC and its parallel component, respectively
 k_{surf} : wavevector contribution of a grating
 $k_{\text{surf},\Gamma\text{K}}, k_{\text{surf},\Gamma\text{M}}$: wavevector contribution of the PhC surface grating along ΓK and ΓM directions, respectively
 λ_{mat} : wavelength in a material
 λ_{vac} : wavelength in free space
 l_{int} : real interaction length between light and gas
 $l_{\text{int,eff}}$: effective interaction length between light and gas
 lc : lateral confinement
 LED : light emitting diode
 l_{pore} : length of a pore
 $LP\text{-CVD}$: low pressure chemical vapor deposition
 Δm : change of mass
 μ_0 : magnetic permeability of free space
 μ_{Si} : magnetic permeability of Si
 m_1, m_2, m_3 : integer numbers
 \vec{M}' : edge point of the BZ for the *finite*PhC
 MIT : Massachusetts Institute of Technology
 MPB : MIT Photonic Bands (free software for computation of eigenstates and eigenfrequencies of PhCs)
 MO : metal-oxide
 $MPI\ MSP$: Max Planck Institute of Microstructure Physics, Halle, Germany
 Δn_{Si} : change of the refractive index of Si n_{Si}
 η : coupling coefficient at dielectric interfaces
 ν : frequency of light [s^{-1}]
 \vec{v}_j : localized function in FEM scheme
 n : band index in (photonic) band structures
 n_{air} : refractive index of air
 n_{ARC} : refractive index of an Anti-Reflection-Coating (ARC)
 n_{coat} : refractive index of a coating layer, e.g., on the pore walls
 N_{D} : doping density [cm^{-3}]
 n_{mat} : refractive index of a dielectric material
 n_{Si} : refractive index of Si
 NO, NO_2 : nitrogen monoxide, nitrogen dioxide (gases)
 N_{PR} : number of pore rows
 N_{Si} : atomic density of Si
 n_{val} : dissolution valence
 ω : angular frequency $2\pi\nu$ of light with frequency ν
 ω_{abs} : absorption frequency of a gas molecule
 ω_{norm} : normalized frequency $(\omega a)/(2\pi c)$ commonly used in PhBS diagrams
 $\omega_{\text{norm,SF}_6}$: normalized absorption frequency of SF_6
 $\Psi_{n,\vec{k}}(\vec{r})$: Bloch state
 p : porosity of a porous Si sample
 $p_{\text{ARL,t}}$: porosity in the region close to the ARL
 $PEC(E)$: photo-electrochemical (etching)
 $PhBG$: photonic band gap

- PhBS* : photonic band structure
PhC : photonic crystal
PhDOS : photonic density of states
 p_{hex} : porosity of a ordered, hexagonal macropore array
PML : perfectly matched layer boundary conditions in FDTD and FEM
PW : plane wave
PWE : plane wave expansion
 ΔQ : size of spatial grid in FDTD or FE numerical calculations
 q : elementary charge (1.602×10^{-19} C)
 Q_1, Q_2, Q_3 : spatial grid size in FDTD calculation
QCL : Quantum Cascade Laser
QCM : quartz crystal microbalance
 ΔR_e : change in electrical resistance
 ρ_{free} : free charges in Maxwell's equations
 r : radius of a macropore
R : reflection at dielectric interface
 $R(\alpha = 0^\circ)$: reflection at dielectric interface according to Fresnel's equation for perpendicular incidence
RIE : reactive ion etching
 \vec{R} : vector specifying a lattice site of the real space lattice
 r_0 : radius of a macropore in the bulk PhC region
 r_{2D} : vector (x,y) in real space
 r_{3D} : vector (x,y,z) in real space
 R_g : universal gas constant
 r_{lc} : pore radius in a PhC used for lateral confinement
rms : root-mean-square
 r_{Pore} : radius of macropores
 r_s : surface roughness, given as the rms value
ro-vib : rotational-vibrational (excitation of a molecule)
 $\Delta \sigma_e$: change in electrical conductivity
 s : factor used for rescaling PhCs
 $S(t)$: intensity at the detector in FTIR spectroscopy
 SF_6 : sulfur-hexafluoride (gas)
SAW : surface acoustic wave
SNR : signal-to-noise ratio
SPP : surface plasmon polariton
 Δt : time step in FDTD calculations
 ΔT_{Ads} : change in temperature due to adsorption
 ΔT_{React} : change in temperature due to a chemical reaction
 $\Theta \vec{H}(\vec{r})$: Hermitian Operator in the PhC master equation
 t : time
 t_B : Bohr time 2.4×10^{-17} s
 t_{ARC} : thickness of a conventional Anti-Reflection-Coating (ARC)
 t_{ARL} : thickness of the Anti-Reflection-Layer (ARL) developed in this work
 T_{HF} : temperature of the electrolyte
 t_{int} : interaction time of radiation and gas
 t_l : time required for PECE macropores of depth l_{pore}
 t_t : thickness of the trenches in the PECE process
 t_{Wafer} : thickness of a (Si) wafer
 ΔU_e : change in electric potential

UPb, Univ. Pb : University of Paderborn

$u_{n,\vec{k}}(\vec{r})$: periodic part of the Bloch state

$\tilde{\nu}$: wavenumber (cm^{-1})

v : speed of the moveable mirror in a Michelson interferometer

V : external voltage applied during the photo-electrochemical etching of Si

V_{bi} : built-in potential for the HF/Si contact

V_{eff} : effective potential at the HF/Si interface

V_{PS} : voltage at which j_{PS} occurs

v_g : group velocity

VIS : visible spectral range

V_{OCP} : zero current potential

v_{100} : speed of macropore growth along [100]-direction in Si

WI : line defect consisting of 1 row of omitted pores in a hexagonal pore array (e.g., to realize a PhC waveguide)

x_{SCR} : width of the space charge region at the HF/Si interface

ΔZ_e : change of impedance

ZIB : Konrad-Zuse-Zentrum für Informationstechnik, Berlin, Germany; www.zib.de

Bibliography

- [1] W. Shockley. Circuit element utilizing semiconductive material. *U.S. Patent 2 569 347*, 1948.
- [2] S.M. Sze, editor. *Semiconductor Devices: Pioneering Papers*. World Scientific Pub. Co. Inc., 1990.
- [3] P. Ruterana, M. Albrecht, and J. Neugebauer, editors. *Nitride Semiconductors: Handbook on Materials and devices*. Wiley VCH, 2002.
- [4] E. Yablonovitch, T. J. Gmitter, and K. M. Leung. Photonic band structure: the face-centered cubic case employing nonspherical atoms. *Phys. Rev. Lett.*, 67:2295, 1991.
- [5] J. D. Joannopoulos, R. D. Meade, and J. N. Winn. Photonic crystals molding the flow of light. *Princeton University Press*, ISBN 0-691-03744-2, 1995.
- [6] S. John. Strong localization of photons in certain disordered dielectric superlattices. *Phys. Rev. Lett.*, 58:2486, 1987.
- [7] E. Yablonovitch. Inhibited spontaneous emission in solid-state physics and electronics. *Phys. Rev. Lett.*, 58:2059, 1987.
- [8] K.M. Ho, C.T. Chan, C.M. Soukoulis, R. Biswas, and M. Sigalas. Photonic bandgap in three dimensions: New layer-by-layer periodic structures. *Solid State Commun.*, 89:413, 1994.
- [9] O. Toader and S. John. Photonic band gaps based on tetragonal lattices of slanted pores. *Science*, 292:1133, 2001.
- [10] R. Hillebrand, S. Senz, W. Hergert, and U. Gösele. Macroporous-silicon-based three-dimensional photonic crystal with a large complete band gap. *J. Appl. Phys*, 94:2188, 2003.
- [11] P. Lodahl, A.F. van Driel, I.S. Nikolaev, A. Irman, K. Overgaag, D. Vanmaekelbergh, and W.L. Vos. Controlling the dynamics of spontaneous emission from quantum dots by photonic crystals. *Nature*, 430:654, 2004.
- [12] H. Kosaka, T. Kawashima, A. Tomita, M. Notomi, T. Tamamura, T. Sato, and S. Kawakami. Superprism phenomena in photonic crystals. *Phys. Rev. B*, 58:10096, 1998.

- [13] T. Asano, B.S. Song, Y. Tanaka, and S. Noda. Investigation of a channel-add drop-filtering device using acceptor-type point defects in a two-dimensional photonic-crystal slab. *Appl. Phys. Lett.*, 83:407, 2003.
- [14] M. Qiu and B. Jaskorzynska. Design of a channel drop filter in a two-dimensional triangular photonic crystal. *Appl. Phys. Lett.*, 83:1074, 2003.
- [15] Y. Akahane, T. Asano, B.S. Song, and S. Noda. Investigation of high-Q channel drop filters using donor-type defects in two-dimensional photonic crystal slabs. *Appl. Phys. Lett.*, 83:1512, 2003.
- [16] B.K. Min, J.-E. Kim, and H.Y. Park. High-efficiency surface-emitting channel drop filters in two-dimensional photonic crystal slabs. *Appl. Phys. Lett.*, 86:011106, 2005.
- [17] T. Baba. Observation of light propagation in photonic crystal optical waveguides with bends. *Electron. Lett.*, 35:654, 1999.
- [18] T. Baba and N. Fukaya. Light propagation characteristics of defect waveguides in a photonic crystal slab. *NATO Science Series C*, 563:105, 2001.
- [19] M. Notomi, K. Yamada, A. Shinya, J. Takahashi, C. Takahashi, and I. Yokohama. Extremely large group-velocity dispersion of line-defect waveguides in photonic crystal slabs. *Phys. Rev. Lett.*, 87:253902, 2001.
- [20] C. Sell, C. Christensen, J. Muehlmeier, G. Tuttle, Z.-Y. Li, and K.-M. Ho. Waveguide networks in three-dimensional layer-by-layer photonic crystals. *Appl. Phys. Lett.*, 84:4605, 2004.
- [21] M. Loncar, T. Yoshie, A. Scherer, P. Gogna, and Y. Qiu. Low-threshold photonic crystal laser. *Appl. Phys. Lett.*, 81(15):2680, 2002.
- [22] J.C. Knight, J. Broeng, T.A. Birks, and P.St.J. Russell. Photonic band gap guidance in optical fibers. *Science*, (282):1476–1478, 1998.
- [23] J.C. Knight, T.A. Birks, P.St.J. Russell, and D.M. Atkin. All-silica single-mode fiber with photonic crystal cladding. *Opt. Lett.*, 21:1547–1549, 1997.
- [24] W.H. Reeves, D.V. Skryabin, F. Biancalana, J.C. Knight, P.St.J. Russell, F.G. Omenetto, A. Efimov, and A.J. Taylor. Transformation and control of ultrashort pulses in dispersion-engineered photonic crystal fibres. *Nature*, 424:511, 2003.
- [25] H. Ouyang, L.A. Delouise, M. Christophersen, B.L. Miller, and P.M. Fauchet. Biosensing with one-dimensional photonic bandgap structure. *Proc. SPIE*, 5511:5511–08, 2004.
- [26] M. Loncar, A. Scherer, and Y. Qiu. Photonic crystal laser sources for chemical detection. *Appl. Phys. Lett.*, 82(26):4648, 2003.
- [27] C.J. Oton, L. Pancheri, Z. Gaburro, L. Pavesi, C. Baratto, G. Faglia, and G. Sberveglieri. Multiparametric porous silicon gas sensors with improved quality and sensitivity. *Phys. Stat. Sol. A*, 197(2):523, 2003.

- [28] C. Charlton, B. Temelkuran, G. Dellemann, and B. Mizaikoff. Midinfrared sensors meet nanotechnology: Trace gas sensing with quantum cascade lasers inside photonic band-gap hollow waveguides. *Appl. Phys. Lett.*, 86(19):194102, 2005.
- [29] A. Feist, A. Lambrecht, J. Schilling, F. Müller, and R.B. Wehrspohn. Vorrichtung und Verfahren zur qualitativen und quantitativen Bestimmung von Gasen und Flüssigkeiten mit PBG-Struktur. Patent DE 100 63 151 A1.
- [30] H. Altug and J. Vuckovic. Experimental demonstration of the slow group velocity of light in two-dimensional coupled photonic crystal microcavity arrays. *Appl. Phys. Lett.*, 86(11):111102, 2005.
- [31] G.v. Freymann, S. John, S. Wong, V. Kitaev, and G.A. Ozin. Measurement of group velocity dispersion for finite size three-dimensional photonic crystals in the near-infrared spectral region. *Appl. Phys. Lett.*, 86(5):053108, 2005.
- [32] Siemens. Günstige Gassensoren im Chipformat. *Physik Journal*, 3(10):16, 2004.
- [33] J. Staab. *Industrielle Gasanalyse*. R. Oldenbourg Verlag GmbH, München, 1994.
- [34] A. Modi, N. Koratkar, E. Lass, B. Wei, and P. M. Ajayan. Miniaturized gas ionization sensors using carbon nanotubes. *Nature*, 424:171, 2003.
- [35] Puscasu I., Pralle M.U., McNeal M.P., Moelders N., Last L., Ho W., Greenwald A.C., Daly J.T., Johnson E.A., El-Kady I., and Biswas R. Frequency selective surfaces enable MEMS gas sensor. *Mat. Res. Soc. Proc.*, 722:395–400, 2002.
- [36] M.U. Pralle, N. Moelders, M.P. McNeal, I. Puscasu, A.C. Greenwald, J.T. Daly, E. A. Johnson, T. George, D.S. Choi, I. El-Kady, and R. Biswas. Photonic crystal enhanced narrow-band infrared emitters. *Appl. Phys. Lett.*, 81:4685, 2004.
- [37] I. Puscasu, M. Pralle, M. McNeal, J. Daly, A. Greenwald, E. Johnson, R. Biswas, and C. G. Ding. Extraordinary emission from two-dimensional plasmonic-photonic crystals. *J. Appl. Phys.*, 98(1):013531, 2005.
- [38] Y.L. Hoo, W. Jin, C. Shi, H.L. Ho, and S.C. Ruan D.N. Wang. Design and modeling of a photonic crystal fiber gas sensor. *Appl. Opt.*, 42(18):3509, 2003.
- [39] S.D. Hart, G.R. Maskaly, B. Temelkuran, P.H. Pridaux, J.D. Joannopoulos, and Y. Fink. Wavelength-scalable hollow optical fibres with large photonic bandgaps for CO₂ laser transmission. *Science*, 296(5567):510, 2002.
- [40] K. Sakoda. *Optical Properties of Photonic Crystals*, volume 80 of *Optical Sciences*. Springer, 2001.
- [41] J.D. Jackson. *Classical Electrodynamics*. John Wiley & Sons, Inc., 1999.
- [42] Diverse. *Die Bibel nach der Übersetzung Martin Luthers*, chapter Gen 1, 3b. Deutsche Bibelgesellschaft Stuttgart, 1985.

- [43] S.G. Johnson and J.D. Joannopoulos. Block-iterative frequency-domain methods for maxwell's equations in a planewave basis. *Opt. Express*, 8:173, 2001.
- [44] K.S. Yee et al. Numerical solution of initial boundary value problems involving Maxwell's equations in isotropic media. *IEEE Trans. Antennas Propag.*, AP-14(3):302–307, 1966.
- [45] A. Taflove, editor. *Advances in Computational Electrodynamics: The Finite-Difference Time-Domain Method*. Artech House, 685 Canton Street, Norwood, MA 02062, USA, 1998.
- [46] V. Lehmann. The physics of macropore formation in low doped n-type silicon. *J. Electrochem. Soc.*, 140:2836, 1993.
- [47] V. Lehmann and H. Föll. Formation mechanism and properties of electrochemically etched trenches in n-type silicon. *J. Electrochem. Soc.*, 137:653, 1990.
- [48] P. Allongue. INSPEC data series, 1997.
- [49] V. Lehmann. *Electrochemistry of Silicon*. Wiley-VCH, 2002.
- [50] H. Föll, M. Christophersen, J. Carstensen, and G. Hasse. Formation and application of porous silicon. *Mat. Sci. Eng.*, R39:93, 2002.
- [51] J. Carstensen, M. Christophersen, G. Hasse, and H. Föll. Parameter dependence of pore formation in silicon within a model of local current bursts. *phys. stat. sol. (a)*, 182:63, 2000.
- [52] H. Miyazaki, M. Hase, H.T. Miyazaki, Y. Kurokawa, and N. Shinya. Photonic material for designing arbitrarily shaped mirrors and microcavities in two dimensions. *J. Appl. Phys.*, 95:4555, 2004.
- [53] M. Notomi, H. Suzuki, T. Tamamura, and K. Edagawa. Lasing action due to the two-dimensional quasiperiodicity of photonic quasicrystals with a penrose lattice. *Phys. Rev. Lett.*, 92:123906, 2004.
- [54] A. Della Villa, S. Enoch, G. Tayeb, V. Pierro, V. Galdi, and F. Capolino. Band gap formation and multiple scattering in photonic quasicrystals with a penrose-type lattice. *Phys. Rev. Lett.*, 94(18):183903, 2005.
- [55] F. Genereux, S.W. Leonard, H.M. van Driel, A. Birner, and U. Gösele. Large birefringence in two-dimensional silicon photonic crystals. *Phys. Rev. B*, 63(16):161101, 2001.
- [56] J. Faist, F. Capasso, D.L. Sivco, C. Sirtori, A.L. Hutchinson, and A.Y. Cho. Quantum cascade laser. *Science*, 264(5158):553–556, 1994.
- [57] X. Letartre, C. Seassal, C. Grillet, P. Rojo-Romeo, P. Viktorovitch, M. Le Vassoe d'Yerville, D. Cassagne, and C. Jouanin. Group velocity and propagation losses measurement in a single-line photonic-crystal waveguide on InP membranes. *Appl. Phys. Lett.*, 79(15), 2001.
- [58] F. Raineri, G. Vecchi, A.M. Yacomotti, C. Seassal, P. Viktorovitch, R. Raj, and A. Levenson. Doubly resonant photonic crystal for efficient laser operation: Pumping and lasing at low group velocity photonic modes. *Appl. Phys. Lett.*, 86:011116, 2005.

- [59] E. Moreno, F.J. Garcia-Vidal, and L. Martin-Moreno. Enhanced transmission and beaming of light via photonic crystal surface modes. *Phys. Rev. B*, 69(12):121402, 2004.
- [60] E. Moreno, L. Martin-Moreno, and F.J. Garcia-Vidal. Efficient coupling of light into and out of a photonic crystal waveguide via surface modes. *Photonics and Nanostructures*, 2:97, 2004.
- [61] T. D. Happ, M. Kramp, and A. Forchel. Photonic crystal tapers for ultracompact mode conversion. *Opt. Lett.*, 26:1102, 2001.
- [62] D.W. Prather, J. Murakowski, S. Shi, S. Venkataraman, A. Saharkawy, C. Chen, and D. Pustai. High-efficiency coupling structure for a single-line-defect photonic-crystal waveguide. *Opt. Lett.*, 27:1601, 2002.
- [63] S.G. Johnson, P. Bienstman, M.A. Skorobogatiy, M. Ibanescu, E. Lidorikis, and J.D. Joannopoulos. Adiabatic theorem and continuous coupled-mode theory for efficient taper transitions in photonic crystals. *Phys. Rev. E*, 66:066608, 2003.
- [64] J. Witzens, M. Hochberg, T. Baehr-Jones, and A. Scherer. Mode matching interface for efficient coupling of light into planar photonic crystals. *Phys. Rev. E*, 69:046609, 2004.
- [65] S.G. Johnson, S. Fanand, P.R. Villeneuve, J.D. Joannopoulos, and L.A. Kolodziejski. Guided modes in photonic crystal slabs. *Phys. Rev. B*, 60:5751, 1999.
- [66] J. Schilling. *Herstellung und optische Eigenschaften von 2D- und 3D-photonicen Kristallen aus makroporösem Silizium*. PhD thesis, Martin-Luther-Universität Halle-Wittenberg, 2002.
- [67] S. Richter, R. Hillebrand, C. Jamois, M. Zacharias, U. Gösele, S.L. Schweizer, and R.B. Wehrspohn. Periodically arranged point defects in two-dimensional photonic crystals. *Phys. Rev. B*, 70(19):193302, 2004.
- [68] H. J. Lezec, A. Degiron, E. Devaux, R. A. Linke, L. Martin-Moreno, F. J. Garcia-Vidal, and T. W. Ebbesen. Beaming light from a subwavelength aperture. *Science*, 297:820, 2002.
- [69] M. Qiu and S. He. Surface modes in two-dimensional dielectric and metallic photonic bandgap structures. *Phys. Lett. A*, 282:85–91, 2005.
- [70] F. Ramos-Mendieta and P. Halevi. Electromagnetic surface modes of a dielectric superlattice: the supercell method. *J. Opt. Soc. Am. B*, 14(2):370–381, 1997.
- [71] F. Ramos-Mendieta and P. Halevi. Surface electromagnetic waves in two-dimensional photonic crystals: Effect of the position of the surface plane. *Phys. Rev. B*, 59(23):15112–15120, 1999.
- [72] W.M. Robertson, G. Arjavalingam, R.D. Meade, K.D. Brommer, A.M. Rappe, and J.D. Joannopoulos. Observation of surface photons on periodic dielectric arrays. *Opt. Lett.*, 18(7):528–530, 1993.
- [73] R.D. Meade, K.D. Brommer, A.M. Rappe, and J.D. Joannopoulos. Electromagnetic Bloch waves at the surface of a photonic crystal. *Phys. Rev. B*, 44(19):10961, 1991.

- [74] M. Christophersen, J. Carstensen, A. Feuerhake, and H. Föll. Pore Formation Mechanisms for the Si-HF System. *Mater. Sci. Eng. B.*, 69:194, 2000.
- [75] S.Y. Lin, J.G. Fleming, D.L. Hetherington, B.K. Smith, R. Biswas, K.M. Ho, M.M. Sigalas, W. Zubrzycki, S.R. Kurtz, and J. Bur. A three-dimensional photonic crystal operating at infrared wavelengths. *Nature*, 394:251, 1998.
- [76] A. Blanco, E. Chomski, S. Grabtchak, M. Ibisate, S. John, S. W. Leonard, C. Lopez, F. Meseguer, H. Miguez, J. P. Mondia, G. A. Ozin, O. Toader, and H. M. van Driel. Large-scale synthesis of a silicon photonic crystal with a complete three-dimensional bandgap near 1.5 micrometres. *Nature*, 405:437, 2000.
- [77] M. Loncar, D. Nedeljkovic, T. Doll, J. Vuckovic, A. Scherer, and T.P. Pearsall. Waveguiding in planar photonic crystals. *Appl. Phys. Lett.*, 77:1937, 2000.
- [78] S. Ottow, V. Lehmann, and H. Föll. Processing of three dimensional microstructures using macroporous n-type silicon. *J. Electrochem. Soc.*, 143:385, 1996.
- [79] S.L. Schweizer, R.B. Wehrspohn, and J. Schilling. Improved electrochemical etching of macroporous silicon - the role of surfactants. volume 203rd meeting of *ECS spring meeting*, Palais des Congres de Paris, April 2003. The Electrochemical Society.
- [80] U. Grüning. *Realisierung photonischer Bandstrukturen in makroporösem Silizium*. PhD thesis, Friedrich-Alexander-Universität Erlangen-Nürnberg, 1996.
- [81] G. Barillaro, A. Nannini, and F. Pieri. Dimensional Constraints on High Aspect Ratio Silicon Microstructures Fabricated by HF Photoelectrochemical Etching. *J. Electrochem. Soc.*, 149:C180–C185, 2002.
- [82] G. Barillaro, A. Nannini, and M. Piottob. Electrochemical etching in HF solution for silicon micromachining. *Sens. Act. A*, 102:195, 2002.
- [83] M. Christophersen, P. Merz, J. Quenzer, J. Carstensen, and H. Föll. Deep electrochemical trench etching with organic hydrofluoric electrolytes. *Sens. Act. A*, 88(3):241–246, 2001.
- [84] P. Kramper, M. Agio, C. M. Soukoulis, A. Birner, F. Müller, R. B. Wehrspohn, U. Gösele, and V. Sandoghdar. Highly directional emission from photonic crystal waveguides of sub-wavelength width. *Phys. Rev. Lett.*, 92:113903, 2004.
- [85] M. Steinhart, J. H. Wendorff, A. Greiner, R. B. Wehrspohn, K. Nielsch, J. Schilling, J. Choi, and U. Gösele. Polymer nanotubes by wetting of ordered porous templates. *Science*, 296:1997, 2002.